



What's new and what's next in diffusion MRI preprocessing

Chantal M.W. Tax^{a,b,1,*}, Matteo Bastiani^{c,d,1}, Jelle Veraart^{e,1}, Eleftherios Garyfallidis^{f,1},
M. Okan Irfanoglu^{g,1}

^a Image Sciences Institute, University Medical Center Utrecht, The Netherlands

^b Cardiff University Brain Research Imaging Centre, School of Physics and Astronomy, Cardiff University, UK

^c Sir Peter Mansfield Imaging Centre, School of Medicine, University of Nottingham, UK

^d Wellcome Centre for Integrative Neuroimaging (WIN), Centre for Functional Magnetic Resonance Imaging of the Brain (FMRIB), University of Oxford, UK

^e Center for Biomedical Imaging, New York University Grossman School of Medicine, NY, USA

^f Department of Intelligent Systems Engineering, Indiana University, Bloomington, USA

^g Quantitative Medical Imaging Section, National Institute of Biomedical Imaging and Bioengineering, National Institutes of Health, Bethesda, MD, USA

ARTICLE INFO

Keywords:

Diffusion MRI
Artifacts
Distortion
Preprocessing

ABSTRACT

Diffusion MRI (dMRI) provides invaluable information for the study of tissue microstructure and brain connectivity, but suffers from a range of imaging artifacts that greatly challenge the analysis of results and their interpretability if not appropriately accounted for. This review will cover dMRI artifacts and preprocessing steps, some of which have not typically been considered in existing pipelines or reviews, or have only gained attention in recent years: brain/skull extraction, B-matrix incompatibilities w.r.t the imaging data, signal drift, Gibbs ringing, noise distribution bias, denoising, between- and within-volumes motion, eddy currents, outliers, susceptibility distortions, EPI Nyquist ghosts, gradient deviations, B_1 bias fields, and spatial normalization. The focus will be on “what’s new” since the notable advances prior to and brought by the Human Connectome Project (HCP), as presented in the predeceasing issue on “Mapping the Connectome” in 2013. In addition to the development of novel strategies for dMRI preprocessing, exciting progress has been made in the availability of open source tools and reproducible pipelines, databases and simulation tools for the evaluation of preprocessing steps, and automated quality control frameworks, amongst others. Finally, this review will consider practical considerations and our view on “what’s next” in dMRI preprocessing.

1. Introduction

Diffusion MRI (dMRI) sensitizes the NMR signal to the translational diffusive motion of water molecules which is in turn modulated by the presence of tissue barriers. As such, dMRI has been widely used in clinical and biomedical research applications to infer valuable information about the underlying tissue microstructure, far below the actual imaging resolution. The work horse in most dMRI applications to date is the spin-echo (SE) experiment combined with an echo-planar imaging (EPI) readout, with diffusion-encoding magnetic field gradients applied between the 90° and 180° pulses, and between the 180° pulse and image readout. EPI has the advantage of having excellent signal-to-noise-per-unit-time, which allows rapid acquisition of multiple dMRI images with varying diffusion encoding, i.e., gradient strength and timing along each axis. Combining images with multiple gradient encoding settings, in turn, provides the opportunity to derive quantitative measures related to the 3D diffusion process and/or tissue microstructure. However, a well-know challenge with EPI is its susceptibility to B_0 field inhomogeneities

and the switching of strong diffusion-weighted gradients induce eddy currents. In addition, quantitative diffusion MRI analyses, including biophysical modeling and tractography, benefit from high contrast-to-noise ratio (CNR) through substantial diffusion weighting, which comes at the expense of low signal-to-noise ratio (SNR). Therefore, dMRI data is characterized with various imaging artifacts, particularly the inherent subject motion and physiological noise, that challenge data processing and analysis (Jones and Cercignani, 2010; Le Bihan et al., 2006a; Pierpaoli, 2010; Tax et al., 2016). Hence, performing a range of preprocessing steps is generally recommended to reduce the confounding effects inherent in dMRI acquisitions. In this review, “preprocessing” refers to any frequency- or image-domain operation that is performed on the data (including filtering, spatial registration, and other cleaning steps (Esteban et al., 2018)) after acquisition and prior to final dMRI model estimation.

The Human Connectome Project (HCP), initiated nearly a decade ago in pursuit of improving our understanding of the human “connectome”, has brought significant advancements in hardware,

* Corresponding author.

E-mail address: taxc@cardiff.ac.uk (C.M.W. Tax).

¹ PhD



Fig. 1. Overview of dMRI artifacts and processing strategies discussed in this paper.

acquisition, and preprocessing. These developments have been extensively described in the Special Issue “Mapping the Connectome”, predecessor of the current Special Issue. Developments in image acquisition included stronger gradients for diffusion weighting, simultaneous multislice (SMS)/multiband (MB) for accelerated acquisition, higher resolution imaging, 2-way reversed phase encoding acquisition for improved correction of susceptibility-induced image distortions, and wide availability of multi-shell dMRI data (Sotiropoulos et al., 2013c). Developments in dMRI preprocessing included a predictive model for eddy current-induced image distortions, integrated motion-, eddy current-, and susceptibility-induced distortion correction leveraging reversed phase encoding acquisitions, and simultaneous detection and replacement of movement-induced signal dropouts. This effort has clearly demonstrated the need for an integrated approach to acquisition and preprocessing where one is informed by results and performance of the other: the choice for monopolar instead of bipolar diffusion encoding has for instance encouraged the development of approaches to ameliorate the amplified eddy current distortions associated with the former, and the increased availability of reversed phase encoding acquisitions in the community called for methods able to leverage this additional information.

In the context of the current special issue “Advances in Mapping the Connectome”, the aim of this paper is to provide an overview of dMRI artifacts and preprocessing steps prior to dMRI estimation and brain connectivity mapping, summarizing some notable advances prior to the HCP and brought by the HCP, while focusing on what’s new in the post-HCP era. Observed trends in the recent literature include the development of tools to promote the availability of reproducible pipelines (e.g. through containers), the emergence of databases and simulations

specifically targeted at evaluating preprocessing steps, and efforts that perform automated quality control (QC) and quantitatively and qualitatively compare preprocessing steps. Finally, we will provide our view on practical considerations and what’s next in dMRI preprocessing.

2. Artifacts and what’s new in dMRI preprocessing

We will go over an extensive list of dMRI artifacts, focusing on the preprocessing steps needed to address them (Fig. 1). In each section, we will provide the reader with an introduction to the artifact and a summary of pre-HCP techniques, as well as a description of more recent post-HCP preprocessing strategies and tools, and some practical considerations including quality control and generalizability. As part of this review, we have collected and classified a list of references related to dMRI preprocessing, which will be made public for the community to contribute to. As such, we endeavour to facilitate the navigation through the breadth of tools and software packages available, as well as keeping an up-to-date overview of dMRI preprocessing developments (temporary link: <https://github.com/dmripreprocessing/neuroimage-review-2022>). The reader should note that the order of the preprocessing steps listed below does not necessarily reflect an optimal or suggested pipeline and different preprocessing packages indeed apply several of these steps at different stages during their execution. Where appropriate, we discuss some practical considerations regarding the ordering of steps. In addition, where steps are interlinked, we refer to the relevant section.

2.1. Brain/skull extraction

Description and Importance:

Diffusion MR images of the head contain not only the brain (here assumed to be the organ of interest), but also other structures such as the skin, skull, eyes, meninges, cranial nerves and face muscles. Brain extraction algorithms allow the removal of these structures from the data to potentially improve the reliability of further preprocessing steps, such as tissue segmentation or cross-modal registration, in addition to reducing the computational demands of any subsequent analyses as these can be constrained to the voxels of interest. For example, using an imperfect mask can lead to the inclusion of voxels with spuriously high fractional anisotropy (FA) at the periphery of the brain, which might bias further registration or analysis steps.

Approaches prior to and brought by the HCP:

Brain extraction in dMRI can take advantage of the skull, fat and muscle tissue having considerably lower signal intensity than the brain in fat-suppressed EPI acquisitions. Therefore, the problem can be formulated as a standard image processing background/foreground segmentation. The well-known Otsu histogram thresholding technique (Otsu, 1979) can be retrofitted to this problem to find the optimal signal threshold that separates the brain from non-brain regions and is the brain extraction algorithm of choice in multiple preprocessing pipelines (Garyfallidis et al., 2014).

Another popular technique, FSL's Brain Extraction Tool (BET) (Smith, 2002), is widely used across different imaging modalities, including dMRI. BET makes mild assumptions about the shape of the brain and it radially projects beams from an initial center position onto a small centered spherical mesh, until the beams reach large intensity gradients. The slowly growing mesh is updated iteratively to accommodate the shape of the brain. A similar approach, AFNI's 3dSkullStrip (Cox, 1996) first removes gross spatial image nonuniformities and repositions the brain to a more convenient orientation and subsequently applies a modified version of BET for brain extraction. For dMRI datasets, these methods are most typically performed on the first non-diffusion-weighted $b = 0$ s/mm² image (referred as the $b = 0$ image throughout this manuscript).

Another category of brain extraction techniques nonlinearly register the $b = 0$ image to one or multiple brain templates (or vice versa) for which segmentation or tissue probability maps have been pre-generated. These template-based brain extraction methods subsequently perform a voting procedure that decides whether a voxel belongs to the foreground or background. BEaST (Eskildsen et al., 2012) and ALFA (Serag et al., 2016) are examples that use multiple templates to statistically improve the voting process.

Diffusion MRI-specific methods leverage the properties of the dMRI signal by fitting a diffusion model to the data and using the derived measures for brain extraction. One of the first measures adopted in this context is Quantitative Anisotropy proposed for Generalized Q-Sampling Imaging (GQI) (Yeh et al., 2010) but can be generalized to any model computing orientation distribution functions (ODF) (e.g. DSI (Wedeen et al., 2005)). The properties of quantitative anisotropy in the brain and the background regions are sufficiently different that a single threshold is often adequate to remove the nonbrain areas.

Novel strategies:

Different types of deep learning architectures such as convolution neural networks (CNNs) (Kleesiek et al., 2016) or U-Nets (Wang et al., 2020b) have recently been proposed for brain extraction. In addition to deep learning-based segmentation, traditional machine learning classifiers such as random forests have been used to segment dMRI data into intracranial, brain, and cerebrospinal fluid (CSF) masks (Reid et al., 2018).

Practical considerations:

Brain extraction quite commonly requires user intervention in the form of $b = 0$ image selection, quality checking, and/or parameter optimization. Brain extraction is typically performed on the first $b = 0$ image, however, any artifacts deteriorating its quality will also impact its performance. Since such a reference image is often used for multiple preprocessing steps (e.g. motion correction, see Section 2.8) it is good

practice to select images with minimal artifacts for brain extraction either manually or automatically (Bastiani et al., 2019b). However, even with adequate data the extraction algorithm can generate unsatisfactory results (e.g. in the case of low signal intensities), and therefore the quality of the extracted brain masks should be checked. Several brain extraction algorithms are designed for in vivo human brain data and are not directly applicable to other organs or species and/or require extensive parameter tuning.

The Otsu technique assumes a bimodal signal distribution and can be sensitive to noise in the data. It is therefore commonly performed after the application of a median filter which removes spurious intensities (Garyfallidis et al., 2014) to increase its accuracy. As it does not rely on a priori brain shape information, it can more readily be applied to brains of other species. In contrast, FSL's BET and AFNI's 3dSkullStrip (in its default setting), have a priori assumptions on the brain shape and can not directly be applied to other organs or species. Additionally, the performance of BET relies on the accuracy of the center estimation and the validity of its uniform intensity assumption.

The registration quality of the brain outline in template-based extraction methods is of fundamental importance for its accuracy. The machine learning methods depend quite strongly on the size and the representation power of the training dataset. Accurate segmentation is further challenged by pathology in clinical datasets, for example in traumatic brain injury (TBI) patients (see Lutkenhoff et al. (2014)).

Brain extraction is generally performed early in the pipeline as other steps can require a mask (e.g. signal drift correction (Section 2.3) and motion/eddy current correction (Sections 2.7 and 2.9)). However, computation of a brain mask prior to susceptibility distortion correction (Section 2.11) can lead to inaccurate results, as signal pile-up and signal-reduction can confuse brain extraction approaches. In addition, the mask will suffer from the same geometric distortions as the uncorrected $b = 0$ image, which for example complicates registration to anatomical T1 weighted images. Furthermore, brain extraction prior to motion correction and eddy current distortion correction may lead to suboptimal masking of diffusion-weighted images (DWIs) as they are affected by translations/rotations and geometrical distortions compared to the first $b = 0$ image. Therefore, brain extraction can be performed at multiple stages in the pipeline, and it is good practice to compute an updated mask after preprocessing and prior to further analysis steps such as model fitting, spatial normalization, and registration to anatomical images.

2.2. B-Matrix incompatibility with the imaging data

Description and Importance: The B-matrix (Mattiello et al., 1997) or B-tensor contains information on the diffusion encoding - i.e., the diffusion gradient orientation and strength - associated to a dMRI volume, which is necessary for the estimation of diffusion models and representations. Depending on the scanner manufacturer, model, and software version, the diffusion encoding information may be stored in the DICOM headers in the form of either a b -value/ b -vector pair (which can be used to compute the B-matrix of Stejskal-Tanner acquisitions, Fig. 2), or the B-matrix itself (which can be decomposed into b -values/ b -vectors through singular value decomposition and can also accommodate more general encodings, see Section 5.3). The b -values contain information about the magnitude and timing of the diffusion gradients and the b -vectors about their orientation. Depending on the scanner, the B-matrix can also include the information of the effects of imaging gradients on diffusion sensitization (Lundell et al., 2014; Mattiello et al., 1997).

Different scanner manufacturers and software versions can save the B-matrix in different ways, e.g. flips in directions (Fig. 2a) or permutation in axes (Fig. 2b)). This can result in a mismatch between the coordinate systems of the B-matrix and imaging data. Furthermore, permutations and flips can occur during conversion between file formats or between different software packages.

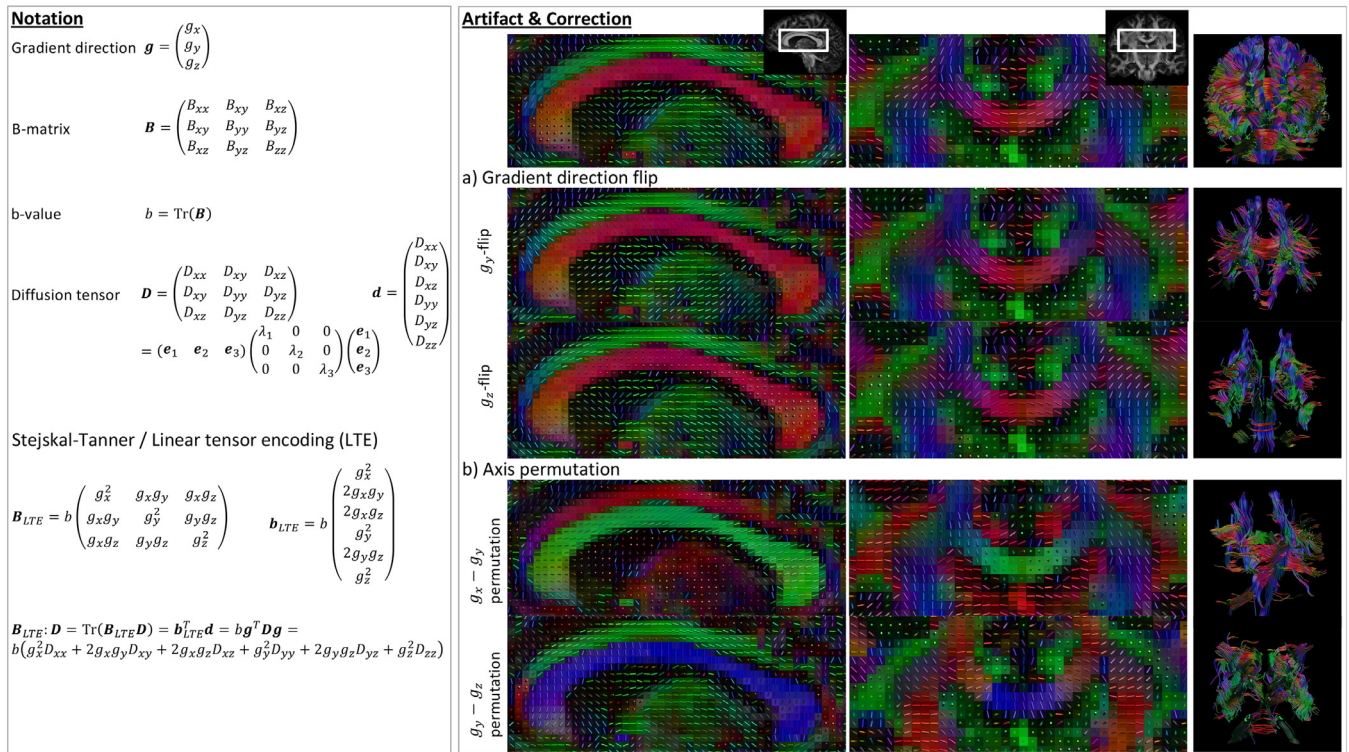


Fig. 2. B-matrix incompatibilities. Left: example notations used for the gradient direction, B-matrix, b-value, and diffusion tensor, where capital letters denote tensors and lower case letters their vectorized form. $\text{Tr}()$ denotes the trace. The computation of the B-matrix from the gradient directions (stored in the .bvec file) and b-values (stored in the .bval file) in the case of conventional Stejskal-Tanner or linear tensor encoding (LTE) is shown. **a)** The first eigenvector of the DT (sagittal and coronal view) and resulting tractography (coronal anterior view) is shown for y- and z-gradient direction sign flips; here the x-, y-, and z-axes correspond to left-right, anterior-posterior, and inferior-superior axes, respectively. Note that these flips cannot be identified on the FA or color-FA maps (where the RGB color reflects the direction of the DT first eigenvector). **b)** Gradient axes permutations, these become apparent on the color-FA maps.

B-matrix incompatibilities with the imaging data are particularly problematic for rotational variance analyses such as fiber tractography. This issue might go unnoticed in dMRI studies, e.g. when solely analyzing dMRI-derived rotationally invariant scalar maps such as FA.

Approaches prior to and brought by the HCP: Manually inspecting the diffusion tensor (DT) first eigenvectors can reveal axes permutations and gradient flips (Fig. 2 right), but it is not always straightforward to find the appropriate correction and trial-and-error of the finite set of possibilities may be necessary. Automated solutions have been proposed that check for unintended B-matrix incompatibilities and correct the B-matrix to match the coordinate space of the imaging data. [Jeurissen et al. \(2014\)](#) introduced the average trajectory length as a measure of how well the gradient orientations match the diffusion MRI images. This strategy relies on the assumption that wrongly permuting axes or flipping gradient orientations will reduce the length of most anatomically correct trajectories and therefore reduce the average length, although it may result in a few slightly longer spurious streamlines. A similar approach is used by AFNI ([Cox, 1996](#)) using the GradFlipTest command ([Taylor et al., 2018](#)), and other tools provide similar utilities including functions for performing fast tracking and calculating the length of tracks.

Novel strategies: Recently a new approach was proposed by [Schilling et al. \(2019b\)](#) based on a "fiber coherence index", which quantifies the number of pairs of neighboring fiber orientations that are coherent, weighted by their anisotropy values. The coherence index is based on the assumption that white matter orientation is coherent on the millimeter scale throughout the brain, and that the correct gradient table results in the highest overall coherence. This approach showed good performance both in healthy subjects and in patients, and in *in vivo* and *ex vivo* animal data.

Practical considerations: The proposed methods are generally fast with few parameters, making them suitable for use across species and in *in vivo* and *ex vivo* data. Some B-matrix inconsistencies are difficult to recognize, for example a flip in the left-right direction on a coronal plane or when permutations and flips occur along multiple axes. In these cases, further manual QC may be required, i.e. looking for specific known pathways such as the Corpus Callosum (CC), cortico-spinal tract (CST) and arcuate fasciculus (AF). Finally, other artifacts may hamper the automatic detection of B-matrix inconsistencies, e.g. severe motion or signal dropouts ([Schilling et al., 2019b](#)). B-matrix checks are typically performed early in the pipeline, as quality checks (e.g. based on color-coded FA images) and steps relying on rotationally variant information are affected by incompatibilities.

2.3. Signal drift correction

Description and Importance: Several studies have observed a gradual change in signal intensity over time within a single dMRI data acquisition session (Fig. 3a) ([Froeling et al., 2017](#); [Hansen et al., 2019](#); [Vos et al., 2017](#)). In functional MRI, such low-frequency signal drift has been recognized as a confounding factor for decades and hypothesized to originate from factors such as scanner instabilities ([Smith et al., 1999](#)) and subject motion ([Bandettini et al., 1993](#)), but its effect has only relatively recently been reported in dMRI. dMRI signal drift can vary considerably across vendors, scanners, and sessions in magnitude (signal changes up to 17% across a session have been reported ([Vos et al., 2017](#))), temporal (decrease/increase, linear/higher order) and spatial pattern ([Hansen et al., 2019](#)). Several origins have been hypothesized, e.g. heating due to the rapid switching of gradients for EPI and diffusion

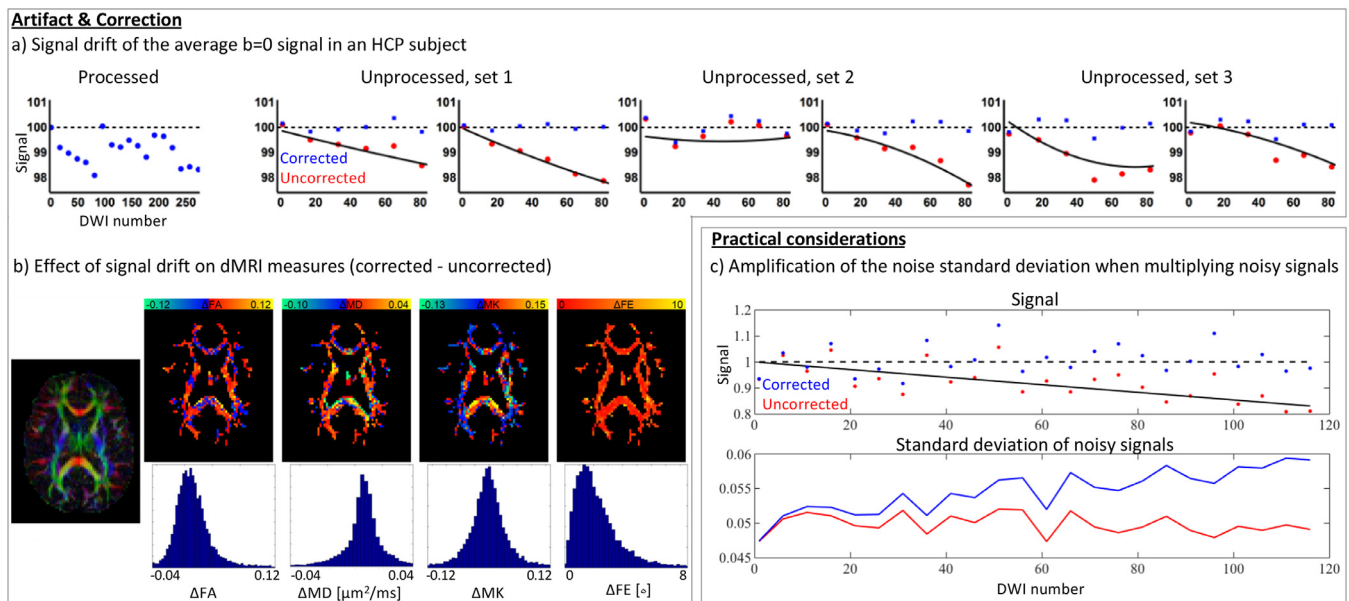


Fig. 3. Signal drift. **a)** The first column is the processed and combined dMRI dataset using the HCP processing pipeline, which excludes signal drift correction. The second to the seventh column contains the unprocessed HCP data, to which signal drift correction is applied: The red dots indicate the drift-affected signal, the black line a quadratic fit, and the blue dots the drift-corrected signal intensities. The second and third columns are the two sets of identical gradient directions but with opposite phase encoding direction. The fourth and fifth, and the sixth and seventh columns represent the second and third sets of gradient directions, respectively, each with opposite phase encoding direction. **b)** Effect of signal drift on dMRI measures FA, MD, MK, and diffusion tensor first eigenvector; Figures adapted from Vos et al. (2017). **c)** Simulated signal drift of 17% across the session (top). The noisy signals are corrected by multiplication of the estimated drift factor (blue dots), but when computing the standard deviation across a large number of noisy signals (bottom), one can see that it is affected by the drift factor.

encoding, drift in the main magnetic field (B_0), or an altered transmission energy and flip angle over time (Vos et al., 2017).

Not accounting for signal drift can cause significant non-trivial effects on diffusion measures (Fig. 3b) and fiber tractography, e.g. when the DWIs are acquired in an ordered fashion: if ordered from low to high b -value, a systematic artificial signal decrease in the later images can be interpreted as overestimated magnitude of diffusivity, and if ordered according to gradient direction proximity, a systematic bias can occur along specific orientations. Signal drift can also introduce a non-trivial bias even in acquisitions in which the diffusion directions and weightings are ordered randomly, albeit to a smaller extent (Vos et al., 2017).

Approaches prior to and brought by the HCP: During acquisition, several vendors provide the possibility to specifically correct for the B_0 drift (Benner et al., 2006). However, this approach may only partially correct (or even over-correct) the total signal drift and might not be an option on all clinical scanners. Offline processing strategies may capture such combined effects, but have not been reported prior to or in HCP pipelines.

Novel strategies: Vos et al. (2017) propose to acquire several interleaved $b = 0$ images, e.g. every 10th image. Hansen et al. (2019) propose to acquire a $b = 0$ image at least every 32 volumes, with a minimum of four volumes. From the $b = 0$ images, an average global signal drift model is then estimated over time based on a linear or quadratic relationship, and the image intensity of all images is adjusted accordingly. Froeling et al. (2017) estimate and correct the global signal drift using a quadratic relationship before correcting for subject motion and geometric image distortions.

Hansen et al. (2019) have recently extended this approach to accommodate for spatially-dependent signal drifts. Their spatiotemporal correction proposes a second order Chebyshev polynomial decomposition of the spatial effects, interacting with a linear or quadratic behavior of the temporal effects. On phantoms it is shown that the drift can indeed be spatially varying and that the spatiotemporal correction can outper-

form temporal correction, with significantly reduced errors in the estimated Apparent Diffusion Coefficients (ADC). This remains to be further evaluated in more complex scenarios such as the human brain.

Practical considerations: While signal drift correction has mostly been evaluated in phantoms and in vivo human brain, application in other species and *ex vivo* should be straightforward as long as appropriate tissue masks can be extracted and interleaved $b = 0$ images are available. The latter may be challenging to achieve on some clinical scanners where the flexibility to adapt the diffusion weightings/directions and their order is limited; interleaving $b = 0$ images commonly requires the possibility to read in a customized B-matrix file by the scanner software. If the global signal change is estimated within brain masks, ideally a separate brain mask should be computed per $b = 0$ image to account for subject motion.

Apparent changes in $b = 0$ image intensities may also occur due to other factors than signal drift, e.g. interactions of subject motion with susceptibility fields and gradient nonlinearities. In addition, outliers, respiratory or pulsatile motion, and inaccuracies in computed brain masks can affect the correction. A plot of the estimated drift over time could reveal such issues, and constraining the temporal characterization to lower orders should reduce the influence of higher-frequency variations. Inspection of brain mask overlays (Section 2.1) and outlier profiles (Section 2.10) could further reveal issues in the estimation. Robust procedures to estimate the (spatio)temporal drift factors are less affected by outliers (Hansen et al., 2019); e.g. in global temporal drift correction, the median $b = 0$ -signal should be more robust to subtle signal variations than the mean. Finally, current procedures correct for drift by multiplying the signal with an estimated drift factor. However, the multiplication of signals also implies multiplication of the noise (Fig. 3c).

Regarding the ordering of steps, temporal signal drift correction has been performed early in the pipeline (Froeling et al., 2017; Vos et al., 2017), but in the case of significant between-volumes subject motion (Section 2.7) the brain mask should be recomputed for each $b = 0$ vol-

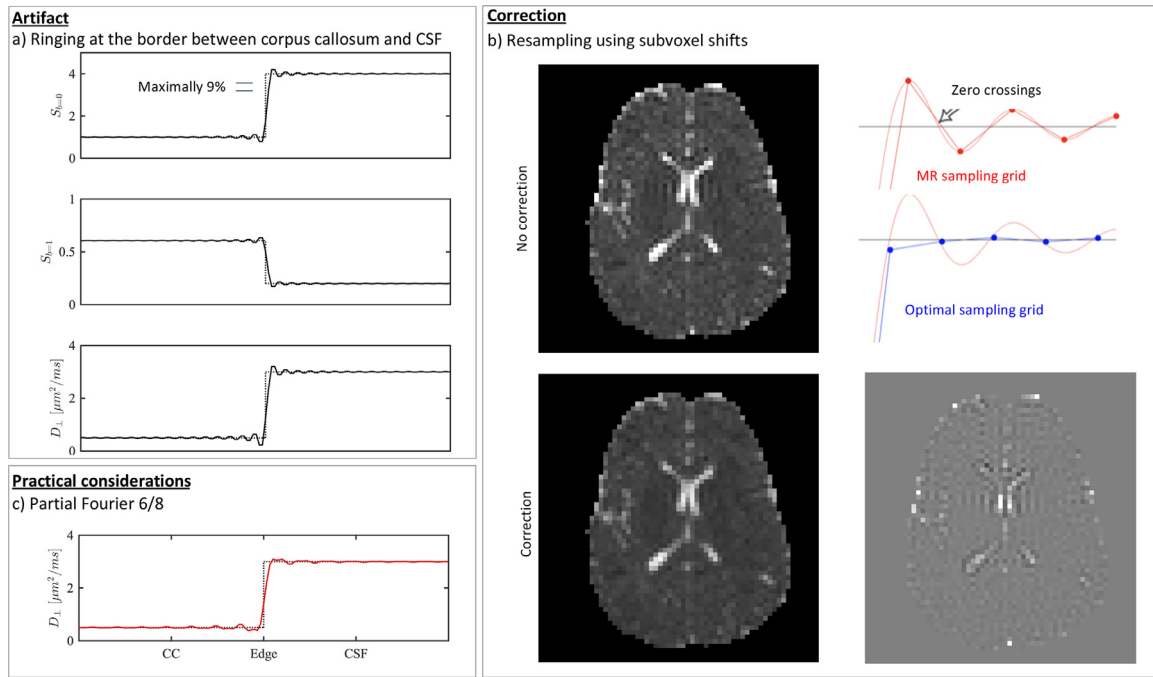


Fig. 4. Gibbs Ringing: **a)** The over- and undershoots of the radial diffusivity depend on the location x and greatly exceed the 9% variation observed in the simulated DW signals, which represent realistic parameter values on the border between CSF and Corpus Callosum (CC). **b)** The spurious ringing is apparent in parametric maps, such as mean diffusivity (top-left). By locally resampling the image using subvoxel shifts, one can achieve a signal sample of the zero-crossings instead of the peaks of the sinc function (top-right), enabling a suppression of the Gibbs ringing artifact (bottom-left). A residual map demonstrates how strongly the Gibbs ringing effect depends on the anatomy. **c)** Partial Fourier reconstruction might interfere with the classical Gibbs ringing pattern if data is zero-filled prior to reconstruction.

ume. Performing signal drift estimation after corrections for motion, susceptibility fields, and gradient nonlinearities may reduce their effect on mean $b = 0$ intensity fluctuations unrelated to signal drift. For spatiotemporal correction (Hansen et al., 2019) drift correction is typically performed after subject motion- and geometric distortion correction as spatial misalignment can influence the estimation.

2.4. Gibbs ringing correction

Description and Importance: Gibbs-ringing is a well-known artifact, which manifests itself as spurious signal oscillations or “ringing” near anatomical boundaries (Gibbs, 1898). The artifact is most notable around sharp boundaries in tissue signal intensity, such as tissue interfaces around the ventricles. Gibbs ringing is an intrinsic feature of all MR images that are reconstructed via an inverse Fourier transformation. With MRI, we are bound to acquire the Fourier expansion coefficients of an image, the k -space, instead of the image itself. Because of scan time and SNR limitations, the outer parts of k -space that contain the high frequency information of the image, are often recorded only up to a certain extent. The apparent sharp cut-off or truncation in the k -space is mathematically equivalent to a convolution of the image with a sinc function and will, as such, result in an imperfect approximation of sharp edges. Within a single MR image, the maximal spurious signal fluctuation is about 9% of the intensity step (Gibbs, 1898; Wilbraham, 1848). Because the magnitude, and even the sign, of this signal artifact is dependent on the underlying signal contrast, it is intrinsically dependent on the anatomical location, b -value, and the gradient direction. The estimation of diffusion parameters from dMRI data with varying b -value and/or gradient directions might amplify this artifact significantly (Barker et al., 2001; Kellner et al., 2016; Perrone et al., 2015; Veraart et al., 2016a). Indeed, the Gibbs effect is often much more noticeable in parametric maps, such as the FA or the mean kurtosis (MK), than the dMRI images themselves. For example, the appearance of non-positive definite diffusion tensors in tissue surrounding

the CSF has been observed and tied to Gibbs ringing by Barker et al. (2001).

Approaches prior to and brought by the HCP: A very efficient way to suppress Gibbs ringing is windowing the k -space with an apodizing filter. By gradually attenuating the highest acquired frequencies, a sharp cut-off can be avoided in k -space. Typical filters are the Gaussian, Hanning, and Hamming filters. Unfortunately, such filtering introduces signal blur, with potential loss of anatomical contrast and challenge statistical analysis (Vos et al., 2011). Therefore, such filters are not generally adopted.

Novel strategies: Under the assumption that the image can be well described by a piecewise constant or piecewise linear function, Total Variation (TV; Rudin et al., 1992) and Total Generalized Variation (TGV; Knoll et al., 2011) regularization, respectively, can be used for the regularized extrapolation of k -space, thereby suppressing the spurious oscillations, while preserving the edges (Amartur et al., 1991; Constable and Henkelman, 1991). Such strategy relies heavily on a user-defined regularization constant and can quickly result in patchy - cartoon-like - images Block et al. (2008), but can easily be applied on individual dMRI images (Perrone et al., 2015; Veraart et al., 2016a).

A technique that is gaining popularity to suppress this artifact in an individual dMRI image is based on subvoxel-shifts to sample the ringing pattern at the zero-crossings of the oscillating sinc-function (Kellner et al., 2016). Indeed, within a local patch, the amplitude of the Gibbs ringing depends on the precise location of the anatomical edge relative to the sampling grid. A local re-sampling of the image using subvoxel shifts can be performed to achieve a sample of the zero-crossings instead of the peaks of the sinc function. The optimal re-sampling grid is determined by minimizing local total variations.

Practical considerations: The development of the above techniques and the public availability of code has definitely increased the awareness of the impact of Gibbs ringing on quantitative dMRI measures. However, further developments are needed to foster a more general applicability. The general applicability is challenged by the common use of partial

Fourier (PF) encoding, which can cause ringing artifacts of varying frequency and phase (Kellner et al., 2016). Extensions of the subvoxel shifts have been proposed for specific PF factors and convolutional neural networks have been developed (Muckley et al., 2021; Zhang et al., 2019) to tackle this problem. However, the solutions impose constraints, e.g. availability of complex data or a specific PF factors, preventing the general applicability at this stage.

Implausible signal maps – which show locations where the $b = 0$ signal becomes lower than diffusion-weighted signals – have been proposed for quality control of Gibbs ringing artifacts, i.e. ringing causing severe signal drops in the $b = 0$ image around sharp intensity changes particularly at CSF-tissue interfaces (Perrone et al., 2015; Tournier et al., 2011). An image showing the difference between pre- and post-correction can qualitatively be inspected to reveal problems with the correction. Automated quality assessment for Gibbs ringing correction is challenged by the complex interference between the shape and magnitude of the artifacts, the location of anatomical boundaries, and signal intensities.

Gibbs ringing correction is typically applied before any signal interpolation e.g. from motion/eddy current correction (Sections 2.7–2.9).

2.5. Noise distribution bias correction

Description and importance: Thermal noise is an intrinsic source of undesired signal fluctuations. In MRI, the measurement noise is Gaussian with standard deviation σ in the acquired complex k -space(s). However, in dMRI, one typically reconstructs the magnitude MR images prior to further analysis to avoid signal voids due to phase variations caused by e.g. subject motion, perfusion, respiration, cardiac pulsation, or field inhomogeneities (Fig. 5a). Magnitude MR data is noncentral Chi-distributed (Fig. 5b bottom) and the degrees of freedom depend on the number of coil elements, the parallel imaging method, and the applied reconstruction technique (Aja-Fernández et al., 2013; Dietrich et al., 2008; Gudbjartsson and Patz, 1995). The Sum-of-Squares combination of multiple complex-valued coil images would result in a noncentral Chi distribution in case of unaccelerated imaging or an approximate noncentral Chi distribution in case of accelerated imaging. However, in many widely-adopted cases, the multi-channel coil data is compressed in a single complex value prior to computing the magnitude image; for example in SENSE-like reconstruction or Adaptive Combine. In such cases, the noncentral-Chi distribution reduces to the more favorable Rician distribution (Fig. 5b top). Although at moderate to high SNR, a noncentral-Chi distribution can be well approximated by a Gaussian distribution; at low SNR, one observes a spurious SNR-dependent signal increase – the noise floor (Fig. 5b right). This effect cannot be removed by simple averaging magnitude MRI images to enhance the SNR. Indeed, whereas the average of Gaussian distributed signals is an unbiased estimator for the underlying signal A , the average of noncentral-Chi distributed signals \bar{S} exceeds the noise-free signal, with an SNR-dependent offset. For moderate SNR regimes, $\bar{S} \approx \sqrt{A^2 + L\sigma^2}$, with L the number of effective coils (Fig. 5b) (Aja-Fernández et al., 2013; Gudbjartsson and Patz, 1995)).

This signal bias propagates in all diffusion measures in an often non-trivial manner if the actual data distribution is not accounted for during model fitting. For example, the apparent diffusivities are underestimated, but to a greater extent in directions with lower SNR. Therefore, in diffusion tensor imaging (DTI), the MD is underestimated as a result of the noise bias, whereas the effect on FA depends on the b -value and SNR (Jones, 2004; Pierpaoli and Basser, 1996). Jones (2004) furthermore show that the noise floor can introduce an artificial correlation between FA and mean MD, which can bias statistical analyses if these measures are tested independently. The impact of such noise bias has also been observed in diffusion kurtosis imaging (overestimated kurtosis; Veraart et al., 2011)) and fiber tracking (more spurious peaks; Eichner et al. (2015)). The impact of the noise bias becomes increasingly important in quantitative dMRI and microstructure mapping, especially with recent developments of higher b -values, varying echo times, or higher spatial resolutions.

Approaches prior to and brought by the HCP: A conventional strategy to minimize the propagation of the signal bias to the parameters of interest is the use of the Maximum Likelihood estimator (MLE). In this parameter estimator, one optimizes the goodness of fit of a statistical model to the measurements, which includes both the diffusion model and the expected probability distribution function of the measurements (i.e. noncentral-Chi in the case of magnitude images). The MLE has optimal (asymptotical) statistical properties, both in terms of accuracy and precision (Sijbers et al., 1998). In case of additive Gaussian noise, the MLE and nonlinear least squares (NLS, which minimizes the sum-of-squared residuals) are mathematically equivalent. Since image preprocessing might alter the shape of the data distribution, other parameter estimation strategies were proposed. An example is to estimate a diffusion model's parameters by incorporating the Rician noise distribution assumption in a fully probabilistic framework (Jbabdi et al., 2012). Instead of including the entire probability distribution function, one can only already reduce the signal biases by “offsetting” the model prediction in the object function of a nonlinear least-squares estimator using the analytical expression of the expectation value operator associated with the appropriate noncentral-Chi distribution (Fig 5c) (Jones, 2004; Veraart et al., 2013). Due to the central limit theorem, the expectation value is more robust to data interpolation associated with image preprocessing than the full data distribution.

Alternatively, one can correct the diffusion-weighted signal prior to model fitting. Ideally, the data distribution is transformed into a Gaussian distribution, centered around the noise-free signal amplitude A and with variance that is equal for all diffusion-weighted measurements. Such approach has been presented (Koay et al., 2009), but relies on an accurate estimation of the \bar{S} and prior knowledge of the noise level. A smoothed spline model (Koay et al., 2009) or spherical harmonics presentation (Veraart et al., 2013) has been suggested to estimate \bar{S} . Noise estimation has also become more accurate and various techniques are widely available (e.g. Coupé et al., 2010; Manjón et al., 2015; St-Jean et al., 2020; Veraart et al., 2016b). A variant to this technique proposes to remove the noise-induced offset, without altering the noise variance (Koay et al., 2006). However, again, \bar{S} and σ must be estimated accurately and unfortunately, these correction techniques suffer from poor error propagation at low SNR. This and the dependence on an accurate estimation of the noise level have challenged a wide use of this preprocessing step.

Novel strategies: If the complex MRI data is accessible, one can estimate the background phase and perform a phase shift to compute a real-valued image with the relevant diffusion-contrast and an imaginary image mainly containing noise which might be discarded. Since the noise in the real- or complex-valued image is Gaussian, the problem of the noise bias is totally avoided (Cordero-Grande et al., 2019; Eichner et al., 2015). Of course, the estimation of the background phase is challenging since it is dependent on unpredictable bulk flow. Eichner et al. (2015) proposed to estimate the background phase with a total variation approach assuming piecewise smoothness of the signal. Such approaches assume knowledge about the smoothness of the background phase (i.e. setting regularization parameters), and suboptimal choices can lead to ineffective correction and even signal outliers and bias beyond that introduced by using magnitude signals (Pizzolato et al., 2016). Further development, including the estimation of the optimal degree of regularization based on noise-variance estimates, are being proposed and will further improve the accuracy of real- or complex valued diffusion MRI (Pizzolato et al., 2020).

Practical considerations: The strategies discussed here rely on a reliable estimate of the noise standard deviation and hence their general applicability is challenged by the dependency of the signal distribution to the image reconstruction technique, especially in case of parallel imaging. Coil-correlations and parallel imaging cause the noise to be spatially varying (non-stationary).

The acquisition of ‘noise maps’, which are additional images with the same settings (e.g. echo time (TE)/ repetition time (TR)) but with

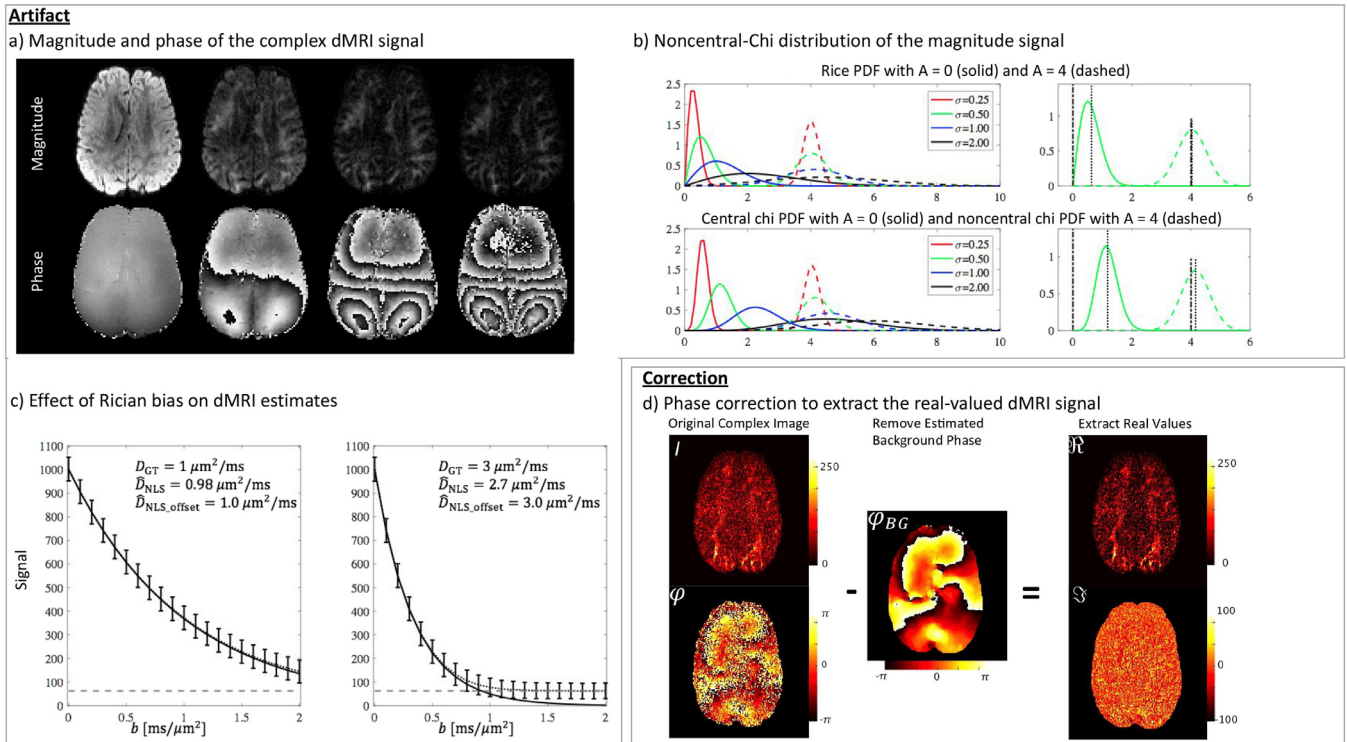


Fig. 5. Rician bias. **a)** Magnitude and phase data for increasing b -values ($[1, 3, 5, 7]$ $\text{ms}/\mu\text{m}^2$). The same structures are roughly visible in the different magnitude images, but the phase images look vastly different. **b)** Left: Rice (top) and noncentral-Chi (with 3 effective coil elements) distributions for different noiseless underlying signals A and noise standard deviation σ . Right: Selected distributions with $A = 0$ and $A = 4$ indicated by the dotted lines and first moment, or average value indicated by the dotted-dashed lines. The average is higher than the true underlying signal and is dependent on the SNR. **c)** Simulated signal decays (solid lines) as a function of b -value with ground truth diffusivities $D_{GT} = 1 \mu\text{m}^2/\text{ms}$ (left, e.g. representing WM) and $D_{GT} = 3 \mu\text{m}^2/\text{ms}$ (right, e.g. representing CSF). Rician noise was added with an SNR of 20 (dashed black lines and error bars indicate the mean and standard deviation across noise realizations per b -value). The grey dashed line represents the $\bar{S} = \sqrt{\pi/2}\sigma$ in case of a Rician distribution with $A = 0$ (which becomes a Rayleigh distribution). Whereas the left example shows only a moderate spurious signal increase, this is obvious in the right example. A nonlinear least squares (NLS) fit, which minimizes the sum-of-squared residuals $\sum_i (\bar{S} - S)^2$ between the measured signals \bar{S} and model-predicted signals S gives a bias estimate of the diffusivity, whereas an “offset” in the model prediction – i.e. minimizing $\sum_i (\bar{S} - \sqrt{S^2 + \sigma^2})^2$ taking into account the approximate signal bias (Jones, 2004) – reduces the bias. **d)** Background phase removal to compute real valued images. Figure adapted from Eicher et al. (2015), permission obtained through Rights Link.

all RF pulses turned off, is not always trivial in clinical settings and increases acquisition time. Other noise-characterization strategies have been developed of which some will be discussed in Section 2.6. Finally, the phase images needed to avoid the noise bias are not commonly provided in standard vendor sequences.

Automated quality assessment is challenged by the complex interference between the magnitude of the artifact and signal intensities, which vary spatially and across DWIs.

2.6. Denoising

Description and importance: Thermal noise can challenge the visual inspection of images, especially in areas with low or strongly attenuated diffusion-weighted signal. Moreover, the estimation of quantitative diffusion measures from the diffusion-weighted data might amplify the thermal noise. Although the thermal noise might be reduced by fitting well-conditioned diffusion models such as DTI, NODDI, or the Generalized Spherical Deconvolution Model (Sperl et al., 2017), many analysis strategies of dMRI data are highly susceptible to noise amplifications that lowers the sensitivity of dMRI data and the visual or statistical analyses thereof.

Approaches prior to and brought by the HCP: A widely adopted strategy to suppress noise is Gaussian smoothing in which the signal or diffusion-signal profiles across neighboring voxels are averaged. Unfortunately, together with the noise, sharp edges and anatomical details

might fade as well. To avoid blurring of fine anatomical detail, edge-preserving strategies have been implemented in which voxels are selected adaptively (e.g. POAS (Becker et al., 2014; 2012) and anisotropic filtering (Ding et al., 2005; Krissian and Aja-Fernández, 2009)) and/or non-locally (e.g. SUSAN (Smith and Brady, 1997), nonlocal means (Manjón et al., 2010; Wiest-Daesslé et al., 2008) or Nonlocal spatial and angular matching (St-Jean et al., 2016)), based on various similarity measures. Whereas adaptive smoothing aims to average over voxels within connected homogeneous regions, nonlocal strategies allows for signal averaging over disconnected voxels.

Novel strategies: The recent developments in image acquisition and reconstruction have been imposing additional challenges and constraints for image denoising. For example, the thermal noise level is typically spatially varying in routine dMRI. A wide variety of image denoising techniques have been adopted, adapted, and developed to overcome such challenges. The techniques can be broadly classified in regularization-, transformation-, and machine learning-based techniques.

First, total variation regularization has already been discussed in the context of Gibbs ringing correction. Although such techniques can suppress local signal fluctuations due to thermal noise while preserving sharp edges, the quality of the denoising strongly depends on user-dependent variables (Rudin et al., 1992). A low-rank image model and edge-preserving regularization terms are characteristic features of this strategy (Lam et al., 2014).

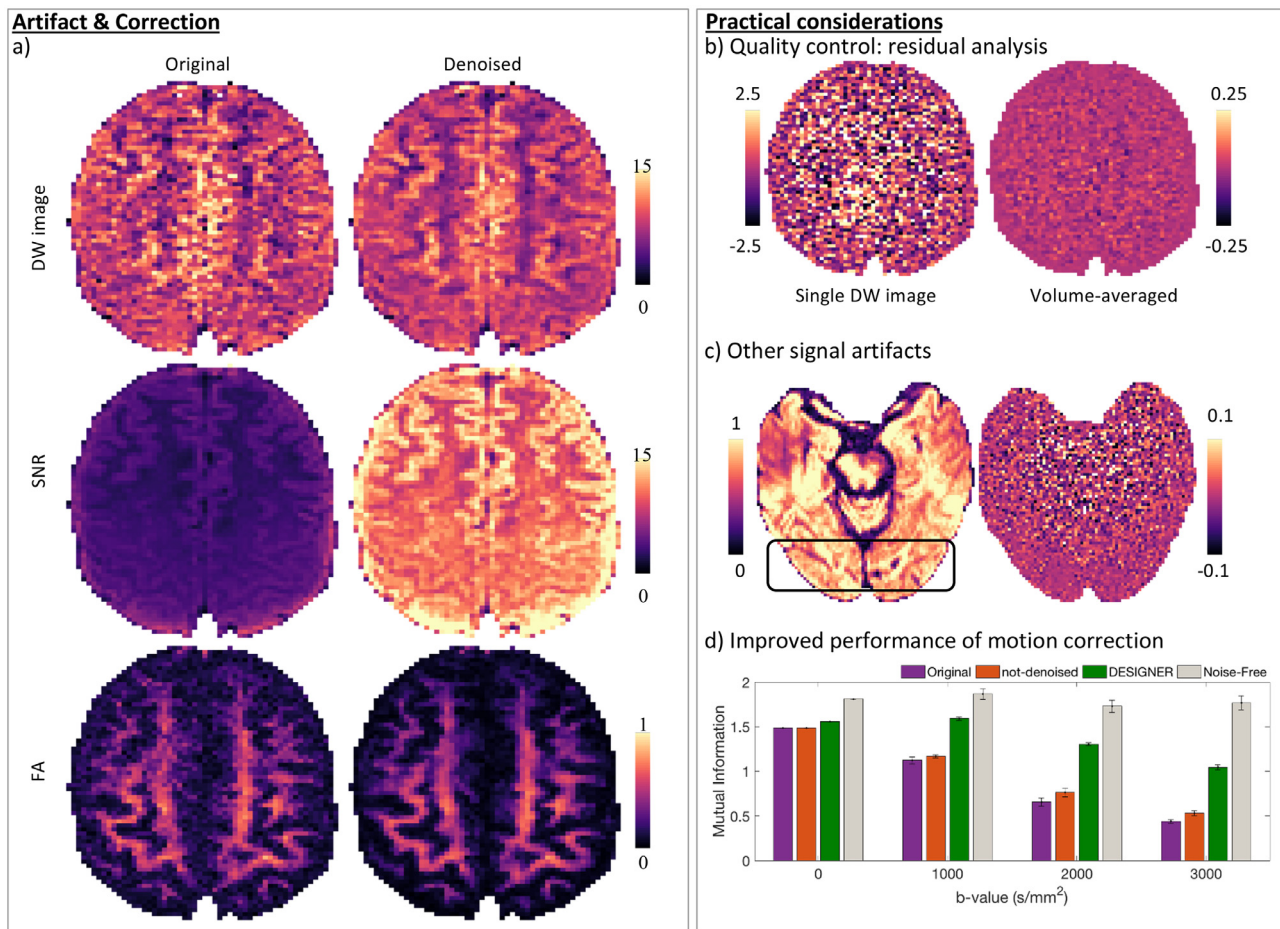


Fig. 6. Denoising: **a)** One slice of one DW image, the SNR map, and the FA map from a single, arbitrarily chosen dMRI data set with $b = 1000 s/mm^2$, is shown, before and after denoising with a state-of-the-art technique. **b)** the difference maps between the denoised and original data are spatially uncorrelated and zero-centered, and spatially varying trends should reflect the g -factor instead of anatomical features. Unfortunately, the Rician bias might interfere with this quality control since low SNR regions such as the ventricles might present themselves in such maps. **c)** Denoising is here presented as the reduction of thermal noise only. Other signal artifacts, e.g. a chemical shift artifact, will be unaltered during denoising. **d)** The denoising performance is best without preceding data interpolation or noise manipulation steps. However, denoising might also improve the performance of subsequent steps such as motion correction (Ades-Aron et al., 2018). The performance of motion correction of a multi-shell DW data sets is here quantified using the mutual information between DW images and a reference $b = 0$ image.

Second, one can transform the data into a sparse basis representation prior to filtering the noise. Such strategies often preserve anatomical detail better by relying on the physical properties of thermal noise. Popular examples of such sparsifying transformations include the wavelet transformation (Wiřtstam et al., 2006) and the Principle Component Analysis (PCA) technique. Denoising based on PCA has been gaining popularity in recent years. Under the assumption that dMRI data shows a high degree of redundancy (oversampling the q -space) only a few principle components are sufficient to describe the dMRI data accurately. The removal of the pure-noise principle components results in the desired noise reduction without removing anatomical detail or edges (Manjón et al., 2013). The automated identification of the pure noise principle components is enabled by adopting principles of Random Matrix Theory, i.e. the Marchenko Pastur distribution is a signature of thermal noise in the PCA eigenspectrum (Marchenko and Pastur, 1967; Veraart et al., 2016b). Other related methods for low-rank matrix denoising have been proposed, including statistical/information theory approaches that derive optimal asymptotic matrix denoisers (Cordero-Grande et al., 2019; Donoho et al., 2014; Gavish and Donoho, 2017; Ma et al., 2020b; Moeller et al., 2021; Nadakuditi, 2014).

Third, various supervised, unsupervised, and self-supervised machine learning-based techniques have been developed and evaluated for the denoising of dMRI data. For example, (Muckley et al., 2021)

used a convolutional neural network (CNN) for artifact removal in dMRI (complex and magnitude) data. It makes use of encoder-decoder strategies to train on simulated MRI and on synthetic non-MRI images. Next, Patch2Self (Fadnavis et al., 2020) is a recent unsupervised and self-supervised denoiser that makes a weak assumption on the noise, i.e. it assumes the noise is statistically independent across the 3D volumes of 4D dMRI data. Noise are uncorrelated “random fluctuations” in the signal components. Unlike the previous approaches which make an assumption on the signal such as low-rank (PCA-based), smoothness (total variation) or repetition (NLMean, BM3D), Patch2Self strictly makes an assumption on the noise and not the signal.

The idea of using statistical independence was used in Noise2Noise (Lehtinen et al., 2018), where two independent measurements of the same entity were required to do the denoising. Noise2Self (Batson and Royer, 2019) laid out a theoretical foundation of how one could learn a self-supervised denoiser by proposing the theory of J -invariance. Both approaches proposed using deep CNNs for denoising 2-dimensional images. Under the assumption that each DW volume can be represented accurately as a linear combination of all other DW volumes, Patch2Self promotes the use of this denoising strategy to 4D DW data sets.

Practical considerations: The general applicability strongly depends on the denoising strategy. Overall, denoising is more efficient in the absence of noise correlation that might be imposed during image re-

construction or image preprocessing. Therefore, there has been a trend towards integrating denoising with image reconstruction (Haldar et al., 2013) or apply it on the complex data, prior to computing the magnitude MR signal and further image preprocessing (Cordero-Grande et al., 2019; Moeller et al., 2021; Wirestam et al., 2006). Denoising is overall widely applicable and does not impose constraints on diffusion acquisition. However, PCA based denoising algorithms should only be applied if “large” data sets with at least 30 diffusion weighted images are available (Veraart et al., 2016b). Patch2Self has been applied successfully with datasets with small number of gradient directions. For example, in Schilling et al. (2021) 15 gradient directions were used.

After the completion of the denoising step, it is advised to evaluate the residual maps. Ideally, residuals are spatially uncorrelated and zero-centered, and spatially varying trends should reflect the g-factor instead of anatomical features. Unfortunately, Rician biases might challenge this quality control.

Overall, applying image denoising early in the pipeline might be beneficial for performance of the denoising itself and for the improved performance of the subsequent steps (Veraart et al., 2016b) to avoid altered noise characteristics due to image interpolation (Rohde et al., 2005).

2.7. Between-volumes motion correction

Description and importance: A typical dMRI dataset consists of N volumes whose voxel-wise intensities reflect properties of the water molecules’ displacement along each of the N sampled diffusion encoding settings. High Angular Resolution Diffusion Imaging (HARDI) and multi-shell acquisitions are now routinely performed, especially in experimental settings, and represent the basic requirements for most of the recently developed microstructural mapping methods (Alexander et al., 2019). Recent advances in EPI-based dMRI data acquisition techniques (e.g., multi-band imaging) have enabled researchers and clinicians to acquire data of unprecedented quality in a fraction of the time when compared to standard serial/interleaved slice-wise protocols (Sotiropoulos et al., 2013c). However, subjects are still required to lie in the scanner for extended periods of time. Therefore, between-volumes subject motion is unavoidable (Fig. 7). If uncorrected, voxels will be misaligned across volumes, leading to, e.g., artifactually higher ADC estimates at the edges between brain tissue and CSF due to partial volume effects (Le Bihan et al., 2006b; Pierpaoli, 2010). Such biased model-based microstructural parameter estimates may lead to spurious results (Leemans and Jones, 2009) when, e.g., comparing two groups (Yendiki et al., 2014). Even though this section focuses on motion-induced misalignment between images, motion is continuous and can lead to misalignment between slices within an image and signal outliers (see sections 2.8 and 2.10 respectively).

Approaches prior to and brought by the HCP: Between-volumes motion correction and B-matrix rotation - which preserves the orientational information associated to each DWI upon realignment - (Leemans and Jones, 2009; Rohde et al., 2004) are often amongst the first stages of a dMRI data preprocessing pipeline. Prior to the HCP, most methods for retrospective motion corrections aimed at affinely registering (Jenkinson and Smith, 2001) each acquired volume to a reference $b = 0$ image using a correlation ratio cost function. However, when dealing with dMRI data, the assumption that volumes are identical except for a rigid geometric transformation does not hold. Distortions caused by other artefactual sources, such as eddy currents and other off-resonance fields (see sections 2.9 and 2.11), make registration very challenging. Moreover, between-shells and between-directions differences in diffusion-weighted contrast make the choice of a similarity function that drives between-volume registration not easily addressable (Rohde et al., 2004). This is especially true when dealing with high b -value data, where most of the brain outline and tissue boundaries are almost indistinguishable. Mohammadi et al. (2015) try to address this by registering the DWIs per b -shell to a median image, and Zhuang et al. (2013) only register images that are close in orientation and b -value.

Recent methods try to overcome registration issues by incorporating predictive modelling approaches into dMRI motion-induced distortion correction frameworks. Such approaches make a prediction about how each of the acquired dMRI volumes “should look”, given its b -vector, and the residuals between the observed and the predicted data can be obtained. This “error-signal” can then be used to iteratively update the estimate of the motion parameters describing the subject’s position. Some methods have attempted to derive such predictions either using modelling-based approaches, such as the DT (Andersson and Skare, 2002) or by comparing neighbouring diffusion encoding orientations (Zhuang et al., 2006). However, predicting any dMRI encoding from a DT fit carries the intrinsic limitations of the DTI approach (e.g., complex fibre configurations such as crossing or kissing cannot be resolved) and leveraging on neighbouring diffusion encoding orientations make the quality of the predictions dependent on, e.g., angular sampling. Ben-Amitay et al. (2012) predict DWIs at higher b -values using the composite hindered and restricted model of diffusion (CHARMED), with parameters derived from a DT fit at lower b -values. Irfanoglu et al. (2017) predict the DWI signal of a given N^{th} volume using the MAP-MRI propagator representation (Özarslan et al., 2013), from all the previously corrected $N - 1$ volumes. Nilsson et al. (2015) suggest that DT-based predictions may negatively impact registration in regions of CSF-partial voluming, and adjust for this and artificial diffusion anisotropy in grey matter. This approach predicts data based on a stretched-exponential representation and is compatible with diffusion encodings beyond conventional pulsed gradient spin echo (PGSE) acquisitions. FSL’s EDDY (Andersson and Sotiropoulos, 2016), predict the data as a linear combination of the observed data using a Gaussian Process (GP), whose hyperparameters are estimated directly from the data (Andersson and Sotiropoulos, 2015). Such hyperparameters determine the smoothness of the dMRI signal, parameterized as a function of b -value and diffusion gradient direction. The GP embedded within EDDY solves issues related to model-based predictions by working directly on the raw dMRI signal and by using all the data that has been acquired (Andersson and Sotiropoulos, 2015).

Novel strategies: Christiaens et al. (2021) use a model-independent spherical harmonics and radial decomposition (SHARD) signal representation to obtain and output predictions. The retrospective motion correction techniques brought by the HCP and their more recent extensions (see, e.g., Section 2.8) allow to reliably estimate between-volumes motion parameters. Recently, real-time prospective motion correction strategies have been developed (Maclaren et al., 2013). These techniques allow to directly measure the amount of motion by either using imaging-based navigators (Alhamud et al., 2012) or optical tracking systems (Aksoy et al., 2011; Forman et al., 2011; Zaitsev et al., 2006). The latter strategy typically tracks a marker attached to the subject and it can accurately and precisely measure motion irrespective of the sequence being used. Marker-based methods typically require an initial cross-calibration step to measure the position and orientation of the tracking marker with respect to the magnet isocenter. Moreover, they require the subject to be compliant, i.e., to lie as still as possible in order not to hide the marker from the tracking camera. This may be hard to achieve with uncooperative subjects such as patients or children. Recently, novel marker-less optical tracking strategies relying on facial features have been developed (Berglund et al., 2021). Although these methods are still being evaluated and have not been widely adopted yet, they offer promising avenues for motion correction in less compliant subjects. Finally, 3D-printed personalized head cases can be used to minimize subject motion, although some studies draw into question their efficacy (Jolly et al., 2020).

Practical considerations: Between-volumes motion correction is a processing step that should always be performed when analysing *in vivo* dMRI data, irrespective of the species being scanned. To ensure optimal results from those methods that rely on model-free predictions of the dMRI signal, a “minimum” b -shell dependent number of diffusion encoding directions should be sampled, i.e., at least 10 directions for a

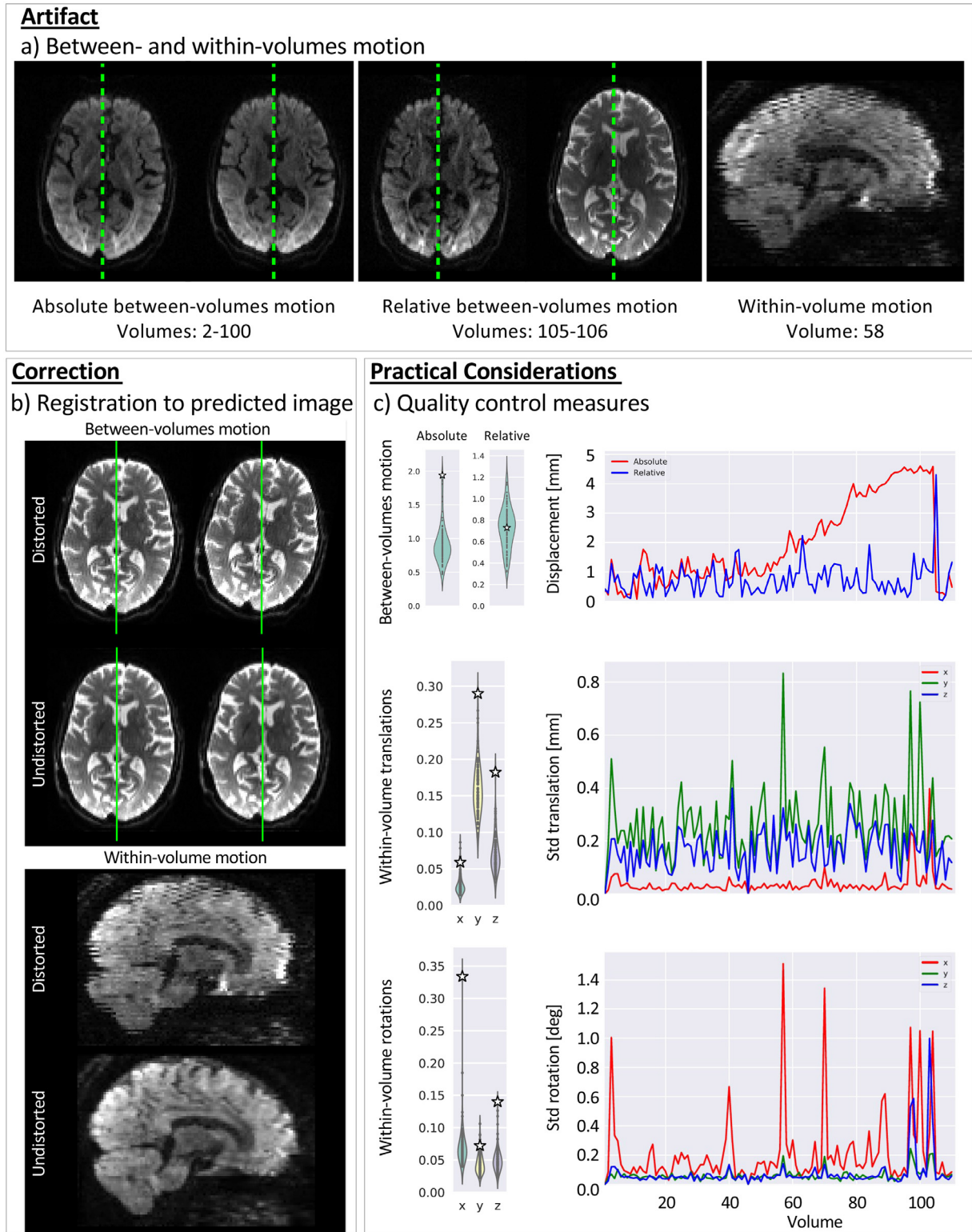


Fig. 7. Absolute and relative between-volumes and within-volume motion effects. **a)** While between-volume motion affects the displacement of whole volumes, the within-volume effects can be recognised by the tell-tale zigzag patterns across axially acquired slices. **b)** Both motion-induced distortions can be corrected successfully using recent preprocessing frameworks such as FSL's eddy, which has been used to correct the two examples provided (bottom left column). **c)** After running motion correction and estimating between and within volumes translations and rotations, their averages can provide the researcher with useful QC measures. Violin plots for 100 preprocessed UK BioBank subjects are shown, highlighting the distribution of each metric. The plots show the volume-wise values of each metric for the subject represented by the white star on the violin plots. Figure modified from (Bastiani et al., 2019b).

b -value of 1500 s/mm^2 and 30 directions for a b -value of 5000 s/mm^2 . For techniques that rely on a model or representation, the acquisition experimental design should be compatible with the model used in correction. For example, the majority of correction strategies expect dMRI data that are sampled on b -shells.

Assuming rigid body motion between the reference volume and each acquired volume, a total of six between-volumes motion parameters (three translations, three rotations) can be estimated when correcting for motion-induced artifacts, where one should keep in mind that interactions with other distortions make the misalignment much more complex (sections 2.9 and 2.11). Useful summary quality control (QC) metrics can be obtained by averaging their values across the whole acquisition. Another summary measure of “total motion” can be calculated by averaging voxel displacement across all voxels within the brain mask. Such voxel-wise average voxel displacement summarizes both rotations and translations at each voxel with a single scalar. Absolute (w.r.t. a reference volume) and relative (w.r.t. the previous volume) total motions can be calculated for each volume, and their averages across all volumes can provide very useful summary QC metrics (Fig. 7). Nilsson et al. (2015) computed averaged translation and rotation parameters across all subjects in a study to evaluate preprocessing performance, and suggested that such motion parameters should average to zero in a population.

Alternatively, QC based on DTI-based measures, such as FA uncertainty and the orientation uncertainty of the first eigenvector, and sensitivity and specificity of probabilistic tractography group results have been proposed (Taylor et al., 2016). However, these may offer difficult to interpret insights into the performance of the motion correction step, as they probe quantities further down the processing line that base themselves on several assumptions to link the dMRI signal with underlying anatomical substrates.

2.8. Within-volume motion correction

Description and importance: In dMRI data acquired in challenging scenarios, such as when scanning neonates, children or patients, a tell-tale zig-zag outline (Fig. 7) reflecting slice misalignment is often present (see, e.g., Bastiani et al., 2019a). This artifact is a consequence of significant subject motion happening between the acquisition of the first and the last slice of a single dMRI volume. If not accounted for, slices misalignment may bias between-volume motion correction and, subsequently, microstructural parameter and structural connectivity estimates from dMRI data.

Approaches prior to and brought by the HCP: Current practice to correct for motion-induced artifacts mostly relies on the assumption that subjects will lie still during the acquisition of all the slices within a volume and will only consistently move between the acquisition of two consecutive volumes. This is why the vast majority of methods only focus on between-volume motion correction and aim at aligning individual volumes to a reference one using, e.g., an affine registration (Jenkinson et al., 2002). Recent work based on fMRI data simulation has shown that this assumption does not hold (Beall and Lowe, 2014). Therefore, slice-to-volume-based registration methods have been implemented to correct within-volume motion-induced artifacts by, e.g., combining it with temporal head motion tracking using a Kalman filtering approach (Marami et al., 2016). However, most approaches do not consider other off-resonance sources (Bannister et al., 2007; Kim et al., 1999), such as eddy currents, or have only considered susceptibility-induced distortions (Yeo et al., 2008) as they were developed to deal with fMRI data.

Novel strategies: Few studies have focused on within-volume motion correction. When correcting neonatal (Bastiani et al., 2019a; Christiaens et al., 2021) or fetal (Marami et al., 2017) dMRI data, the benefit of incorporating a slice-to-volume movement by means of simultaneous multi-slice acquisitions (Marami et al., 2019), an intermediary volumetric model (Jiang et al., 2007) or through intersection matching

(Kim et al., 2010) has been shown. A recent extension of FSL’s EDDY takes a holistic approach, trying to incorporate within- and between-volume motion, eddy-currents and susceptibility-induced artifacts correction into a single coherent modelling framework (Andersson et al., 2017).

Practical considerations: Correcting for within-volume motion-induced slice misalignment has the greatest benefits when dealing with subjects who move a lot or when acquiring a single volume takes a long time because, e.g., multi-band acquisition is not available. However, simulated data suggests that when within-volume motion is not significant, correcting for it does not bias the results (Andersson et al., 2017). Promising results have been obtained with this method (Oldham et al., 2020), suggesting that this step can be used when preprocessing in vivo human dMRI data even when the data exhibits minimal within-volume motion. A practical consideration is that such corrections are computationally heavy and at the time of writing, the implementation in FSL EDDY requires/benefits from access to a GPU.

Assuming rigid body motion of each slice or block of simultaneously acquired slices (if SMS/MB is used), a total of six within-volume motion parameters (3 translations, 3 rotations) can be estimated by those methods that incorporate a slice-to-volume model. Useful summary QC metrics can be obtained by averaging the standard deviation of each parameter calculated across the slices/groups of a volume (Fig. 7), which quantifies the amount of subject movement within that volume (Bastiani et al., 2019b).

2.9. Eddy current-induced distortion correction

Description and importance: To maximise both the signal- (SNR) and contrast-to-noise ratios (CNR) in a classical Stejskal-Tanner (ST) dMRI experiment using EPI, the two identical diffusion encoding gradients should be played at their maximum amplitude in the shortest possible time. Such rapidly changing magnetic fields induce eddy currents in the MR scanner conducting elements. The eddy currents will in turn generate a magnetic field, which is known as an eddy current-induced off-resonance field. The eddy current-induced gradient will combine with the spatial encoding gradients and will slightly change the expected resonance frequency. All these effects will result in phase encoding (PE) direction-dependent image distortions, such as scaling, shearing and translation, which will be unique to each diffusion-encoding setting. When not properly accounted for, eddy current-induced distortions can lead to misalignment and biased estimates of microstructural parameters such as, e.g., spuriously high FA values at the edge of the brain (Pierpaoli, 2010).

Approaches prior to and brought by the HCP: Advancements in hardware and data acquisition techniques relying on, e.g., in-plane parallel imaging (Larkman and Nunes, 2007), help to reduce eddy current-induced distortions. One way to further reduce eddy current-induced distortions is to try and null the induced field completely by modifying the ST encoding, e.g. bipolar/twice-refocused gradients (Alexander et al., 1997; Finsterbusch, 2009; Reese et al., 2003). However, these modifications often result in increased echo times, which lead to a further drop in SNR. Another possibility is to try and measure the eddy current-induced distortions by using additional data (Jezzard et al., 1998), potentially collected from phantoms (Bastin and Armitage, 2000; Chen et al., 2006; Horsfield, 1999; Papadakis et al., 2000; 2005). These methods assume that eddy-current induced distortions can be predicted from a small set of measurements, enabling researchers to calibrate the MR scanner and minimise distortions. However, these methods do not account for the problems related with subject motion and may not ensure optimal correction if distortions change either slowly or suddenly over time.

Most retrospective image processing-based correction tools try to estimate the eddy current-induced field through affine registration, and are based on the assumption that eddy currents are only elicited in the gradient coils, resulting in a field that can be modelled as a simple com-

bination of linear gradients in the three primary directions (Bastin and Armitage, 2000; Jezzard et al., 1998; Papadakis et al., 2005). The in-plane shears, zooms, and translations along the PE direction can therefore be modelled using $3 \times N$ parameters, where N is the total number of acquired DWIs. Therefore, most early approaches for eddy-currents distortion correction employed an affine transformation model (Jenkinson and Smith, 2001; Mohammadi et al., 2010), which are still frequently used (Nilsson et al., 2015; Thompson et al., 2014). The total number of parameters can further be brought down to 9 for any given set of diffusion-weighted volumes when assuming that diffusion-encoding gradients distortions along the three principal axes are known (Andersson and Skare, 2002; Horsfield, 1999; Zhuang et al., 2006).

Finding a suitable distortion-free reference volume to which all distorted volumes can be retrospectively aligned to can be very challenging. This would typically be a non-diffusion-weighted $b = 0$ image, however, correction tools would need to account for the difference in contrast between such a volume and the DWIs, potentially with a suitable registration cost function (Rohde et al., 2004). Moreover, modern gradient coils, especially those reaching very high amplitudes, are not necessarily linear (Janke et al., 2004), making the linear model insufficient to describe the eddy current-induced fields (Rohde et al., 2004). For such data, a complete or parsimonious (derived from the Cartesian solutions to the Laplace equation (Rohde et al., 2004)) quadratic (or occasionally cubic) basis sets are used to model the distortions.

Previous works have tried to address the contrast similarity issue by suppressing the CSF signal in $b = 0$ images (Bastin, 2001) or by acquiring extra volumes at low b -value (Haselgrove and Moore, 1996). Other methods rely on signal extrapolation from low b -value shells (Irfanoglu et al., 2017; Nilsson et al., 2015) or rely on the acquisition of extra DWIs with opposing diffusion gradients (Bodammer et al., 2004) or PE directions (Embleton et al., 2010). These methods may result in significantly longer scan times, with the last two expecting the user to sample the same diffusion direction twice, assuming they will have linearly opposite distortion patterns. To overcome the limitations of the linearity assumption and potentially reduce scanning times, the novel strategy described in Section 2.7 can be used, i.e., by combining predictive modelling approaches with standard registration techniques, it is possible to predict diffusion-weighted signals from all the available data and refine, in an iterative fashion, the higher order (quadratic and cubic) eddy current-induced field parameters (Andersson and Sotiropoulos, 2016).

Novel strategies: The quest to achieve higher spatial resolution and diffusion weighting in dMRI has led to increasingly "signal-starved" acquisitions, which can prohibit robust correction of eddy current distortions in very low SNR images with image registration-based techniques. An alternate strategy that has been gaining popularity recently in research settings is concurrent field monitoring (Ma et al., 2020a; Wilm et al., 2015) using a field camera (Kennedy et al., 2018; Skope, 2019). These cameras are used to monitor the magnetic field dynamics during the EPI readout, which can retrospectively be used for distortion correction for highly diffusion-weighted acquisitions.

Practical considerations:

In this review, we mainly considered the primary effects of eddy currents, which are geometric distortions. However, the reader should note that as with other sources that alter the field such as gradient nonlinearities or concomitant fields, eddy currents also introduce a deviation from the prescribed diffusion synthesis. These changes in the B-matrix due to eddy currents are generally ignored and no dMRI preprocessing pipeline currently accommodates for their effects. However, the geometric distortions due to eddy current-induced off-resonance fields should always be corrected when acquiring dMRI data. Image-based techniques are widely available and represent the current de-facto standard. Some strategies (e.g. FSL EDDY) greatly benefit from acquiring reversed PE data and/or diffusion encoding directions that span the entire sphere and not just the half-sphere. However, to not sample the same diffusion information twice (i.e. \mathbf{g} contains the same diffusion information as $-\mathbf{g}$, the directions could be optimally distributed on the half sphere and half

the vectors replaced by their negations. Modification to the ST encoding may not always be available across all MR scanner vendors, while field-probing cameras require extra hardware components that are not typically provided with MR scanners.

Correcting for geometric deformations due to eddy currents should be accompanied by modulating the signal intensity in a voxel according to its change in volume upon deformation (Rohde et al., 2004). The Jacobian matrix describes the deformation from the distorted image to the undistorted image, and the associated volumetric change is given by its determinant. Omitting to modulate the signal intensity by the Jacobian determinant can lead to a significant bias in dMRI estimates (Jones and Cercignani, 2010).

Most retrospective image processing-based correction tools model the eddy current-induced off-resonance field using a low order polynomial (typically second order). Using this approach, it is possible to derive QC measures by, e.g., computing the standard deviation of the three coefficients of the first order terms across the whole acquisition (Bastiani et al., 2019b). This is a measure that quantifies the volume-to-volume variability in eddy current-induced distortions across the scan. It reflects a combination of the magnitude of the eddy current-induced off-resonance fields and the bandwidth in the PE direction. Alternatively, visual QC can be performed by looping through the preprocessed volumes, looking for residual distortions across three orthogonal planes (Tournier et al., 2011).

2.10. Outlier detection

Description and Importance: Outliers are typically defined as signal intensities that significantly differ from the expected behavior based on other observations, and do not reflect the anatomically modulated water diffusion process. Outliers may occur due to measurement variability (e.g. as a result of noise), but could also indicate more serious measurement errors. Signal errors can affect different dMRI measures in different ways and could significantly impact microstructural estimates, tractography, and group studies. For example, they could bias the estimated dMRI measures causing an artifactual decrease or increase in certain areas associated with outliers, or they could increase the variance of microstructural estimates impeding the statistical power to detect differences, where the former effect is likely larger (Walker et al., 2011). Moreover, outliers may impact patient- and control populations differently, leading to statistically significant results that can primarily be explained by the presence of outlier data (Yendiki et al., 2014).

Within-volume motion is an important source of outliers: gross movement – e.g. subject or physiological motion – that occurs during the diffusion encoding can cause severe signal dropout. In the typical case of linear gradients, signal dropout is associated with movement that has rigid rotation or linear shear components (Wedeen et al., 1994). The characteristics of the dropout in the case of rigid rotation depend on the magnitude and rotational axis of movement, the magnitude, direction, and timings of the gradients, and the imaging plane (Fig. 8a) (Andersson et al., 2016; Storey et al., 2007). Depending on the direction of the applied diffusion gradient, the second pulse will thus not be able to refocus the phase shift introduced during the first pulse even for static spins, i.e. there will be a phase gradient across the tissue (Storey et al., 2007; Wedeen et al., 1994). Following the properties of the Fourier transform, a linear phase variation (i.e. multiplying the phase with a complex exponential) across the tissue corresponds to a displacement of the data in k -space, and if this displacement is large enough, the signal in k -space may fall (partially) outside the sampled range. This will in turn lead to severe signal loss in the case when the phase change within a single voxel is greater than π (Fig. 8a). Such outliers typically become more prevalent at larger field-of-view (FOV) and higher b -values. The sensitivity to rotational motion is further exacerbated in the case of partial Fourier imaging of k -space, because even a small displacement of the echo in k -space may lead to the signal moving outside of the detected range (Fig. 8b). Note that translations in the period between two pulses

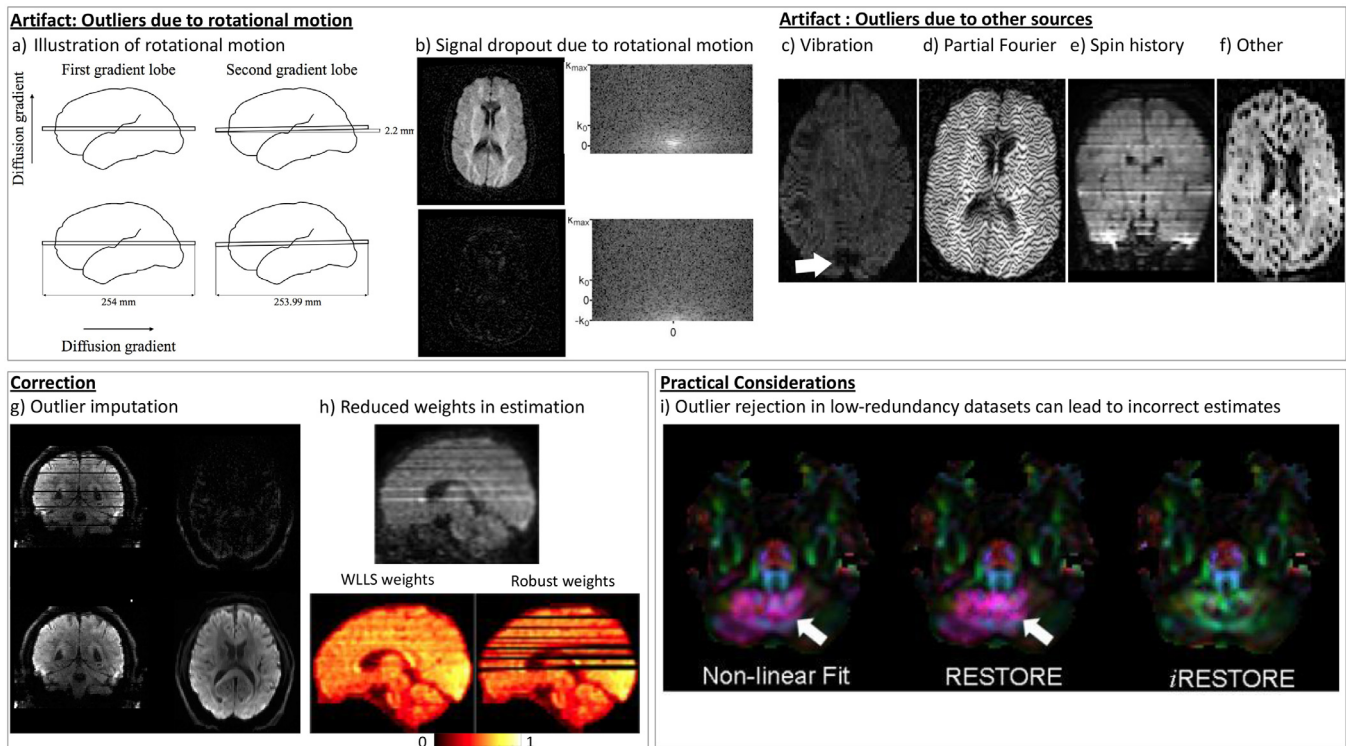


Fig. 8. Signal outliers. **a)** In the case of rigid rotation and depending on the direction of the applied diffusion gradient, there will be a phase gradient across the tissue of $\nabla\phi = \gamma\mathbf{G} \times \Omega\delta\Delta$ (Storey et al., 2007; Wedeen et al., 1994), where Ω is the angular velocity, and \mathbf{G} , δ and Δ define the magnitude, direction, and timings of the gradients. A linear phase variation across the tissue corresponds to a displacement of the data in k -space of $\Delta\mathbf{k} = \gamma\mathbf{G} \times \Omega\delta\Delta$, and if the phase change within a single voxel is greater than π this will lead to severe signal loss. Consider an example presented in Andersson et al. (2016) with an FOV of 256 mm with 2 mm voxels; a rotation of the subject around the left-right axis of 0.5° between the first and second PGSE gradient lobe would lead to a difference in position between the centres of the voxels on either side of an axial plane of $dz = 254 \text{ mm} \cdot \sin 0.5^\circ = 2.2 \text{ mm}$ along the inferior-superior axis, and $dy = 254 \text{ mm} \cdot \cos 0.5^\circ = 253.99 \text{ mm}$ along the anterior-posterior axis. If a rectangular diffusion gradient pair ($G = 30 \text{ mT/m}$, $\delta = 25 \text{ ms}$) is applied along the inferior-superior axis (top), there will be no phase shift within the slice as it is perpendicular to the gradient direction and all spins thus remain precessing with the same frequency. However, when the second lobe is played out the voxels on either side of the slice accrue a phase difference of $\Delta\phi = \gamma dz G_x \delta = 267.5 \text{ rad/s/T} \cdot 0.0022 \text{ m} \cdot 0.025 \text{ T/m} \cdot 0.025 \text{ s} \approx 445 \text{ rad}$, which corresponds to a pixel shift of $445/(2\pi) \approx 71$ pixels in k -space. This will move the signal out of the sampled window and lead to severe signal drop. In comparison, if the gradient pair is applied along the anterior-posterior axis (bottom), the phase shift of voxels on either side the slice following the first lobe will be $\Delta\phi = \gamma dy G_y \delta = 267.5 \text{ rad/s/T} \cdot 0.254 \text{ m} \cdot 0.03 \text{ T/m} \cdot 0.025 \text{ s} \approx 50959 \text{ rad}$, and the second lobe will refocus $\Delta\phi = \gamma dy G_y \delta = 267.5 \text{ rad/s/T} \cdot 0.25399 \text{ m} \cdot 0.03 \text{ T/m} \cdot 0.025 \text{ s} \approx 50957 \text{ rad}$, which only corresponds to a pixel shift of only $2/(2\pi) \approx 0.32$ in k -space. Figure adapted from Andersson et al. (2016). **b)** DWI and corresponding k -space acquired with Partial Fourier in the case of no motion (top) and motion (bottom). Figure adapted from Storey et al. (2007). **c)** Outliers due to mechanical vibration. **d)** High-frequency oscillations due to standard homodyne reconstruction in Partial Fourier imaging, figure adapted from Storey et al. (2007). **e)** Hyper-intensities due to spin history effects. **f)** Other intensity-outliers, data provided by BABA Center, Children's Hospital, HUS Imaging, Helsinki University Hospital, Finland. **g)** Imputation of outlier data (top) with signal predictions (bottom), figure adapted from Bastiani et al. (2019b). **h)** Outliers in a DWI (top) and reducing their weight in parameter estimation (bottom); left bottom shows the weights if a normal weighted linear least squares (WLLS) estimator is used, right bottom shows the weights informed by a robust outlier detection procedure. Figure adapted from Sairanen et al. (2018). **i)** Not constraining or informing outlier rejection in low-redundancy datasets can lead to the convergence to an incorrect solution. Figure adapted from Chang et al. (2012).

would cause a spatially constant phase and thus theoretically no signal loss.

Besides rigid motion, regional signal outliers can also occur due to other types of motion such as physiological processes (e.g. cardiac induced pulsation and respiratory motion) and scanner vibrations. Walker et al. (2011) found an increased extent of outliers in regions affected by cardiac pulsation, such as the cerebellum, genu, and splenium of the corpus callosum at $b = 1100 \text{ s/mm}^2$. Pannek et al. (2012) only found outliers in the cerebellum, ventricular and insular regions at $b = 1000 \text{ s/mm}^2$, while at higher b -values ($b = 3000 \text{ s/mm}^2$) outliers were also found within the corpus callosum and posterior limb of the internal capsule, raising the question whether cardiac pulsation is the main cause. Mohammadi et al. (2013) performed peripheral measurements of the subjects breathing and cardiac pulse and found that physiological effects were most prominent in the cerebellum, basal brain areas, extremities of the cortex, and proximity of ventricles, and they found an associated bias in FA in the brainstem between 3 – 5%. Scanner vibration-induced outliers can occur due to the switching of strong diffusion gra-

dients, leading to low-frequency mechanical resonances of the system and table which can be transferred to the subject (Berl et al., 2015; Gallichan et al., 2009). Such mechanical vibration can manifest as localized signal loss when the diffusion gradient has a large component in the left-right direction, presumably due to nonrigid rotational motion in the transverse plane.

In addition to slice-wise or regional signal drops, motion can also generate other types of outliers: common reconstruction algorithms in the case of partial Fourier imaging estimate the phase modulation from the center of the k -space (i.e. using a low-pass filter), but if the echo has moved outside this central range this can lead to severe outliers in the form of high-frequency oscillations in the image (Fig. 8d) (Storey et al., 2007). Spin-history effects can occur when the time between excitation of consecutive slices is short and motion causes them to overlap, e.g. leading to signal hyper-intensities (Fig. 8e) (Bastiani et al., 2019a).

Other artifacts beyond motion can result in signal outliers, e.g. those described in this review if not appropriately corrected, but also artifacts that are difficult or sometimes even impossible to correct with image

processing techniques such as the presence of a foreign metal body (e.g. surgery clips, retainers), or remaining chemical shift artifacts where the signal from fat appears spatially displaced along the phase encoding direction because of its different resonance frequency leading to artificial signal changes (usually seen as a 'band' from fat below the skin in brain imaging). Outliers may furthermore be hardware-related, e.g., caused by temporal scanner instabilities or spike noise, i.e. an erroneous point in k -space that accentuates a particular spatial frequency and reflects itself as parallel lines in the image. External factors such as electromagnetic interference and vibrations can also introduce signal errors; while proper RF shielding aims to reduce the former, the latter is not always easily avoided in the case of nearby building- or transport sites (e.g. metro).

Approaches prior to and brought by the HCP: Traditionally, images with severe outliers were simply removed upon visual inspection, but more advanced approaches have been proposed since. Cardiac gating during acquisition has been adopted in several studies to avoid imaging during those periods of the heart cycle with the greatest motion (Nunes et al., 2005; Skare and Andersson, 2001), but at the cost of increased scan time and varying temporal gaps between slice acquisitions, which can in turn lead to e.g. different effects of signal relaxation (Mohammadi et al., 2013).

Processing strategies to correct for outliers commonly consist of an identification and amelioration step, and often either target slice-wise or voxel-wise outliers. Slice-wise outlier detection is typically performed before any motion correction, as outlying slices become interpolated across multiple slices. The algorithm of Liu et al. (2010) as implemented in DTIPrep (Oguz et al., 2014) and DSI Studio (Yeh, 2021) computes the normalized correlation between successive slices of a DWI, defined as the pixelwise cross correlation normalized by the square root of the autocorrelation of the slices. Across DWIs, they assume the normalized correlation at the same slice-location to be normally distributed, and slices significantly deviating from the mean (i.e. α times the standard deviation) are flagged. Li et al. (2013) perform a morphological closing operation (i.e. a dilation followed by an erosion) on each DWI along the slice-select direction, and compute the difference with the original image (the inter-slice intensity discontinuity or ISID). Anatomical discontinuities are avoided by subtracting the ISID of a single DWI from the average ISID across all DWIs, and this approach is implemented in DTIStudio (Jiang et al., 2006). Although the closing operation can reveal more localized outliers, Marami et al. (2016) use this to detect motion-corrupted slices if the mean intensity in the difference was outside the interquartile range (IQR) of the mean of all slices. Zhou et al. (2011) identify outlier-slices based on their local textural features.

Voxel-wise outliers are typically detected by using the information across DWIs in a robust fitting procedure. The popular Robust Estimation of Tensors by Outlier Rejection (RESTORE) algorithm (Chang et al., 2005) iteratively fits DTI on the data using nonlinear least-squares, each time adjusting the weights of potential outliers. Specifically, the influence of data points with residuals far beyond the noise standard deviation is reduced using the Geman–McClure M-estimation technique (Geman, 1987; Mangin et al., 2002), and outlier measurements are finally identified based on the residuals. Chang et al. (2012) propose informed RESTORE (iRESTORE) based on the notion that physiological noise primarily results in signal dropout, and at each iteration the data point with the maximum negative residual is excluded. This prior information is beneficial when detecting physiological noise artifacts in datasets with relatively few directions. Zwiers (2010) incorporates neighborhood and slice-wise information into a different weighting strategy to increase robustness. Robust fitting approaches have also been developed for higher angular resolution data and representations, e.g. spherical harmonics (Pannek et al., 2012) and spherical deconvolution (Parker et al., 2013). The use of dMRI models or representations require the data to be co-registered but voxel-wise outliers become interpolated across the neighborhood, and outlier detection or weight computation is ideally performed on non-interpolated data (Morris et al., 2011; Zwiers,

2010). Farzinfar et al. (2013b) compare the entropy of the estimated fiber orientation distribution across the brain with learned entropy values from a training set of artifact-free samples, with the aim of detecting vibration artifacts which typically generate spurious left-right connections and thus lower entropy.

After detection, outliers can be handled in different ways. DWIs containing outliers can be removed completely based on the detection criteria (e.g. in the case of one (Liu et al., 2010) or multiple (Marami et al., 2016) outlier slices). Although some authors argue that the gain of local compared to global outlier rejection does not outweigh the increased complexity of dealing with locally varying numbers of data-points (Oguz et al., 2014), the affected DWI can still contain relevant information despite the presence of outliers. Several approaches therefore discard outlier measurements voxel-wise or slice-wise, e.g. when the residuals of a fit exceed a certain threshold (Chang et al., 2005; Collier et al., 2015; Tax et al., 2015). Factors causing outliers can also be included as regressors in the fit. Mohammadi et al. (2013) incorporate regressors in DT-fitting to explain the measured physiological effects, and show that the noise in the fit is greatly reduced. To address scanner vibrations, Gallichan et al. (2009) include an empirical approximation of their effect on DWIs as a regressor, while Farzinfar et al. (2013b) iteratively remove DWIs that lead to the largest improvement in fiber-orientation entropy. If reversed-PE data is available, the signal may be lost in one PE direction due to the shift in k -space but not in the other, and Mohammadi et al. (2012a) weight the two images according to their respective tensor-fit error. Finally, spatial regularization can be included to penalize discontinuity between estimates in neighboring voxels/slices (Filiard et al., 2007).

Novel strategies: With multi-shell data becoming more prevalent, outlier detection and amelioration techniques have been extended to accommodate data across b -values. Tax et al. (2015) extend RESTORE to DKI, which is more susceptible to data artifacts, and propose REKINDLE as a faster linearized version. REKINDLE takes into account the heteroskedasticity (i.e. the variance of each measurement becoming different after taking the logarithm to linearize the DTI/DKI equation) by transforming variables so that they obtain a homoskedastic nature in each iteration. Collier et al. (2015) take a slightly different approach where they correct the estimate of the standard deviation for heteroskedasticity and use this to determine the weights in the linearized fitting. FSL integrates outlier detection with motion and distortion correction in their EDDY tool (see section 2.9), and compares measurements to predictions in the native distorted space to avoid interpolation (Andersson et al., 2016). The predictions are based on their Gaussian Process generative model and thus not dependent on a specific dMRI model. If a slice is flagged as an outlier, it can be replaced with the model-free prediction from the GP. TORTOISE employs the MAPPMI model (Özarslan et al., 2013) to predict the diffusion signal for motion and eddy currents distortion correction but does not replace the signal with the predicted values, instead, relies on RESTORE and iRESTORE (Chang et al., 2005; 2012) robust fitting approaches. Koch et al. (2019) derive an outlier score from a harmonic oscillator-based reconstruction and estimation (SHORE) fit of all measurements (Özarslan et al., 2013), and achieve a higher accuracy compared to Gaussian Process-based outlier detection with lower computational demands. Christiaens et al. (2021) integrate slice-wise outlier detection with within-volume motion correction and use their SHARD signal representation to obtain predictions. A probabilistic mixture model per b -value is subsequently used to separate root-mean-squared errors into an "inlier" and outlier class in an unsupervised manner.

Several methods propose to impute detected outliers with signal-predictions (Fig. 8g) (Andersson et al., 2016; Christiaens et al., 2021; Koch et al., 2019), which facilitates the generalizability in that subsequent estimation strategies can be applied as if no outliers were present. A contrasting view is that such an approach does not provide new information (as measurements are predicted from other measurements), and one loses track as to which measurements were 'original' and what the

noise distribution and uncertainty of imputed measurements is. Other approaches therefore propose to propagate a measure of uncertainty through the pipeline and eventually include this as weights in the model estimation (Fig. 8h). Outlier rejection assigns binary weights of 1 (inlier) or 0 (outlier), but weights can take any value between 0 and 1 (Mangin et al., 2002). Sairanen et al. (2018) performs slice-wise outlier detection (SOLID) prior to motion and distortion correction by comparing a slice-wise intensity measure across DWIs with a similar b -value, and computes the modified Z-score as a robust version of the Z-score to assess whether an observation is suspiciously far away from the median. Geometrical transformations are then applied to the modified Z-scores and weights are computed, where a data point gets a weight of 0 if the modified Z-score is above an upper threshold, 1 if below a lower threshold, and a value between 0 and 1 otherwise.

Practical considerations: Outlier detection generally relies on data-redundancy and a minimum number of 'good' measures to separate outliers from inliers. The minimum requirements for accurate outlier detection depend on the separation strategy and the dMRI representation used. Robust estimators typically have a breakdown point, characterizing the proportion of incorrect observations before giving an incorrect result, larger than 0 but lower than 50%: if more than half of the observations are contaminated separation becomes impossible. In low-redundancy datasets not constraining outlier rejection may lead to incorrect estimates (Fig. 8i). The median absolute deviation (MAD), which is often used to estimate the standard deviation of the residuals (Chang et al., 2005; Tax et al., 2015; Zwiers, 2010), has a breakdown point of 50%. For the Gaussian Processes-based outlier detection, FSL recommends a minimum number of directions of 10-15 for a b -value of 1500 and 30-40 directions for a b -value of 5000, whereas simpler outlier measures could work with fewer directions, e.g. in legacy data (Sairanen et al., 2018). In addition, several outlier detection strategies require multiple b -values depending on the model or representation used (e.g. Koch et al. (2019)). Finally, some outlier mitigation techniques require access to additional acquisitions (e.g. reversed PE) or raw k -space data: to ameliorate high-frequency oscillation outliers that can arise from motion in Partial Fourier acquisition, Storey et al. (2007) compare the commonly used reconstruction algorithm causing the oscillations with an adapted reconstruction algorithm and simple zero padding. While the adapted reconstruction algorithm shows significant improvements, it requires access to k -space data. It is thus important to determine data requirements prior to using any outlier detection strategy.

2.11. Susceptibility distortion correction

Description and Importance: As stated in the Introduction, the EPI readout commonly used in dMRI acquisitions is susceptible to B_0 field inhomogeneities. One of the sources of these inhomogeneities is the large magnetic susceptibility differences of the different body parts being imaged. These inhomogeneities introduce geometric distortions and signal pile-ups along the phase-encode direction of the acquisition (Jezzard and Balaban, 1995) and are most significant near the interfaces, such as the air, bone, and soft tissue interfaces for brain imaging (Fig. 9a). Even though the effects of these susceptibility-induced EPI distortions have been reported both on dMRI-derived scalar maps (Kybic et al., 2000; Wu et al., 2008) and on fiber tractography (Irfanoglu et al., 2012), their correction was not a common practice prior to HCP and only a few dMRI processing pipelines included this step.

Approaches prior to and brought by the HCP:

Unlike eddy current-induced distortions, susceptibility distortions affect all dMRI volumes identically in the absence of motion, therefore, the estimated diffusion models remain unaltered pre- and post-correction, which was perhaps the primary reason for their exclusion from most pipelines. However, still, the differences in distortion manifestation in multi-site or longitudinal studies significantly reduced dMRI-derived measure reproducibility (Wu et al., 2008), and the incompatibility of the dMRI-estimated fiber direction with the underlying brain

shape negatively affected the anatomical plausibility of the fiber tracts (Irfanoglu et al., 2012).

The most widely-used susceptibility-induced EPI distortion correction strategies in the pre-HCP era were to acquire additional data to map the B_0 field (Jezzard and Balaban, 1995) or to perform a nonlinear registration of the $b = 0$ image to an undistorted T1 or T2 anatomical image (Kybic et al., 2000; Tao et al., 2009; Wu et al., 2008). These fieldmapping or image registration based correction strategies were designed to correct the gross anatomy of the brain but were incapable of capturing fine-level distortions or redistributing the signal in piled-up or expanded regions. The acquisition strategy employed by HCP involved the use of simultaneous multi-slice approach without any in-plane acceleration, which resulted in severely distorted DWIs. Therefore, HCP employed a different (and more sophisticated) distortion correction strategy, the so-called reversed-phase encoding or blip-up blip-down correction (Andersson et al., 2003; Bowtell et al., 1994; Chang and Fitzpatrick, 1992; Holland et al., 2010; Ruthotto et al., 2012) and popularized this technique by demonstrating its significantly superior performance both in terms of geometric fidelity and signal pile-up redistribution (Fig. 9a-b). The technique relies on having (at least) a pair of PE-opposed $b = 0$ volumes, from which a fieldmap can be estimated and used to correct these distortions. In recent years, the research focus in susceptibility-induced distortion correction has shifted towards the reversed-phase encoding-based correction strategies.

Novel strategies: Several new distortion correction methods that aim to further improve correction performance have been proposed since the release of HCP (Fig. 9b). The DRBUDDI method (Irfanoglu et al., 2015) from the TORTOISE dMRI processing package (Pierpaoli et al., 2010), employs a symmetric diffeomorphic distortion model (Avants et al., 2008) and performs the correction not only using $b = 0$ images but also diffusion tensors fitted to the blip-up and -down acquisitions (if the data supports it). Furthermore, a distortion-free anatomical T2 image serves as a constraint in the presence of large distortions. This multi-parametric and constrained approach enables DRBUDDI to accurately align tiny white matter structures between the blip-up and -down images, which would otherwise be indistinguishable on homogeneous $b = 0$ images. Other correction techniques that aim to further improve upon white matter fiber bundle correction quality have also been proposed and these techniques directly operate on dMRI-derived measures such as fiber orientation distributions (FODs) (Qiao et al., 2019). Another novel method, HySCO (Ruthotto et al., 2013), adopts the physical distortion model from Chang and Fitzpatrick (1992) and minimizes a regularized distance function between the up and down $b = 0$ images to estimate the inhomogeneity. The AnimaBMDistortion correction (Hédouin et al., 2017) method adopts the symmetric block-matching principles to distortion correction.

All these novel techniques compare their results to HCP processing and show either superior or equivalent but faster processing performance. In addition to these image registration-based correction techniques, several deep learning based susceptibility-induced distortion correction techniques have also been proposed in recent years. Schilling et al. (2019a) proposed to employ deep-learning techniques to estimate an undistorted $b = 0$ image from a distorted raw $b = 0$ image and an anatomical T1W image. The estimated undistorted image is provided to FSL's TOPUP with an infinite phase-encoding bandwidth to estimate a deformation field and take advantage of other features of EDDY such as eddy current distortion correction and outlier detection. Qiao and Shi (2020) proposed an unsupervised deep-learning based correction method that uses the fiber orientation distribution information instead of $b = 0$ images to perform the correction. Other examples of deep learning based EPI distortion correction based techniques generally perform machine-learning based image registration and include the works from Hu et al. (2020) and Duong et al. (2020).

In addition to these image registration-based and deep learning-based correction techniques, methods aiming to improve traditional dMRI-to-anatomical registration have also been proposed. Regseg

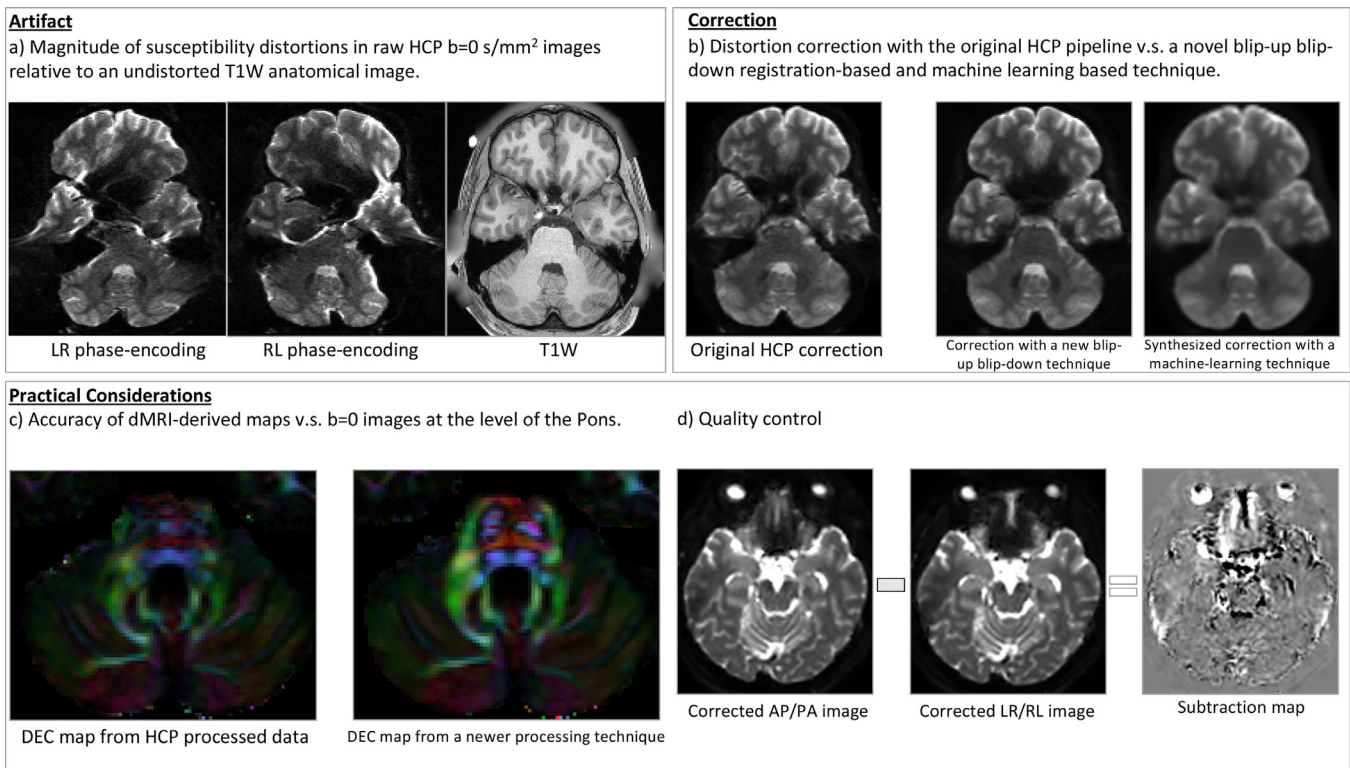


Fig. 9. Susceptibility-induced EPI distortions. **a)** The magnitude of susceptibility-induced distortions of a single subject from the HCP dataset. Distortions near the Pons, frontal lobes and temporal lobes are significant as can be observed from the geometrical difference between the raw, unprocessed $b = 0$ images and the undistorted T1W structural image. The distortions between the Right-Left (RL) phase-encoding and Left-Right (LR) phase-encoding are theoretically opposite of each other. **b)** Corrected $b = 0$ images of the same data using three different methods: The original HCP-processed image made publicly available, a new image registration based technique and a new machine-learning based technique. **c)** The Directionally encoded color (DEC) map (Pajevic and Pierpaoli, 1999) of the same subject at the level of the Pons. The image on the left is computed from HCP-processed data, which relies only on the geometry of the $b = 0$ images and the image on the right is from a method that also uses diffusion information during correction. Using diffusion information improves the anatomical accuracy of the fiber bundles w.r.t just $b = 0$ based correction. **d)** Evaluation of the quality of susceptibility distortion correction with 4-way phase-encoded data. Difference between independently processed AP/PA and RL/LR data using either $b = 0$ or dMRI-derived images can indicate regions with imperfect distortion correction quality, such as the orbito-frontal cortex or posterior part the temporal lobes in these images. The same QC approach could be used to an extent with 2-way blip-up and -down data as well even though the correction of the two images would be inter-dependent.

(Esteban et al., 2016), which is a cortical surface-driven registration method for the segmentation and susceptibility-distortion correction of dMRI is able to achieve high accuracy at a sub-voxel level while registering $b = 0$ to anatomical images. Such cortical surface-based registration techniques could be combined with blip-up -down techniques to possibly further improve correction quality.

In addition to these new correction methods, new acquisition principles that complement the reversed-phase encoding correction strategies have also emerged in recent years. The developing Human Connectome Project (dHCP) opted to employ a neonatal acquisition protocol that not only phase-encoded the data along the Anterior-Posterior (AP) and Posterior-Anterior (PA) directions but also the horizontal Right-Left (RL) and Left-Right (LR) directions (Hutter et al., 2018b). Irfanoglu et al. (2020) showed that these "4-way" acquisitions not only have the potential to provide even more improved distortion correction, but can also significantly improve data reproducibility by reducing the effects of other artifacts such as ghosts.

Most aforementioned correction techniques assume that the underlying susceptibility field is constant throughout the acquisition and, therefore, apply either the same deformation field or the rotated version of the same field (based on motion) to the DWIs. These approaches disregard the dependence of the susceptibility fields on head orientations, hence subject motion. Recently, a new technique that can estimate the susceptibility fields on a per-volume basis has been proposed (Andersson et al., 2018a). This approach updates the estimated fieldmap by taking into

account the effects of subject's motion, which can influence the spatial location and magnitude of the susceptibility-induced distortions by dynamically affecting the field. In cases where a subject moves significantly, i.e., when scanning patients or children, this approach has been shown to further improve anatomical fidelity of the computed dMRI metrics and data reproducibility.

Practical considerations: Most susceptibility distortion correction techniques require additional data, either in the form of a fieldmap acquisition, reverse phase-encoded dMRI data or an undistorted anatomical image. The latter option is already available in most clinical MRI acquisitions, which can directly be used for correction with several publicly available processing pipelines, but may lead to sub-optimal results. The use of reverse phase-encoded data has become quite common in research settings and its popularity is increasing even in clinical environments, for non-brain acquisitions and in vivo and *ex vivo* animal scans, as it only requires the acquisition of at least one $b = 0$ volume with reversed PE orientation.

Theoretical quality control and performance assessment of novel methods are performed with either simulated data (Graham et al., 2016) or with 4-way phase-encoded data (Irfanoglu et al., 2019) (Fig. 9d), which are the approaches used by Gu and Eklund (2019) in their work that compares the performances of publicly available susceptibility distortion correction methods. Quality check for real data is generally still performed visually, by examining the alignment of the corrected $b = 0$ image and an anatomical image, by examining the anatomical accuracy

of dMRI-derived information such as FA maps or FODs or by assessing the residual mismatch between the corrected blip-up and -down images. A critical note is that when only $b = 0$ images are used for the estimation of the fieldmaps, care must be taken that the correction is adequate in regions where the $b = 0$ image has uniform contrast. In such regions, such as the pons, there might not be sufficient local contrast information to drive the correction process, therefore, during QC, the quality of both the corrected $b = 0$ images and the dMRI-derived maps have to be assessed (9c). Additionally, the quality of the $b = 0$ image used for correction can also be crucial, therefore the acquisition of several $b = 0$ images is generally suggested. Another possible remedy for this issue is to use an "estimated" $b = 0$ image, for instance from the tensor or other models, instead of using an acquired image, which is the approach implemented in (Irfanoglu et al., 2015).

2.12. EPI Nyquist ghost correction

Description and Importance: In EPI pulse sequences, an echo is generated for each k -space line and adjacent k -space lines along the phase-encoding direction are traversed in the reverse direction. This reading order causes a low bandwidth along the phase encoding direction and even numbered echoes must be time-reversed to match the odd numbered ones prior to Fourier transformation for image reconstruction. If the forward and backward echoes are not consistent, artifacts are introduced into the images: A delay in the acquisition of an echo will be propagated into all the later ones, resulting in slight timing differences between the peaks of even and odd echoes. For non-EPI acquisitions with one readout direction, this does not cause any problems because each k -space line exhibits identical phase offsets, which is not reflected onto the magnitude images. However, with EPI, the phase inconsistency between adjacent k -space lines results in displaced signal intensity, called Nyquist or $N/2$ ghosts, along the phase-encoding direction, halfway across the image after reconstruction (Fig. 10).

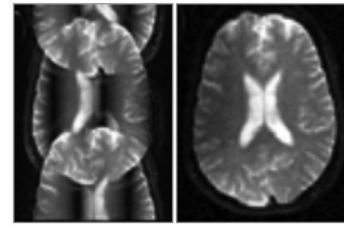
Nyquist ghosts can be caused by several sources including poor shimming, gradient coil heating, patient motion, reconstruction errors, concomitant fields, susceptibility and most predominantly eddy-currents. The manifestation of these ghosts is exacerbated with multi-shot techniques, which introduce an additional source of possible timing inconsistencies. With such techniques and with in-parallel imaging methods, the ghosting pattern is more complex than $N/2$ displacements. When these ghosts overlap with the body organ being imaged, they lead to significantly erroneous diffusion measures (Porter et al., 1999).

Approaches prior to and brought by the HCP: Nyquist ghosts are often corrected by acquiring additional data in the form of three-line navigator echoes, which are used to model the phase differences between adjacent readout lines as a linear phase change (Heid, 2000), or reference scans (Bruder et al., 1992) that are used to calculate the proper phase corrections and filtering. Another school of correction techniques aims at mapping the 2D phase information (Buonocore and Gao, 1997; Chen and Wyrwicz, 2004; Hu and Le, 1996; Xiang and Ye, 2007) through either a modification to the pulse sequence or through separate reconstruction of odd and even echoes.

Among the many ghost correction methods, referenceless methods that use the EPI data for self-correction without any additional calibration or navigator scans are of particular interest as they potentially reduce scan times and are easier to integrate into existing processing pipelines. These methods define a cost function that is minimized when the data is ghost-free. Earlier techniques employed the image entropy as a heuristic cost function (Clare, 2003; Skare et al., 2006) and showed better correction performance than calibration-scan based methods with single-shot EPI but they are unable to reliably remove ghosts in multi-shot or SMS acquisitions. Another category of referenceless methods rely on a more flexible model in which the data samples from each polarity are assumed to be coming from different but correlated images, similar to parallel imaging methods like SENSE or GRAPPA (Chang and Chen, 2016; Hoge and Polimeni, 2016; Xiang and Ye, 2007).

Artifact & Correction

a) Ghost artifact in a single shot acquisition (left) and correction with an entropy minimization technique (right).



Practical Considerations

b) Ghost magnification due to imperfect correction

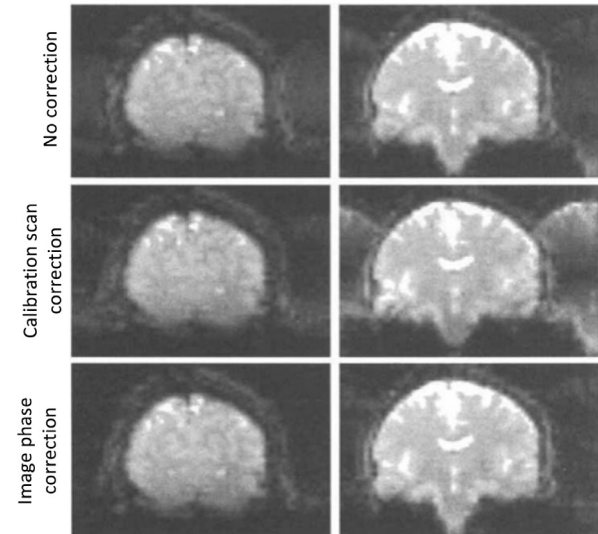


Fig. 10. a) Nyquist ($N/2$) ghosts with varying number of shots and their corrections with a reference-less image entropy-based correction technique. The displayed images are from Skare et al. (2006). b) Displays two similar acquisitions with similar ghost levels (11% of the base image signal). Even though the calibration-based method improved the ghost levels from the first acquisition, it actually magnified the ghost for the second one. The image phase-correction technique did not suffer from this issue. The images are borrowed from (Buonocore and Gao, 1997).

Novel strategies: Entropy based ghost correction has been shown to successfully deghost single-shot EPI images, however, they are inadequate for multi-shot or SMS acquisitions, as these images are confounded by aliasing and the image entropy measure is not applicable. Peterson et al. (2015) proposed an extension to Entropy-based techniques for such cases by maximizing the self-consistency of neighboring k -space points with GRAPPA-like kernels and performing singular value decomposition on individual shot of parallel imaging acquisitions. Recently, structured low-rank matrix methods for ghost correction have received increasing attention for their ability to provide near-excellent ghost-suppression performance (Lee et al., 2016; Liu et al., 2019; Lobos et al., 2018; Lyu et al., 2018; Mani et al., 2017). These approaches assume linear dependencies in k -space due to limited image support, smooth phase variations and multi-channel correlations. Structured low-rank EPI ghost correction methods combine these principles with the fact that EPI data acquired from different polarities can be treated as coming from different effective channels. Since structured low-rank methods for conventional image reconstruction automatically account for the unknown sensitivity maps in a parallel imaging experiment, these approaches apply the same principles to handle the unknown polarity or shot dependent modulations in EPI ghost correction.

The interest in SMS and ultra-high field acquisitions has grown significantly in dMRI research community since HCP, which is reflected in recent publications on EPI ghost correction. Moeller et al. (2015) propose a k -space trajectory correction that is compatible with Slice-GRAPPA for SMS acquisitions, which they apply to 7T dMRI data. Similarly, Hoge et al. (2018) extend their previous method to these acquisitions. Pan et al. (2020) introduces a novel referenceless correction approach and a new reconstruction algorithm for SMS acquisitions without the need of reference scans. Powell et al. (2020) addresses the challenges of ghost correction for high b -value data by denoising the complex channel data to enable robust ghost correction for low SNR images.

Practical considerations: Calibration scan based or navigator based ghost correction techniques require additional data and cannot be applied retrospectively. Several of the aforementioned referenceless methods are performed during image reconstruction or require k -space data, which might not be available in clinical environments. For these reasons, ghost correction techniques are generally not included in widely used dMRI post-processing pipelines. However, a limited number of publicly available modules exist.

Application of the ghost correction techniques to organs other than the brain (e.g. peripheral nerve) is also challenging McKay et al. (2019) due to incomplete fat-suppression and increased B_0 susceptibility, and additional measures might need to be taken for adequate correction.

The quality control of a ghost correction technique is generally performed visually in application studies and compared to previously established methods for publications proposing a novel technique. For diffusion MRI, the 4-way acquisition principles described in Section 2.11 have the potential to provide an alternative quality control approach. Given that the Nyquist ghosts manifest themselves along the phase-encoding direction, dMRI data acquired with different PEs can implicitly reduce the effects of these artifacts (in case they overlap with the brain region) without any correction applied (Irfanoglu et al., 2020). Additionally, a local similarity metric of these different PE data can be used to quantitatively assess residual ghost manifestations if the DWIs are properly corrected for susceptibility-induced distortions.

2.13. Gradient deviations: Gradient nonlinearities & gradient gain miscalibration

Description and Importance: The gradients used for image readout and the encoding of diffusion can deviate from their nominal imposed value due to several factors. Firstly, to limit the peripheral nerve stimulation caused by the rapidly varying magnetic fields as a function of time, gradient coils are often designed to accommodate a modest FOV. This can result in a significant spatial nonuniformity (or nonlinearity) of the effect, which become more pronounced when moving away from the isocenter. Particularly in high-performance gradients such as whole-body or head-only ultra-strong gradient systems, gradient linearity is often sacrificed (Foo et al., 2020; Jones et al., 2018; Setsompop et al., 2013; Weiger et al., 2018), but also data from more conventional clinical systems can be affected. Mesri et al. (2020) report angular- and magnitude deviations of the gradients for HCP subjects of up to 5° and 10% respectively, and further characterize their mean magnitude deviation and fractional gradient anisotropy.

The gradient along an axis is generated by providing current to the corresponding gradient amplifier, which in turn generates magnetism along orthogonal directions. In order for the hardware to produce the desired gradient strength at the magnet isocenter given an input current, the gains of the x , y , z gradient amplifiers have to be calibrated. This calibration process is usually performed by vendors at installation and during routine service, using anatomical scans of a phantom of known dimensions. Nevertheless, residual gradient miscalibrations that are geometrically undetectable could still be present.

Deviations from the expected gradients cause geometric image deformations and discrepancies from the intended diffusion encoding. Ge-

ometric distortions and associated signal intensity deviations occur because typical image reconstruction methods assume the data was spatially encoded using calibrated linear gradients. Even on clinical scanners these distortions were found to be significant (Wang et al. (2004) report distortions between 10 and 25 mm), and this can thus be problematic in surgical planning or volumetric studies.

B-matrix discrepancies resulting from gradient deviations are spatially varying, i.e. each voxel has a unique B-matrix (or set of b -values and gradient directions). Not accounting for this can lead to significant biases, as was shown in the case of gradient nonlinearities for the estimated diffusion coefficient (up to 30% even on 1.5T 40 mT/m (Bammer et al., 2003)), diffusion tensor directions and diffusion/kurtosis tensor scalar measures (up to 10% and 3% respectively (Mesri et al., 2020)), fibre orientation distribution functions and derived fibre directions (several degrees, (Guo et al., 2020; Morez et al., 2021)), tissue signal fractions (up to 34% for WM (Morez et al., 2021)), tractography and connectivity analysis (Guo et al., 2019; Mesri et al., 2020; Morez et al., 2021), group statistics (changes in significance and effect sizes (Mesri et al., 2020)), and measures derived from sequences beyond Stejskal-Tanner encoding (Paquette et al., 2020). In addition, B-matrix deviations can increase the variability between scanners (Hansen et al., 2021; Tax et al., 2019a). In contrast to the perhaps common assumption that deviations in the B-matrix mostly affect measurements with a high diffusion weighting, also lower-to-moderate diffusion-weighted signals are affected as the absolute signal change as a function of b -value is larger in this regime (Guo et al., 2020).

Approaches prior to and brought by the HCP: To correct for the effects of gradient deviations, accurate characterization is crucial, i.e. mapping the spatial dependence at each location \mathbf{r} of the effective magnetic field generated by each coil $B_{z,\text{eff},i}(\mathbf{r})$, $i = x, y, z$ compared to the nominal imposed field $B_{z,i}(\mathbf{r}) = g_i r_i$ where g_i is the applied nominal gradient. $B_{z,i}(\mathbf{r})$ is often expressed by a spherical harmonic expansion, and can be provided by the manufacturer (for gradient nonlinearities), or characterized by imaging a phantom (for a joint characterization of deviations) with known dimensions (Glover and Pelc, 1983; Langlois et al., 1999) or with known diffusion properties (Hansen et al., 2021; Lee et al., 2020; Mohammadi et al., 2012b). By computing the partial derivatives of $B_{z,\text{eff},i}$ normalized by the respective g_i , one can obtain the gradient coil tensor $\mathbf{L}(\mathbf{r})$ characterizing deviations up to the first order (Bammer et al., 2003; Mohammadi et al., 2012b).

Geometric distortions arising from gradient nonlinearities can be corrected online on the scanner (Glover and Pelc, 1983; Langlois et al., 1999), but care must be taken as sometimes only the distortions in-plane are remedied (Wang et al., 2004) and distortion correction is not always applied to all types of images (e.g. T1 but not dMRI for some vendors). Alternatively, if uncorrected images can be exported, the geometric distortion can be performed offline as part of the dMRI preprocessing pipeline (Fan et al., 2016; Glasser et al., 2013; Rudrapatna et al., 2021). It should be noted that most widely available online and offline distortion correction techniques perform image-based correction, that is, inverse Fourier transformation of the dataset followed by coordinate mapping and interpolation, and signal intensity correction with Jacobian determinants (see Section 2.9). However, the interpolation leads to blurring and resolution loss, and distortions from gradient deviations are ideally corrected prospectively during reconstruction (Tao et al., 2015).

Based on the coil tensor, the effective gradient and b-matrix can be computed as $\mathbf{g}_{\text{eff}}(\mathbf{r}) = \mathbf{L}(\mathbf{r})\mathbf{g}$ and $\mathbf{b}_{\text{eff}}(\mathbf{r}) = \mathbf{L}(\mathbf{r})\mathbf{bL}(\mathbf{r})^T$, respectively (Bammer et al., 2003). While the signal could theoretically be 'corrected' by interpolating it back to the nominal B-matrix using a dMRI signal model (e.g. for approaches that rely on a shell-sampling), the spatially varying gradients and B-matrix are more commonly dealt with during or after the estimation of a dMRI model or representation. Malyarenko et al. (2014) proposes an approach to correct the estimated ADC for conventional (three orthogonal direction) DWI acquisitions. Bammer et al. (2003) derive corrections for the diffusion tensor based on the full coil tensor and effective B-matrix, while

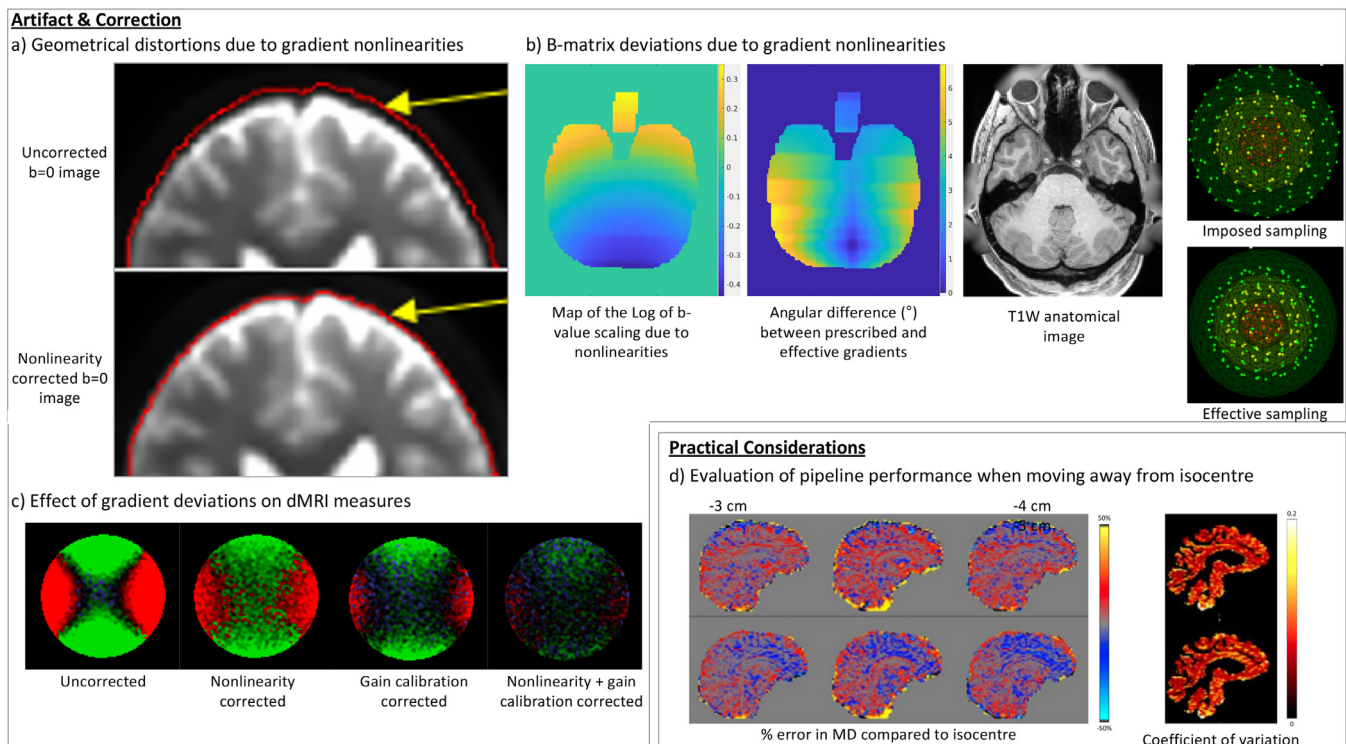


Fig. 11. Gradient deviations. **a)** Geometrical distortions due to gradient nonlinearities in an HCP dataset. The red outline is obtained from a corresponding T1W image and pasted on to the two $b=0$ images. **b)** B-matrix deviations due to gradient nonlinearities in an HCP dataset. From left to right: the logarithm of the determinant of the coil tensor L , which provides information about the voxel-wise scaling of the b -values (with positive values indicating an increase in the effective b -values and the negative values a decrease relative to the prescribed value), the total rotation (as sum of the absolute values of Euler angles) in degrees induced by the rotation component of L , the corresponding T1W anatomical image showcasing the location of the slice, and an example of the imposed and effective sampling in a voxel with coil tensor $\Delta L = \text{diag}([-0.13, -0.14, -0.05])$ (Figure adapted from Guo et al. (2020)). **c)** Direction-encoded color map (first DT eigenvector modulated by FA with maximum brightness indicating FA = 0.05) of an isotropic phantom. Ideally FA should be zero for an infinite SNR and have no directional bias. The improvements is shown of each correction step. **d)** Left: Comparison of MD when moving the table away from isocenter to MD at isocenter for the pipelines proposed in Fan et al. (2016) (top) and Glasser et al. (2013) (bottom). Right: coefficient of variation of MD calculated over different bed translations. Figure adapted from Rudrapatna et al. (2021).

Lee et al. (2020) propose a simplified approach based on corrected b -values only. Guo et al. (2019); Morez et al. (2021) propose correction strategies for spherical deconvolution approaches - which commonly rely on shell-sampling - by adjusting the response function during estimation.

Novel strategies: B-matrix deviations are typically computed as one of the later stages of the preprocessing pipeline, i.e. after subject motion/eddy current corrections. However, if the subject has moved, the $L(r)$ of the original position in the scanner should be applied. Hence, the B-matrix not only varies spatially but also temporally. Rudrapatna et al. (2021) compute spatiotemporal B-matrices by using the estimated motion parameters to map the temporal evolution of the effective gradient amplitudes for each voxel location. Their results suggest that the spatiotemporal B-matrix approach could yield more consistent parameter estimates in the case of high gradient nonlinearities and/or severe motion.

The nonlinearity of a gradient system depends on the coil design and wiring, therefore are known to the manufacturers in advance, however, the gain settings need to be estimated and calibrated periodically. This calibration process is based on the known shape of a phantom, which has a linear dependence on gradient strength. Diffusion synthesis, on the other hand, has a quadratic dependence, and therefore is more sensitive to any miscalibrations: Teh et al. (2017) recently showed that their proposed gradient gain and nonlinearity estimation method improves accuracy of both anatomical and diffusion MRI.

Practical considerations: It is not always straightforward to appropriately correct for gradient nonlinearities if the gradient deviations are

unknown to the user. Scanner manufacturers in principle possess the necessary information for correction, but since the specification of a gradient system is commercially sensitive information this is often not widely available (Doran et al., 2005). In addition, each gradient coil may be slightly different due to e.g. winding errors, which causes variations from the predicted field (Janke et al., 2004). Accurate characterisation of the gradient system is therefore ideally performed in-house, but the resources and knowledge to do so are not always available. Public databases such as the HCP (Sotiropoulos et al., 2013b) and others (Tax et al., 2019a) increasingly provide information to consider the effective B-matrix in analyses. Care should be taken, however, regarding the gradient information provided and/or used for correction: the coil tensor typically has non-zero cross-terms and is not symmetric, but some studies assume otherwise as highlighted by Bammer et al. (2003).

Commonly available and standardized open source approaches for integrated image-distortion correction (e.g. jointly with motion, eddy, and susceptibility correction) are still not publicly available. Rudrapatna et al. (2021) compare two pipelines proposed by the HCP that address these steps separately: Glasser et al. (2013) advise motion, eddy, and susceptibility correction prior to gradient nonlinearity correction, whereas Fan et al. (2016) suggest the opposite order. By scanning subjects at isocenter as well as deliberately translating the bed away from isocenter, they assess the robustness of pipelines by assessing the change and coefficient of variation in DT estimates of the bed-translated datasets to the isocenter-dataset (Fig. 11d). They found that determining the best performing pipeline was not straightforward as performance seemed to depend on the amount of gradient nonlinearity and/or mo-

tion present in the data, and on the DT measure being evaluated. In addition to ignoring interactions between sources of distortions, separate correction leads to additional interpolation unless the transformations can be concatenated, hence reducing the image resolution by additional blurring.

2.14. B_1 Bias field correction

Description and Importance: MR signal intensity measured from homogeneous tissue varies typically smoothly across an image. Such slow, non-anatomical intensity variation is usually attributed to poor radio frequency (RF) coil uniformity. This B_1 inhomogeneity, causing a variability in flip angle of 15% in the human brain at 3T and even more at higher field strengths due to shorter RF wavelength, is an intrinsic problem that even a perfect coil cannot resolve (Moeller et al., 2020). The intensity variations are typically modeled as a smooth multiplicative bias field. The common practice of normalizing a diffusion weighted image with the corresponding non-diffusion-weighted $b = 0$ image thus cancels this bias field in case of minimal subject motion. Therefore, this artifact gained less attention in diffusion MRI in comparison to other MRI modalities. However, when $b = 0$ normalization is not preferred or possible, this artifact can be corrected prior to further analysis. Specifically, not all diffusion MRI analysis are compatible with a normalization by the $b = 0$ image; e.g. TE-dependent DWI or estimation of fiber ODFs on a b -shell. Therefore, other B_1 bias field correction strategies might be relevant; the bias field is then estimated based on the (averaged) $b = 0$ -image and DWIs are scaled by the estimated field thereafter.

Approaches prior to and brought by the HCP: Sled and Pike (2000) introduced a widely used automatic and non-parametric method for the estimation and correction of the B_1 bias field. During an iterative process, the smoothly varying bias field is estimated by maximizing the high frequency content of the histogram of signal intensities in the image. The original algorithm has been modified by including a B -spline basis approximation to parameterize the bias field and adopting a hierarchical optimization algorithm (Tustison et al., 2010). An alternative strategy to estimate the bias field using an adaptive low-pass filtering technique is implemented in FSL, where the bias field is estimated using an Maximum a posteriori estimator with a Random Field (MRF) based spatial prior (Zhang et al., 2001).

Practical considerations: Although B_1 bias field correction is not widely adopted in dMRI analysis, its application might be encouraged in case of strong head motion and high magnetic field strengths. Various software packages and pipelines have included this bias field correction as an optional step in the image preprocessing pipeline, e.g. MRtrix (Tournier et al., 2019), FSL (Jenkinson et al., 2012), QSIprep (Cieslak et al., 2020), Tractoflow (Theaud et al., 2020), PreQual (Cai et al., 2021b), and DESIGNER (Ades-Aron et al., 2018). However, when applied, the signal scaling will be another source of noise heteroscedasticity in the data (similar to Fig. 3c) that might have to be accounted for in parameter estimation, especially with robust estimation techniques (Section 2.10), in subsequent steps for optimal precision.

2.15. Spatial normalization

Description and Importance: Manual delineation of structures in MR images enables quantification of local effects and serves as one of the basis of population based neuroimaging studies. However, this process is very time consuming for large population sizes and is prone to inter-operative variability. Spatial normalization techniques provide a fast alternative and have been used successfully for automated labeling of anatomical MR images. dMRI provides information of typically higher dimensionality about the tissue than conventional MRI, which raises the need for specialized image registration techniques to fully take advantage of this modality.

Approaches prior to and brought by the HCP: Since the early 2000s, Tract-Based-Spatial Statistics (TBSS) (Smith et al., 2006) – which non-

linearly registers subject data to a common space and performs a skeletonization step – has been de-facto analysis strategy for dMRI data. The main advantage of TBSS was its ability to compensate for the misalignments among subjects in a population, originating from imperfect image registration. In these early days, registration of dMRI data has mostly been based on FA images (Mohammadi et al., 2009; Smith et al., 2006), which did not fully utilize the rich set of information provided by the diffusion tensor or higher order models. More recent advances in specialized dMRI registration and template creation techniques enabled more robust voxel-wise analysis of dMRI data, which provided an alternate route to TBSS.

The Diffusion Tensor Imaging ToolKit (DTI-TK) method from Zhang et al. (2006) was one of the first widely used approaches to dMRI registration specifically. DTI-TK employed the differences between the deviatoric part of diffusion tensors as its similarity metric, which not only considered the anisotropy information but also the estimated principal diffusion direction. Combined with a nonlinear locally-affine deformation model, DTI-TK was able to provide near-excellent voxel-wise correspondence in single fiber white-matter regions.

Novel strategies: The DR-TAMAS methodology (Irfanoglu et al., 2016) extends the feature set of DTI-TK, including diffusivity similarity in its cost function with a locally varying weighting, which favors the tensor-deviatoric similarity in white matter regions and the tensor-trace similarity in gray matter and CSF-filled regions. This strategy, along with its support to use anatomical MR images, enables DR-TAMAS to achieve a high quality alignment in all brain regions, not only the white matter. However, DR-TAMAS employs the DT for registration, which might be inadequate for regions of complex fiber-configurations. To achieve better image registration performance in such regions, Raffelt et al. (2011) proposed to employ FOD function similarities. With a multi-level registration strategy that not only gradually increases image resolution but also FOD spherical harmonics degrees, this method is able to achieve a high quality of alignment in all white matter regions. To achieve a better registration accuracy, both these methods use the popular Symmetric Normalization (SyN) transformation model, a powerful diffeomorphic transformation that is not affected by the switching of the source and target images that can intrinsically solve the “2-mean” problem (Avants et al., 2008).

Along with their high quality registration performance and the advances in susceptibility distortion correction strategies, which provide a high level of morphological correspondence between dMRI and anatomical images, these dMRI registration methods have opened the door for voxel-based morphological analysis. The Jacobian matrices originating from the tensor-based registration techniques have been extensively used to analyze different pathologies and those originating from FOD based registration led to analysis approaches for fiber bundle morphology with fiber bundle elements (FIXEL) (Raffelt et al., 2017).

3. Quality control in preprocessing

QC is a crucial but very often neglected aspect of dMRI data preprocessing as it can be time-consuming and nontrivial. Nonetheless, detecting data quality issues and assessing the efficacy of the preprocessing pipeline is of tremendous importance to avoid biased model-based parameters or structural connectivity estimates (Tournier et al., 2011). Here, we will discuss efforts to evaluate the quality of 1) the acquired data, and 2) preprocessing pipelines themselves, where the latter implies that appropriate evaluation criteria (e.g. a ground truth) is available.

3.1. Quality control of data

3.1.1. Data quality measures

“Data quality” pertains both to the quality of the metadata and file format (e.g. appropriate storage of acquisition parameters), and the unprocessed and processed imaging data. Regarding the imaging data,

the lack of a ground truth when dealing with biological tissues implies that data quality can only be assessed by surrogate measures derived from the data itself. Such quality measures have been proposed for MRI images in general (e.g. signal-to-noise ratio (SNR), see also [Esteban et al. \(2017\)](#) for a summary), and several measures more specific to dMRI have been discussed in the "Practical considerations" sections. For example, individual motion and distortion-related QC metrics can provide very useful information to the experimenter, pointing them to individual volumes which may benefit from further visual inspection because, e.g., they are affected by a significant amount of motion. However, such measures do not necessarily quantify the overall quality of a dMRI dataset. The SNR obtained from the $b = 0$ s/mm² volumes is a very important measure, but for dMRI this quantity does not provide any information about for example the angular contrast of a given dataset. Maximising such contrast is crucial to, e.g., be able to resolve complex sub-voxel fibre geometries. Recently, a b -shell-specific contrast-to-noise (CNR) measure was introduced ([Bastiani et al., 2019b](#)). Notably, this model-free ([Andersson and Sotiropoulos, 2015](#)) metric has been shown to quantify the amount of angular contrast available in a given dMRI dataset, with higher CNR leading to an improvement in the estimation of complex fibre configurations (i.e., more than one fibre compartment in each voxel).

Most QC metrics are based on parameters used to correct the same dataset they are extracted from. This means that they do not necessarily reflect the performance of the preprocessing tool, as it is likely the case that the data has been preprocessed correctly despite, e.g., a subject moving significantly more than the others. Summary QC metrics such as the SNR and CNR play a crucial role in quantifying the overall quality of a dataset. In cases where a preprocessing step has failed, the individual QC metrics may mislead the researcher in believing for example that a given subject did not move significantly during data acquisition. However, SNR and CNR metrics would become strong outliers, warning the researcher that the dataset requires further visual inspection.

Standardization and generalizability of QC metrics is necessary to harmonize datasets and assess new acquisition protocols, but it is not straightforward ([Liu et al., 2015](#)). Several quality metrics might depend on specific scanning parameters, such as voxel volume, readout bandwidth and imaged volume's size ([Sotiropoulos et al., 2013a](#)). These factors need to be accounted for when, e.g., comparing subjects between studies to assess the performance of their newly developed dMRI data acquisition strategy ([Bastiani et al., 2019b](#)). Some studies have tested different measures in big cohorts and between sites ([Kochunov et al., 2018](#); [Lauzon et al., 2013](#); [Roalf et al., 2016](#)), but the accuracy of such measures across different studies using different data acquisition protocols has yet to be assessed.

3.1.2. Automatic data quality control

[Section 2](#) provides some guidelines for quality control of data upon individual preprocessing steps; this section will focus on tools for overall quality control of single subject datasets and population-based studies. There are two ways to assess the overall quality of the preprocessed data prior to any microstructural model fit. The first solely relies on visual inspection of the imaging data, and can be performed at any stage of the preprocessing pipeline. A volume can be considered unusable, either a priori because of, e.g., too much within-volume motion occurred, or a posteriori, looking at the output of each preprocessing stage and deciding whether the preprocessing routine achieved a "good-enough" result. All these considerations are subjective and depend on the judgment and expertise of the visual inspector. Moreover, the different artifacts present in a typical SE-EPI dMRI experiment may cause very subtle image distortions or contrast modulation. These may be particularly challenging to consistently identify by visual inspection of a 4-dimensional (where all b -values and gradient directions are stored along the 4th dimension) dMRI dataset. With the recent advent of large population-scale studies ([Alfaro-Almagro et al., 2018](#)), visual QC of dMRI datasets becomes impossible.

The second way to perform QC of dMRI data is to automatically extract and rank QC measures, such as those presented in the previous sections of this review. These can provide very useful extra features to, e.g., de-confound statistical associations between imaging and non-imaging data ([Alfaro-Almagro et al., 2021](#)). This has fortunately gained more attention in the literature recently, and several automated tools have been developed. Some frameworks rely on phantom data to perform pre-calibration based on the accuracy of the expected DTI-derived parameters ([Hasan, 2007](#)). Others combine various dMRI data processing tools to extract useful QC measures and perform automated QC. [Lauzon et al. \(2013\)](#) propose a framework integrating FSL and CAMINO that segments $b = 0$ images for regional quality checking, and reports motion parameters, outliers, voxel-wise and slice-wise goodness of fit measures with images of 'best' and 'worst' slices, estimates of FA variance and bias, power curves for different effect sizes, and images for B-matrix checking. They output quality reports for both the raw and processed data. DTIPrep checks dMRI data for information correctness (e.g. image dimensions, origin, voxel spacing, and orientation), slice-wise outliers, residual motion after correction, and suspicious entropy of fiber-orientation estimates across the brain (see also [Section 2.10](#)) ([Liu et al., 2010](#); [Oguz et al., 2014](#)). [Roalf et al. \(2016\)](#) provide a set of scripts based on AFNI and FSL to classify a dataset as being of excellent, good, or poor quality based on the number of intensity-based outliers, relative motion, and temporal SNR; and [Maximov et al. \(2019\)](#) calculate the latter for each b -value as a quality measure of different pipeline steps. In addition, a fully automated dMRI QC framework based on the FSL EDDY tool ([Andersson and Sotiropoulos, 2016](#)) has been developed ([Bastiani et al., 2019b](#)). This framework consists of two tools, i.e., QUAD (QUality Assessment for DMRI) and SQUAD (Study-wise QUality Assessment for DMRI), which automatically generate quantitative single subject and study-wise reports, respectively. The reports offer a rich description of the off-resonance and subject movement effects present in the uncorrected data by extracting several QC metrics. These are based on the parameters estimated by EDDY when correcting for between-volume motion and off-resonance fields ([Andersson and Sotiropoulos, 2016](#)), signal dropout caused by movement during the diffusion encoding ([Andersson et al., 2016](#)), within-volume movement ([Andersson et al., 2017](#)) and movement-induced changes of the susceptibility-induced off-resonance field ([Andersson et al., 2018b](#)). PreQual ([Cai et al., 2021b](#)) is built around FSL, MRTrix, and ANTs and performs QC on the raw and preprocessed data. This tool allows for checking the correctness of the phase encoding direction, and provides qualitative and quantitative QC reports on denoising (SNR across $b = 0$ images), intensity normalization between input datasets (scale factors and plot of the average $b = 0$ intensity histograms), susceptibility distortion correction (side-by-side visualization of $b = 0$ and T1 image), FSL's EDDY output, DT fitting (visualization of tensor glyphs, FA, and MD, and quantification of FA per region and goodness-of-fit), B-matrix flips, brain extraction (contours of the outline on a $b = 0$ image), Gibbs ringing (averaged differences upon correction across $b = 0$ images), Rician bias correction (decreased shell-wise intensity distributions after correction), and B_1 bias field correction (visualization of $b = 0$ images before and after correction).

Finally, several QC tools have been proposed based on machine learning. QC-Automator is a deep-learning based automated QC tool trained on a large manually labeled dataset of artifactual and artifact-free slices from different sites and scanners ([Samani et al., 2020](#)). Specifically, QC-Automator consists of a pre-trained CNN that has learned generic image-features adapted to the task of slice-artifact detection using transfer learning. It can detect artifacts on axial slices (e.g. chemical shift, susceptibility, ghosting) and sagittal slices (e.g. motion and multiband interleaving artifacts). [Graham et al. \(2018\)](#) investigate the training of a deep-learning based QC tool on simulated data and a small amount of manually labelled data to minimize manual labor, and show that its performance can approach that of a network trained on real data.

3.2. Evaluation of preprocessing pipelines

The recent literature has seen an increase of strategies to compare preprocessing pipelines, aiming to allow end-users to make a better-informed choice among the breadth of tools available. Quantitatively evaluating preprocessing pipelines requires the availability of a ground truth, most commonly in the form of numerical or physical phantoms. Several numerical simulation frameworks exist, which typically simulate 1) the diffusion process to obtain representative dMRI contrasts, and 2) the MR acquisition process to mimic the occurrence of artifacts. The former can for example be achieved by a model- or representation-based approach (e.g. forward generating the signal given a ground truth DT and acquisition scheme) whether or not combined with a numerical fibre phantom (Neher et al., 2014; Perrone et al., 2016), or by simulating random walks in an arbitrary substrate. Simulation of the diffusion process is sufficient to assess the performance of correction procedures affecting the local signal or B-matrix such as voxel-wise outlier detection (Chang et al., 2005; Farzinfar et al., 2013a; Tax et al., 2015) and B-matrix rotation (Leemans et al., 2009). The MR image acquisition- and artifact simulation can either be performed in image-space or in k -space, where the latter allows for a more natural integration of artifacts associated with image formation. The POSSUM framework (Graham et al., 2016) simulates realistic dMRI datasets using a model-free representation of diffusion and a physics-based approach to the MR image acquisition process in k -space, allowing for the characterization of a wide range of artifacts including those that affect the geometry (e.g. eddy currents, motion (Graham et al., 2016), susceptibility fields (Graham et al., 2017)), and the signal (blurring due to motion and eddy current decay, dropout due to motion, Nyquist ghosting, chemical shifts, Gibbs ringing). It outputs the ground truth signals and deformation fields for evaluation. This approach has been used to evaluate individual processing steps as well as overall pipelines and automatic data QC procedures (Gu and Eklund, 2019; Haddad et al., 2019). Ades-Aron et al. (2018) evaluate the accuracy of their Diffusion parameter Estimation with Gibbs and Noise removal pipeline (DESIGNER) on a numerical phantom created in image-space by averaging spherical harmonics from 36 HCP datasets nonlinearly registered to a common space, for varying noise levels and in presence of Gibbs artifacts. They found that including noise removal and Gibbs ringing correction yielded increased accuracy of dMRI measures.

Finally, the careful design of public imaging databases can also provide ground truth surrogates for evaluation. The Multiple Acquisitions for Standardization of Structural Imaging Validation and Evaluation (MASSIVE) database consists of 8000 dMRI volumes distributed over five shells with b -values up to 4000 s/mm^2 and two Cartesian grids with b -values up to 9000 s/mm^2 , B_0 field maps, noise maps, and three-dimensional FLAIR, T1 -, and T2 -weighted scans (Froeling et al., 2017). Different PE directions are available, and the database can serve as a testbed for preprocessing pipelines. Irfanoglu et al. (2019) proposed a database and the corresponding methodology for quantitative assessment of newly proposed eddy current and susceptibility-induced distortion correction techniques. The dMRI data of this database contains two shells acquired with 4-way phase-encoding with diffusion gradients sampling the whole-sphere.

Test-retest databases on the same scanner or across scanners are useful to compare the reproducibility of pipelines. Ades-Aron et al. (2018) assess the precision of pipelines by computing the coefficient of variation in a test-retest database of 30 subjects scanned three times. Publicly available examples include the Penthera1.5T and Penthera3T of 10 subjects scanned four times (twice with ten minutes delay and twice with two days delay) at 1.5T (Chamberland et al., 2019; Girard et al., 2015), and 13 subjects scanned six times in two sessions with three scans per session at 3T (Paquette et al., 2019), respectively. The HCP provides test-retest data on 46 subjects (<https://www.humanconnectome.org/study/hcp-young-adult/document/1200-subjects-data-release>). The MASIVAR database

consists of 319 dMRI datasets of 97 subjects on 4 scanners, to assess variability on different levels (Cai et al., 2020). Finally, the CDMRI Harmonization database provides data of 15 subjects on 3 different scanners with 5 different protocols in total, to assess cross-scanner and cross-protocol variability (Ning et al., 2020; Tax et al., 2019a).

Several studies acquired independent measurements alongside dMRI data to characterize confounds, e.g. motion navigators (Taylor et al., 2016) or cardiac/respiratory cycle measurements (Mohammadi et al., 2013), which could be used to benchmark preprocessing pipelines. Other studies use surrogate measures derived from the data to evaluate performance; however, in absence of a ground truth, the underlying assumptions indicating ‘good performance’ may not always be valid and results have to be interpreted with caution. Brun et al. (2019) compute the maximum mutual information (MMI) between dMRI and T1 images to assess the performance of distortion correction, and the DT-fitting error, mean dispersion index of the DT first eigenvectors in a neighborhood, and spatial variance of reconstructed fascicles (i.e. the covariance matrix of the voxel-coordinates that the fascicle traverses within a certain distance from the seed) to evaluate the overall performance of preprocessing. As measures of pipeline performance they assume that a higher MMI and lower dispersion index, fitting-error, and tract spatial dispersion indicates better pipeline performance, and identify a pipeline leveraging full reversed PE data as the best one out of six. Maximov et al. (2019) detect significant spatially varying differences between pipelines using TBSS, and compare temporal SNR and dMRI sensitivity to age between different pipelines. Vellmer et al. (2018) assess the performance of different preprocessing pipelines by their accuracy in brain glioma differentiation. Other surrogate measures of pipeline-performance used in the literature include increased tract length (Zhuang et al., 2013), increased FA (Yamada et al., 2014), and image smoothness and neighboring DWI correlation (Cieslak et al., 2020).

4. Availability of tools

With global movements promoting open-source code and data sharing, our field too has seen a growth in the public availability of dMRI preprocessing tools. Such software packages typically provide the option to perform multiple preprocessing steps successively, and often include the possibility to perform other steps of the dMRI pipeline such as model fitting and tractography. Many preprocessing tools developed not as part of a particular dMRI software package are available on open-source repositories such as GitHub or the MATLAB repository. In addition to software toolkits providing integrated preprocessing pipelines, dedicated pipelines can also be created with pipeline-frameworks that wrap around separate functions or dependencies of different preprocessing packages. This can be in the form of Bash, Python, or MATLAB scripts, as for example adopted in the DESIGNER pipeline (Ades-Aron et al., 2018), PreQual (Cai et al., 2021b), and MRtrix3_connectome (https://github.com/BIDS-ApPs/MRtrix3_connectome). Whereas scripts are relatively easy to create, they may be hard to maintain and do not straightforwardly allow to resume processing in case of interruptions. Theaud et al. (2020) discuss multiple pipeline-tools including Luigi, Snakemake (Koster and Rahmann, 2012), and Nipype (Gorgolewski et al., 2011), where the latter is a dedicated neuroimaging data processing framework in Python. QSIprep (Cieslak et al., 2020) and dMRIprep (<https://github.com/nipreps/dmriprep>) are based on Nipype. Theaud et al. (2020) mention the complexity of adding and maintaining packages in Nipype as a challenge for creating dMRI preprocessing pipelines, and instead opt for Nextflow (DI Tommaso et al., 2017). Based on this framework, they propose the TractoFlow pipeline that can be run inside container software such as Singularity (Kurtzer et al., 2017), which fixes the versions of dependencies and as such improves reproducibility of the pipeline. Other frameworks have also been made available as containerized version, such as PreQual (Cai et al., 2021b), QSIprep (Cieslak et al., 2020), MRtrix3_connectome (https://github.com/BIDS-ApPs/MRtrix3_

connectome), dMRIPrep (<https://github.com/nipreps/dmriprep>), and QuNex (<https://bitbucket.org/oriadev/qunex/wiki/Home>).

Finally, cloud-based pipelines or platforms have been developed such as Flywheel (Wandell et al., 2015), O8T (Yeung et al., 2021), BrainLife (Avesani et al., 2019), QuNex and QMENTA. These platforms allow to run multiple tools under a common interface in the cloud. Some of these are commercial products and others publicly available or provided with separate academic/industrial licensing. Cloud-based approaches allow to either use data onsite or upload them to the cloud using web interfaces. The focus of these approaches is to provide automated and reproducible end-to-end solutions.

5. What's next in dMRI preprocessing

Despite the ever increasing availability of tools for dMRI preprocessing, running a preprocessing pipeline can be tedious and challenging even for technical experts. First and foremost, there is to date no consensus on the optimal pipeline; considering the possibility of combining individual modules from different software packages, varying the order of steps, and the many user-dependent variables, a very large number of preprocessing options are available to the users, often with unknown outcome in accuracy, precision, and/or robustness on the final visual or statistical analysis. A consensus could on the one hand greatly simplify dMRI preprocessing for users who may not necessarily have in depth knowledge of dMRI data analysis techniques, and boost reproducibility of findings across studies which, in the era of big multi-centre imaging studies, is an issue that is gaining a lot of attention (Lerma-Usabiaga et al., 2020; Prohl et al., 2019). This arguably may become even more important as the pipeline from acquisition to modelling becomes more integrated leading to progressively more complex analysis workflows beyond a single expertise (Esteban et al., 2018). On the other hand, apart from several practical considerations including those described in this review, the 'optimal' choice of pipeline and its performance may highly depend on the data, and become quickly outdated with new tools becoming available. Furthermore, it is important to maintain a close connection with the data and understanding of the practical considerations and limitations of different dMRI preprocessing steps, and hence providing 'black-box' pipelines may be undesirable. Indeed, ongoing consensus efforts involving a large part of the community should greatly contribute to these discussions and reaching a consensus, as in other fields (e.g. Choi and Kreis (2021)).

Here, we discuss several aspects and developments that deserve attention in the discussion of what's next in dMRI preprocessing. First, the lack of data standardization and the fixed order and inclusion of preprocessing steps in available software platforms challenges the flexible construction and exploration of pipelines. Next, we discuss the need for integration of acquisition and preprocessing and extension to preprocessing of data beyond conventional adult in vivo human brain PGSE EPI data. Finally, we highlight potential advances that machine learning can bring in dMRI preprocessing.

5.1. Data standardization and open-source flexible pipelines as the new norm

Data from different scanners, vendors, or software versions on the same scanner can be stored differently in the DICOM format. This poses a huge challenge for data preprocessing, as the pipeline may have to be re-adjusted for each new dataset. An increasing number of software packages provide (semi-)automatic checks for correctness of information, e.g. B-matrix flips (Section 2.2 and Fig. 2). Most current dMRI preprocessing tools work with other file formats than DICOM, e.g. Nearly Raw Raster Data (NRRD, https://www.naminc.org/wiki/NAMIC_Wiki:DTI:Nrrd_format) or the Neuroimaging Informatics Technology Initiative (NifTI, <https://nifti.nimh.nih.gov/>) file formats, of which the latter is the most commonly used. NifTI was adapted from the widely used ANALYZE 7.5 file format (Cox et al.,

2004) and several DICOM to NifTI conversion tools and guidelines are available (Li et al., 2016). One of the main objectives was to provide a community-based framework to address the lack of interoperability of tools and data, and as such make them more useful. While initially focused on fMRI, NifTI standards have also been proposed for storing dMRI data. NifTI files are commonly accompanied by a .bval and .bvec file describing the diffusion weighting and direction, respectively. Patel et al. (2010) furthermore proposed standards for storage of metadata in NifTI for DWI (MiND). Nevertheless, such standards do not always provide the necessary flexibility or have not yet found widespread adoption; whereas the extended MiND header for example proposes to reserve the 4th NifTI dimension for time-data and the 5th dimension for vector-valued data such as dMRI measurements in different directions, most tools still expect this information to be stored in the 4th dimension. Furthermore, the field has evolved with multidimensional data including variations in diffusion encoding beyond Stejskal-Tanner and other parameters (e.g. TE, inversion t(TI)) per volume and per slice are becoming more common (Section 5.3), requiring new ways of standardization. The Brain Imaging Data Structure (BIDS) (Gorgolewski et al., 2016) format has been proposed as a standard for organizing and describing MRI datasets using file formats compatible with existing software: the data is stored in the NifTI format and additional metadata such as acquisition details in JavaScript Object Notation (JSON). In addition, BIDS specifies a directory structure to deal with different subjects, sessions, and imaging modalities, and allows the addition of supplementary files and new metadata keys. A standardization for advanced dMRI data (aDWI-BIDS) has recently been proposed to handle arbitrary diffusion encoding gradients and RF pulses, and to specify sequence parameters at different scales ranging from the entire image to a single voxel (Gholam et al., 2021). This should greatly facilitate the processing of dMRI data and the development of new tools.

With the lack of comprehensive data standards comes the challenge of poor interoperability between software packages that commonly read, interpret, and write data in different ways; e.g. the order of estimated DT and spherical harmonics components, the handling of scaling factors, or information associated with both image and B-matrix coordinate spaces. This greatly challenges the combination of tools from different packages into a flexible pipeline. In addition to BIDS standardization for raw dMRI data, standardizing derivatives (i.e. outputs of processing pipelines for subsequent processing) in the BIDS format can provide machine-readable access and enable higher level processing. Moreover, not all packages are open source and data handling may change with different versions, which further challenges the translation and compatibility between software tools. It is therefore good practise to always mention the version number of the software packages used in a study. Further, the challenges with installation of different packages can hamper the construction and execution of pipelines, for example when only certain operator systems are supported or when root access is required. While efforts have been made to improve compatibility and pipeline design e.g. through the increased availability of documentation and conversion tools, further standardization and the possibility to create flexible pipelines comprising different tools are important moving forward. Containers solve some of these issues: Docker containers are easily run on cloud services and personal computers, while Singularity is more suited for high performance computing clusters and does not require root access. BIDS Apps (Gorgolewski et al., 2017) are versioned container images that take BIDS formatted datasets as input and several BIDS-compatible tools have been developed for dMRI preprocessing, including Tractoflow (Theaud et al., 2020), QSIprep (Cieslak et al., 2020), MRtrix3_connectome (https://github.com/BIDS-Apps/MRtrix3_connectome), dMRIPrep (<https://github.com/nipreps/dmriprep>), and QuNex (<https://bitbucket.org/oriadev/qunex/wiki/Home>). As such, containers and BIDS Apps can greatly improve the ease of use and reproducibility of dMRI preprocessing pipelines. Finally, code availability might not be sufficient to guide the user through this complex task. Thorough reporting allow users to better understand and quality-check the

various pipeline-steps; such reports ideally include QC of the data format and metadata (e.g. acquisition parameters), the unprocessed data (e.g. SNR and angular CNR), and the processed data (e.g. motion estimates) (Esteban et al., 2018). The vast amount of interaction on user groups of several platforms also demonstrates the importance of creating a community of users to keep tackling questions and tune the software to the users' needs.

Even though open source pipelines are desirable in all situations, they might also bring additional challenges. Many of the aforementioned dMRI pipelines use either open-source libraries or tools from other pipelines that are released with different and incompatible licenses. For developers from strictly regulated institutions, these issues need to be overcome for a fully transparent development process. Likewise, making data publicly available for benchmarking is challenged by privacy considerations – in the European Union for example regulated by the General Data Protection Regulation (GDPR, <https://gdpr-info.eu/>) – and the potential of data containing commercially sensitive information such as gradient system specifications (see e.g. section 2.13).

Despite ongoing efforts of data standardization and distribution of open source software, the wide variability (even when running the same pipeline twice) and degrees of freedom in image preprocessing have been identified as a source in the, often, poor reproducibility of neuroimaging studies (Cetin Karayumak et al., 2020; Theaud et al., 2020). Therefore, as a scientific community, we must keep striving to minimize, or at least understand, the impact of the variability in applied image preprocessing pipelines on the outcome of our studies (Botvinik-Nezer et al., 2020).

5.2. Acquisition, image reconstruction, and preprocessing should be integrated

During the past years, we witnessed a rapidly growing trend of integrating data acquisition, image reconstruction, and image preprocessing during experimental design. As a result, the design of a scan protocol is more often attuned to the planned image preprocessing pipeline. The acquisition of reversed phase encoding data or the uniform distribution of $b = 0$ images across the time series is becoming more widely adopted in clinical and research studies, in part because such modifications to the image protocol are available to most users. However, the user must often overwrite the vendor's default setting and, for example, provide a customized gradient direction file.

Another example where the acquisition strategy may impact dMRI preprocessing and QC is the adoption of strategies to accelerate the data acquisition: (a) parallel MRI, (b) SMS or multiband, and (c) partial Fourier. In case of parallel imaging, one reduces the duration of the EPI readout, thereby reducing the overall scan time, the magnitude of the susceptibility-induced geometric distortion, and the SNR. In combination with the loss in SNR, the noise amplification is spatially dependent, leading to non-stationary noise levels that require customized tools. In contrast, SMS leads to a reduction in acquisition time with no impact on distortion or SNR. However, SMS can introduce additional artifacts to the images, especially when used with large speed-up factors. Unlike in-plane parallel imaging, the positive and negative effects of SMS on diffusion MRI have yet to be fully characterized. Partial Fourier is a widely adopted imaging strategy that allows for a significant acceleration of data acquisition by exploiting the conjugate symmetry of the k -space. Moreover, the SNR penalty can in part be compensated by shortening the echo time. Unfortunately, the incomplete measurement of k -space might cause spurious ringing along the phase-encoding direction of the resulting image if zero-filling is used for image reconstruction. Unlike the classical Gibbs phenomenon, this spurious ringing has a varying frequency and phase. It has been shown that this ringing pattern cannot be resolved using classical subvoxel shifting or convolutional neural networks if only magnitude MRI data is available.

Improved integration of acquisition, reconstruction, and preprocessing may affect the pipeline-order, and even make some preprocessing

steps redundant in the future. An increasing number of studies have showed that the performance of image preprocessing pipelines can further be improved by performing several preprocessing steps on the k -space, complex coil data, or complex combined data. If available, various studies demonstrated that the performance of denoising and Gibbs correction improved and becomes more general applicable. Moreover, enhancing the SNR by denoising the complex data, or avoiding the magnitude operator in its entirety by promoting real- or complex-valued diffusion MRI, holds the promise of more accurate and precise quantitative analysis because the signal will not be perturbed with the Rician or noncentral-Chi bias. Acquisition-side artifact corrections include prospective motion correction, field camera eddy current correction, high order b_0 shimming, novel reconstruction strategies, or parallel RF transmission (pTx) for B_1 field optimization. Unfortunately, the development and evaluation of such approaches are currently challenged by limited availability or access to data formats and/or equipment. Conversely, with novel processing algorithms, some acquisition-side artifact remedies could be moved to the processing side (e.g. the correction of eddy current distortions through image registration rather than twice-refocused acquisitions which penalize TE). As acquisition strategies improve, preprocessing strategies will adapt; therefore, determining the most effective way to handle an artifact or distortion will continue to be an interesting engineering problem.

5.3. The need for the extension of tools beyond adult in vivo human brain and conventional PGSE EPI

In this review, we have mostly focused on several techniques and recent developments for preprocessing dMRI human brain data acquired in vivo from healthy young adults using PGSE sequences. However, this scenario represents only a fraction within the breadth of applications that awaits to be explored; we will discuss here extensions to lifespan and cross-species imaging, other sequences and imaging dimensions (e.g. relaxometry), and high resolution imaging.

The brain constantly changes with age, and so do its structural connectivity fingerprint (Cox et al., 2016; Lebel et al., 2012) and microstructural properties (Beck et al., 2021; Cetin-Karayumak et al., 2020). However, because of these changes and other challenges such as increased motion at young/old age, the typical preprocessing pipeline used for young adult data may not always be optimal for other ages. Since the HCP and the related methodological advancements (Sotiropoulos et al., 2013c), new preprocessing pipelines that can deal with dMRI data acquired across different age ranges have been developed. These were brought forward by other big international consortia, such as the developing Human Connectome Project (Bastiani et al., 2019a; Hutter et al., 2018b), the Adolescent Brain Cognitive Development (ABCD) study (Hagler et al., 2019), the UK BioBank (Alfaro-Almagro et al., 2018) and the HCP Lifespan extensions (Harms et al., 2018).

Studying different species would enable to define a functionally relevant common framework (Mars et al., 2018; Passingham et al., 2002) and translatability of findings (Mars et al., 2021). Connectome mapping efforts are underway across several species (see, eg., (Autio et al., 2020; Sinke et al., 2018)), and these will lead to optimised preprocessing tools that will allow to deal with species-specific issues.

Furthermore, in recent years, several new acquisition protocols based on novel waveforms have been developed, moving away from the standard Stejskal-Tanner PGSE 'linear tensor encoding' approach (Stejskal and Tanner, 1965) defined by a b -vector and b -value to an extended B-tensor representation (Westin et al., 2016). Spherical and planar encoding techniques have been shown to provide orthogonal information that can potentially be used to resolve some of the microstructural modelling degeneracies which are commonly observed when analysing dMRI data (Cottaar et al., 2020; Lampinen et al., 2019; Szczepankiewicz et al., 2015; Tax et al., 2019b). Spherical tensor-, planar tensor-, and other free gradient waveform-based dMRI data can be affected by several imaging artifacts and sources of signal error. Differ-

ences in signal dependency e.g. as a function of b -value between encoding strategies make the development of bespoke preprocessing tools necessary, for example when using prediction-based strategies to correct for subject motion and eddy current distortions (Nilsson et al., 2018). While the effects of concomitant gradients or Maxwell terms – which are additional nonlinear fields present in the transverse direction thus invalidating the assumption of linear gradients along the principle magnetic field direction – are commonly considered negligible in conventional symmetrical Stejskal Tanner encoding (Baron et al., 2012) and therefore not discussed here, this may not be the case for asymmetric free gradient waveforms (Szczepankiewicz et al., 2019). Careful design of the waveforms can compensate for the detrimental effects of concomitant fields, as well as eddy currents (Yang and McNab, 2019) and motion (Szczepankiewicz et al., 2021).

In addition to new flavors of diffusion encoding, the dimensionality of data for in vivo microstructural imaging is increasing beyond a single contrast; correlation experiments vary multiple MRI parameters to extract joint and complementary information from different modalities. This approach has been common in NMR for several decades, but with advances in MRI hardware and software, it has also gained popularity in imaging of the human brain. Several studies for example combine the variation in diffusion encoding parameters (i.e. b -value and b -vector, or more generally the B-matrix) with variations in parameters related to probing relaxation (i.e. TE (Lampinen et al., 2020; Tax et al., 2017; Veraart et al., 2018), and inversion time (Hutter et al., 2018a)) and susceptibility (i.e. delay time w.r.t. the echo centre (Kleban et al., 2020)). In addition to volume-wise parameter variations, MRI acquisition settings can also vary slice-wise, e.g. when using slice-level interleaved diffusion encoding and slice-shuffling for efficient diffusion-relaxation correlation MRI. As such, a ‘dMRI dataset’ can have parameter variations beyond what is traditionally captured with b -value and b -vector files, and preprocessing tools have to be adapted accordingly. For example, eddy current distortions can manifest differently if the timing of the diffusion pulses is kept fixed and TE varied. As with variations in B-tensor encoding and diffusion time, such datasets can be processed individually and registered retrospectively, but this would lead to additional interpolation steps. Preprocessing techniques start to be adapted to and evaluated in multi-parametric MRI scenarios, e.g. denoising (Grussu et al., 2020b).

With the post-HCP advent of improved hardware and k -space sampling techniques, sub-millimeter dMRI data resolutions can be achieved (Ramos-Llordén et al., 2020; Wang et al., 2020a). Therefore, it becomes crucial to develop new preprocessing tools that can reliably correct for, e.g., small amounts of motion. One solution may be to adopt markerless motion tracking systems (Berghlund et al., 2021) that can be used across subjects. However, this may not solve issues related with pulsatile motion (Truong and Guidon, 2014). The acquisition of *ex vivo* brain tissue represents another route to achieve higher resolution and, when combined with histological techniques, could potentially provide the neuroimaging community with very useful insights into developing early disease biomarkers or novel dMRI modelling approaches (Bastiani et al., 2017; Howard et al., 2019). However, also in this specific situation, while correcting for motion-induced artifacts may not be the primary aim of an *ex vivo* data preprocessing pipeline, several other factors, such as tissue deformation and signal-changes due to decay and fixation agent need to be taken into account (Roebroek et al., 2019).

As a consensus of optimal pipelines for conventional data is already lacking, devising a preprocessing pipeline that can reliably deal with data coming from all these different dimensions is very challenging. Single tools have been successfully applied across different studies and data types and their reliability has been quantitatively assessed (Oldham et al., 2020). However, only recently some works have started assessing the generalizability of different whole preprocessing pipelines to analyse human brain multi-shell dMRI data (Ades-Aron et al., 2018; Brun et al., 2019; Cai et al., 2021a; Cui et al., 2013; Maximov et al., 2019; Oguz et al., 2014). It should be noted that both pipelines and data need to be harmonised in order to have a truly generalizable pre-

processing framework, and the latter could be achieved faster with the collaboration of the MRI system vendors.

5.4. The future of dMRI preprocessing with machine learning

Machine learning (ML), specifically deep learning (DL), has gained a tremendous amount of attention over the last decade. Deep neural networks are now the state-of-the-art machine learning models across a variety of areas, from image analysis to natural language processing, and widely deployed in both academia and industry. These developments have a huge potential for MRI technology, data analysis, diagnostics and healthcare in general, which are slowly being realized. DL has seen applications at each step of the MRI pipeline, from acquisition and image reconstruction to image preprocessing and retrieval, from segmentation to disease prediction.

Deep learning’s primary MRI applications have focused on segmentation and classification (for diagnosis) of images. Its relatively more recent utilization at earlier stages of the MRI pipeline has already shown impressive results. The advantages brought by DL techniques to MRI acquisition and reconstruction in general have already been established, with early works (Schlemper et al., 2018; Wang et al., 2016; Yang et al., 2016) using CNNs and recurrent neural networks (RNN) for acquisition speed-up and dynamic image reconstruction from undersampled k -space data. A unified framework for image reconstruction (Zhu et al., 2018), AUTOMAP, combined a fully-connected feedforward deep neural network with a sparse convolutional autoencoder and was trained on the HCP dataset to generate a mapping between the sensor and the image domain data. Recently, NYU Langone Health and Facebook AI Research started an initiative called fastMRI with the goal of achieving a speed-up factor of ten for MRI acquisitions. The use of these faster acquisition and reconstruction techniques have also been investigated for dMRI. Mani et al. (2020) proposed a model-based DL architecture for the reconstruction of highly accelerated dMRI that enables high resolution imaging. The DeepDTI framework (Tian et al., 2020) aims to achieve a high data quality with the minimal acquisition of a single $b = 0$ s/mm^2 and six diffusion-weighted volumes.

Super-resolution (or super-sampling) is another exciting application of DL methods. Even though such techniques have been around for a while, the introduction of deep learning has been relatively recent (Bahrami et al., 2017; Zeng et al., 2018). Elsaid and Wu (2019) investigated the feasibility of super-resolution in DTI. Hong et al. (2019) aimed to reduce acquisition time by undersampling the slice dimension and regenerating the high resolution images with DL methods, and similarly Tian et al. (2021) proposed SRDTI to reduce scan times and achieve high data quality. Alexander et al. (2017) showed that application of “image quality transfer” to low resolution dMRI data dramatically outperforms interpolation in increasing image resolution. Given that dMRI data need to undergo interpolation during preprocessing, these DL based interpolation and super-sampling techniques have the potential to be a key component in all dMRI preprocessing pipelines in the future.

Another area that is developing within the context of deep learning for MRI is the estimation of quantitative tissue parameters from recorded complex-valued or magnitude data. These approaches are already being used for quantitative susceptibility mapping and MR fingerprinting, and are also of particular interest to dMRI-based investigation of microstructure as shown in recent studies (de Almeida Martins et al., 2021; Golkov et al., 2016; Grussu et al., 2020a; Ye, 2017; Ye et al., 2019).

The inter-volume motion (Section 2.7), eddy-currents distortion (Section 2.9), susceptibility distortion (Section 2.11) and dMRI spatial normalization (Section 2.15) processing steps generally involve the use of image registration techniques, which is another field particularly suitable for deep learning methods. The long computational times involved in image registration, especially diffeomorphic registration, benefit tremendously from these approaches (Balakrishnan et al., 2019; de Vos et al., 2019; Shan et al., 2018; Wu et al., 2016).

Possibly, the most interesting application of machine learning to dMRI preprocessing will be in the area of image restoration, i.e. for denoising (see Section 2.6), artifact detection, artifact removal, image synthesis, distortion correction and quality assurance. The variety of artifacts DL methods have been and are being applied to are numerous: Several groups have proposed methods to detect and possibly remove motion artifacts from MRI data (Duffy et al., 2021; Küstner et al., 2018; Pawar et al., 2018), others tackled Gibbs ringing- (Muckley et al., 2021; Zhang et al., 2019) (see Section 2.4), metal- (Seo et al., 2020) and banding artifacts (Kim and Park, 2017). Ayub et al. (2020) proposed a deep generative model to "inpaint" overly cropped dMRI data to fill in the missing slices for both the $b = 0$ and diffusion weighted images. Samani et al. (2020) proposed a DL method to detect artifacts and provide an automated quality control (see Section 3.1.2).

Even though the future of DL is bright, at present, caution should be exercised while interpreting the outcomes and the results should be thoroughly validated. The black-box nature of DL methods can prohibit manual validation of the learned feature sets, e.g., it is challenging to determine whether a DL method successfully classified a patient MRI due to an inherent feature or solely due to the increased amount of motion-related artifacts common for the population group. In the future, with the increased expertise of machine learning researchers on improving potential instabilities (Antun et al., 2020), sensitivity, and reliability of these techniques, ML has the potential to be applied to traditionally intractable or computationally infeasible problems in each step of the dMRI pipeline.

6. Conclusion

The dMRI preprocessing pipeline is typically lengthy and complex and contains multiple steps, each of which can be performed with a broad range of tools and methods. Currently, there is no consensus on the optimal preprocessing pipeline, and the required pipeline steps can vary for different datasets. An integrated approach to acquisition and preprocessing is therefore desired: on the one hand it is necessary to have in-depth knowledge of the data to devise an appropriate pipeline, and on the other hand the acquisition strategy can be adapted when one is well-aware of the required data for desired artifact corrections. Different tools, versions, and operating platforms can cause significant variability in the analysis, and we thus urge the community to carefully report the software and version used for preprocessing in publications. Fortunately, recent developments in data- and code sharing and standardization greatly facilitate the processing of dMRI data and pave the way towards more reproducible results. We envision that data standardization, reporting, and pipelines accommodating more exotic dMRI datasets become increasingly important, and that machine learning can bring exciting new avenues for dMRI preprocessing.

Data and Code Availability Statement

All data and code developed as part of this work will be made publicly available.

Declaration of Competing Interest

JV is a co-inventor on patent US10698065B2, which described methodology presented in this manuscript.

Credit authorship contribution statement

Chantal M.W. Tax: Conceptualization, Project administration, Supervision, Visualization, Writing – original draft, Writing – review & editing. **Matteo Bastiani:** Conceptualization, Visualization, Writing – original draft, Writing – review & editing. **Jelle Veraart:** Conceptualization, Visualization, Writing – original draft, Writing – review & editing. **Eleftherios Garyfallidis:** Conceptualization, Writing – original draft,

Writing – review & editing. **M. Okan Irfanoglu:** Conceptualization, Supervision, Visualization, Writing – original draft, Writing – review & editing.

Acknowledgment

CMWT was supported by a Sir Henry Wellcome Fellowship (215944/Z/19/Z) and a Veni grant (17331) from the Dutch Research Council (NWO). MOI is supported by the Intramural Research Program of the National Institute of Biomedical Imaging and Bioengineering in the National Institutes of Health. The contents of this work do not necessarily reflect the position or the policy of the US government, and no official endorsement should be inferred. Research was performed as part of the Center of Advanced Imaging Innovation and Research (CAI2R, www.cai2r.net), an NIBIB Biomedical Technology Resource Center (NIH P41 EB017183) and was partially supported by the NINDS of the NIH (R01 NS088040). Work performed by EG for this paper was supported by the National Institute Of Biomedical Imaging And Bioengineering of the National Institutes of Health under Award Number R01EB027585.

References

- Ades-Aron, B., Veraart, J., Kochunov, P., McGuire, S., Sherman, P., Kellner, E., Novikov, D.S., Fieremans, E., 2018. Evaluation of the accuracy and precision of the diffusion parameter EStimation with gibbs and noise removal pipeline. *Neuroimage* 183, 532–543. doi:10.1016/j.neuroimage.2018.07.066. URL <https://www.ncbi.nlm.nih.gov/pmc/articles/PMC6371781/>.
- Aja-Fernández, S., Brion, V., Tristán-Vega, A., 2013. Effective noise estimation and filtering from correlated multiple-coil mr data. *Magn Reson Imaging* 31 (2), 272–285.
- Aksoy, M., Forman, C., Straka, M., Skare, S., Holdsworth, S., Hornegger, J., Bammer, R., 2011. Real-time optical motion correction for diffusion tensor imaging. *Magn Reson Med* 66 (2), 366–378. doi:10.1002/mrm.22787.
- Alexander, A.L., Tsuruda, J.S., Parker, D.L., 1997. Elimination of eddy current artifacts in diffusion-weighted echo-planar images: the use of bipolar gradients. *Magn Reson Med* 38 (6), 1016–1021. doi:10.1002/mrm.1910380623. URL <https://www.ncbi.nlm.nih.gov/pubmed/9402204>
- Alexander, D.C., Dyrby, T.B., Nilsson, M., Zhang, H., 2019. Imaging brain microstructure with diffusion mri: practicality and applications. *NMR Biomed* 32 (4), e3841. doi:10.1002/nbm.3841.
- Alexander, D.C., Zikic, D., Ghosh, A., Tanno, R., Wotschel, V., Zhang, J., Kaden, E., Dyrby, T.B., Sotiropoulos, S.N., Zhang, H., Criminisi, A., 2017. Image quality transfer and applications in diffusion mri. *Neuroimage* 152, 283–298. URL <https://www.sciencedirect.com/science/article/pii/S1053811917302008>.
- Alfaro-Almagro, F., Jenkinson, M., Bangerter, N.K., Andersson, J.L., Griffanti, L., Douaud, G., Sotiropoulos, S.N., Jbabdi, S., Hernandez-Fernandez, M., Vallee, E., Vidaurre, D., Webster, M., McCarthy, P., Rorden, C., Daducci, A., Alexander, D.C., Zhang, H., Dragonu, I., Matthews, P.M., Miller, K.L., Smith, S.M., 2018. Image processing and quality control for the first 10,000 brain imaging datasets from UK biobank. *Neuroimage* 166, 400–424. doi:10.1016/j.neuroimage.2017.10.034.
- Alfaro-Almagro, F., McCarthy, P., Afyouni, S., Andersson, J.L., Bastiani, M., Miller, K.L., Nichols, T.E., Smith, S.M., 2021. Confound modelling in uk biobank brain imaging. *Neuroimage* 224, 117002. doi:10.1016/j.neuroimage.2020.117002. URL <https://www.sciencedirect.com/science/article/pii/S1053811920304882>.
- Alhamud, A., Tisdall, M.D., Hess, A.T., Hasan, K.M., Meintjes, E.M., van der Kouwe, A.J., 2012. Volumetric navigators for real-time motion correction in diffusion tensor imaging. *Magn Reson Med* 68 (4), 1097–1108. doi:10.1002/mrm.23314.
- de Almeida Martins, J., Nilsson, M., Lampinen, B., Palombo, M., White, P., Westin, C.-F., Szczepankiewicz, F., 2021. Neural networks for parameter estimation in microstructural mri: a study with a high-dimensional diffusion-relaxation model of white matter microstructure. 10.1101/2021.03.12.435163
- Amartur, S., Liang, Z.-P., Boada, F., Haacke, E.M., 1991. Phase-constrained data extrapolation method for reduction of truncation artifacts. *J. Magn. Reson. Imaging* 1 (6), 721–724.
- Andersson, J.L., Graham, M.S., Drobniak, I., Zhang, H., Campbell, J., 2018. Susceptibility-induced distortion that varies due to motion: correction in diffusion mr without acquiring additional data. *Neuroimage* 171, 277–295.
- Andersson, J.L., Graham, M.S., Drobniak, I., Zhang, H., Filippini, N., Bastiani, M., 2017. Towards a comprehensive framework for movement and distortion correction of diffusion MR images: within volume movement. *Neuroimage* 152, 450–466. doi:10.1016/J.NEUROIMAGE.2017.02.085. URL <https://www.sciencedirect.com/science/article/pii/S1053811917301945?via%3Dihub>.
- Andersson, J.L., Graham, M.S., Zsoldos, E., Sotiropoulos, S.N., 2016. Incorporating outlier detection and replacement into a non-parametric framework for movement and distortion correction of diffusion MR images. *Neuroimage* 141, 556–572. doi:10.1016/j.neuroimage.2016.06.058.
- Andersson, J.L., Skare, S., 2002. A model-based method for retrospective correction of geometric distortions in diffusion-weighted epi. *Neuroimage* 16 (1), 177–199. doi:10.1006/nimg.2001.1039. URL <https://www.ncbi.nlm.nih.gov/pubmed/11969328>

- Andersson, J.L., Skare, S., Ashburner, J., 2003. How to correct susceptibility distortions in spin-echo echo-planar images: application to diffusion tensor imaging. *Neuroimage* 20 (2), 870–888.
- Andersson, J.L., Sotiropoulos, S.N., 2015. Non-parametric representation and prediction of single- and multi-shell diffusion-weighted mri data using gaussian processes. *Neuroimage* 122, 166–176. doi:10.1016/j.neuroimage.2015.07.067. URL <https://www.ncbi.nlm.nih.gov/pubmed/26236030>
- Andersson, J.L., Sotiropoulos, S.N., 2016. An integrated approach to correction for off-resonance effects and subject movement in diffusion MR imaging. *Neuroimage* 125, 1063–1078. doi:10.1016/j.neuroimage.2015.10.019.
- Andersson, J.L.R., Graham, M.S., Drobnjak, I., Zhang, H., Campbell, J., 2018. Susceptibility-induced distortion that varies due to motion: correction in diffusion mr without acquiring additional data. *Neuroimage* 171, 277–295. doi:10.1016/j.neuroimage.2017.12.040. URL <https://www.ncbi.nlm.nih.gov/pubmed/29277648>.
- Antun, V., Renna, F., Poon, C., Adcock, B., Hansen, A.C., 2020. On instabilities of deep learning in image reconstruction and the potential costs of ai. *Proceedings of the National Academy of Sciences* 117 (48), 30088–30095. doi:10.1073/pnas.1907377117.
- Autio, J.A., Glasser, M.F., Ose, T., Donahue, C.J., Bastiani, M., Ohno, M., Kawabata, Y., Urushibata, Y., Murata, K., Nishigori, K., Yamaguchi, M., Hori, Y., Yoshida, A., Go, Y., Coalson, T.S., Jbabdi, S., Sotiropoulos, S.N., Kennedy, H., Smith, S., Van Essen, D.C., Hayashi, T., 2020. Towards hcp-style macaque connectomes: 24-channel 3t multi-array coil, mri sequences and preprocessing. *Neuroimage* 215, 116800. doi:10.1016/j.neuroimage.2020.116800. URL <https://www.sciencedirect.com/science/article/pii/S1053811920302871>.
- Avants, B., Epstein, C., Grossman, M., Gee, J., 2008. Symmetric diffeomorphic image registration with cross-correlation: evaluating automated labeling of elderly and neurodegenerative brain. *Med Image Anal* 12 (1), 26–41.
- Avesani, P., McPherson, B., Hayashi, S., Caiafa, C.F., Henschel, R., Garyfallidis, E., Kitchell, L., Bullock, D., Patterson, A., Olivetti, E., et al., 2019. The open diffusion data derivatives, brain data upcycling via integrated publishing of derivatives and reproducible open cloud services. *Sci Data* 6 (1), 1–13.
- Ayub, R., Zhao, Q., Meloy, M.J., Sullivan, E.V., Pfefferbaum, A., Adeli, E., Pohl, K.M., 2020. Inpainting cropped diffusion mri using deep generative models. In: Rekić, I., Adeli, E., Park, S.H., Valdés Hernández, M.D. C. (Eds.), *Predictive Intelligence in Medicine*. Springer International Publishing, pp. 91–100.
- Bahrami, K., Shi, F., Rekić, I., Gao, Y., Shen, D., 2017. 7T-guided super-resolution of 3t mri. *Med Phys* 44 (5), 1661–1677. doi:10.1002/mp.12132.
- Balakrishnan, G., Zhao, A., Sabuncu, M.R., Gutttag, J., Dalca, A.V., 2019. Voxelmorph: a learning framework for deformable medical image registration. *IEEE Trans Med Imaging* 38 (8), 1788–1800. doi:10.1109/TMI.2019.2897538.
- Bammer, R., Markl, M., Barnett, A., Acar, B., Alley, M., Pelc, N., Glover, G., Moseley, M., 2003. Analysis and generalized correction of the effect of spatial gradient field distortions in diffusion-weighted imaging. *Magn Reson Med* 50 (3), 560–569. doi:10.1002/mrm.10545.
- Bandettini, P.A., Jesmanowicz, A., Wong, E.C., Hyde, J.S., 1993. Processing strategies for time-course data sets in functional mri of the human brain. *Magn Reson Med* 30 (2), 161–173. doi:10.1002/mrm.1910300204.
- Bannister, P.R., Michael Brady, J., Jenkinson, M., 2007. Integrating temporal information with a non-rigid method of motion correction for functional magnetic resonance images. *Image Vis Comput* 25 (3), 311–320. doi:10.1016/j.imavis.2005.10.002. Articulated and Non-rigid motion, URL <https://www.sciencedirect.com/science/article/pii/S0262885606000345>.
- Barker, G., Parker, G., Wheeler-Kingshott, C., 2001. Gibbs ringing and negative adc values. In: *Proceedings of the 9th meeting of the International Society for Magnetic Resonance in Medicine*, Vol. 1546.
- Baron, C.A., Lebel, R.M., Wilman, A.H., Beaulieu, C., 2012. The effect of concomitant gradient fields on diffusion tensor imaging. *Magn Reson Med* 68 (4), 1190–1201. doi:10.1002/mrm.24120.
- Bastiani, M., Andersson, J.L., Cordero-Grande, L., Murgasova, M., Hutter, J., Price, A.N., Makropoulos, A., Fitzgibbon, S.P., Hughes, E., Rueckert, D., Victor, S., Rutherford, M., Edwards, A.D., Smith, S.M., Tournier, J.D., Hajnal, J.V., Jbabdi, S., Sotiropoulos, S.N., 2019. Automated processing pipeline for neonatal diffusion MRI in the developing human connectome project. *Neuroimage* 185, 750–763. doi:10.1016/j.neuroimage.2018.05.064.
- Bastiani, M., Cottaar, M., Dikranian, K., Ghosh, A., Zhang, H., Alexander, D.C., Behrens, T.E., Jbabdi, S., Sotiropoulos, S.N., 2017. Improved tractography using asymmetric fibre orientation distributions. *Neuroimage* 158, 205–218. doi:10.1016/j.neuroimage.2017.06.050.
- Bastiani, M., Cottaar, M., Fitzgibbon, S.P., Suri, S., Alfaro-Almagro, F., Sotiropoulos, S.N., Jbabdi, S., Andersson, J.L., 2019. Automated quality control for within and between studies diffusion MRI data using a non-parametric framework for movement and distortion correction. *Neuroimage* 184, 801–812. doi:10.1016/j.neuroimage.2018.09.073.
- Bastin, M.E., 2001. On the use of the flair technique to improve the correction of eddy current induced artefacts in mr diffusion tensor imaging. *Magn Reson Imaging* 19 (7), 937–950. doi:10.1016/S0730-725X(01)00427-1. URL <https://www.ncbi.nlm.nih.gov/pubmed/11595365>
- Bastin, M.E., Armitage, P.A., 2000. On the use of water phantom images to calibrate and correct eddy current induced artefacts in mr diffusion tensor imaging. *Magn Reson Imaging* 18 (6), 681–687. doi:10.1016/S0730-725X(00)00158-2. URL <https://www.ncbi.nlm.nih.gov/pubmed/10930777>
- Batson, J., Royer, L., 2019. Noise2self: Blind denoising by self-supervision. In: *International Conference on Machine Learning*. PMLR, pp. 524–533.
- Beall, E.B., Lowe, M.J., 2014. Simpace: generating simulated motion corrupted bold data with synthetic-navigated acquisition for the development and evaluation of slow-moco: a new, highly effective slice-wise motion correction. *Neuroimage* 101, 21–34. doi:10.1016/j.neuroimage.2014.06.038.
- Beck, D., de Lange, A.-M.G., Maximov, I.I., Richard, G., Andreassen, O.A., Nordvik, J.E., Westlye, L.T., 2021. White matter microstructure across the adult lifespan: a mixed longitudinal and cross-sectional study using advanced diffusion models and brain-age prediction. *Neuroimage* 224, 117441. doi:10.1016/j.neuroimage.2020.117441. URL <https://www.sciencedirect.com/science/article/pii/S1053811920309265>.
- Becker, S., Tabelow, K., Mohammadi, S., Weiskopf, N., Polzehl, J., 2014. Adaptive smoothing of multi-shell diffusion weighted magnetic resonance data by mspos. *Neuroimage* 95, 90–105.
- Becker, S., Tabelow, K., Voss, H.U., Anwander, A., Heidemann, R.M., Polzehl, J., 2012. Position-orientation adaptive smoothing of diffusion weighted magnetic resonance data (poas). *Med Image Anal* 16 (6), 1142–1155.
- Ben-Amity, S., Jones, D.K., Assaf, Y., 2012. Motion correction and registration of high b-value diffusion weighted images. *Magn Reson Med* 67 (6), 1694–1702. doi:10.1002/mrm.23186.
- Benner, T., van der Kouwe, A.J., Kirsch, J.E., Sorensen, A.G., 2006. Real-time rf pulse adjustment for b0 drift correction. *Magnetic Resonance in Medicine: An Official Journal of the International Society for Magnetic Resonance in Medicine* 56 (1), 204–209.
- Berglund, J., van Niekerk, A., Rydén, H., Sprenger, T., Avventi, E., Norbeck, O., Glimberg, S.L., Olesen, O.V., Skare, S., 2021. Prospective motion correction for diffusion weighted epi of the brain using an optical markerless tracker. *Magn Reson Med* 85 (3), 1427–1440. doi:10.1002/mrm.28524.
- Berl, M.M., Walker, L., Modi, P., Irfanoglu, M.O., Sarlls, J.E., Nayak, A., Pierpaoli, C., 2015. Investigation of vibration-induced artifact in clinical diffusion-weighted imaging of pediatric subjects. *Hum Brain Mapp* 36 (12), 4745–4757. doi:10.1002/hbm.22846.
- Block, K.T., Uecker, M., Frahm, J., 2008. Suppression of mri truncation artifacts using total variation constrained data extrapolation. *Int J Biomed Imaging* 2008.
- Bodammer, N., Kaufmann, J., Kanowski, M., Tempelmann, C., 2004. Eddy current correction in diffusion-weighted imaging using pairs of images acquired with opposite diffusion gradient polarity. *Magn Reson Med* 51 (1), 188–193. doi:10.1002/mrm.10690. URL <https://www.ncbi.nlm.nih.gov/pubmed/14705060>
- Botvinick-Nezer, R., Holzmeister, F., Camerer, C.F., Dreber, A., Huber, J., Johannesson, M., Kirchler, M., Iwanir, R., Mumford, J.A., Adcock, R.A., Avesani, P., Baczkowski, B.M., Bajracharya, A., Bakst, L., Ball, S., Barilari, M., Bault, N., Beaton, D., Beutner, J., Benoit, R.G., Berkers, R.M.W.J., Bhanji, J.P., Biswal, B.B., Bobadilla-Suarez, S., Borotolini, T., Bottenhorn, K.L., Bowring, A., Braem, S., Brooks, H.R., Brudner, E.G., Calderon, C.B., Camilleri, J.A., Castrellon, J.J., Cecchetti, L., Cieslik, E.C., Cole, Z.J., Collignon, O., Cox, R.W., Cunningham, W.A., Czoschke, S., Dadi, K., Davis, C.P., Luca, A.D., Delgado, M.R., Demetriou, L., Dennison, J.B., Di, X., Dickie, E.W., Dobryakova, E., Donnat, C.L., Dukart, J., Duncan, N.W., Durnez, J., Eed, A., Eickhoff, S.B., Erhart, A., Fontanesi, L., Fricke, G.M., Fu, S., Galván, A., Gau, R., Genon, S., Glatard, T., Glerean, E., Goeman, J.J., Golowin, S.A.E., González-García, C., Gorgolewski, K.J., Grady, C.L., Green, M.A., Guassi Moreira, J.F., Guest, O., Hakim, S., Hamilton, J.P., Hancock, R., Handjaras, G., Harry, B.B., Hawco, C., Herholz, P., Herman, G., Heunis, S., Hoffstaedter, F., Hogeveen, J., Holmes, S., Hu, C.-P., Huetel, S.A., Hughes, M.E., Iacovella, V., Jordan, A.D., Isager, P.M., Isik, A.I., Jahn, A., Johnson, M.R., Johnstone, T., Joseph, M.J.E., Juliano, A.C., Kable, J.W., Kassinosopoulos, M., Koba, C., Kong, X.-Z., Koscić, T.R., Kucukboyaci, A.N., Kuhl, B.A., Kupek, S., Laird, A.R., Lamm, C., Langner, R., Lauharatanahirun, N., Lee, H., Lee, S., Leemans, A., Leo, A., Lesage, E., Li, F., Li, M.Y.C., Lim, P.C., Lintz, E.N., Liphardt, S.W., Lüsebeck Vermeer, A.B., Love, B.C., Mack, M.L., Malpica, N., Marins, T., Maumet, C., McDonald, K., McGuire, J.T., Melero, H., Méndez Leal, A.S., Meyer, B., Meyer, K.N., Mihai, G., Mitsis, G.D., Moll, J., Nielson, D.M., Nilsson, G., Notter, M.P., Olivetti, E., Onicas, A.I., Papale, P., Patil, K.R., Peltle, J.E., Pérez, A., Pischke, D., Po-line, J.-B., Prystaika, Y., Ray, S., Reuter-Lorenz, P.A., Reynolds, R.C., Ricciardi, E., Rieck, J.R., Rodriguez-Thompson, A.M., Romy, A., Salo, T., Samanez-Larkin, G.R., Sanz-Morales, E., Schlichting, M.L., Schultz, D.H., Shen, Q., Sheridan, M.A., Silvers, J.A., Skagerlund, K., Smith, A., Smith, D.V., Sokol-Hessner, P., Steinkamp, S.R., Tashjian, S.M., Thirion, B., Thorp, J.N., Tinghög, G., Tisdall, L., Tompson, S.H., Toro-Serey, C., Torre Tresols, J.J., Tozzi, L., Truong, V., Turella, L., van 't Veer, A.E., Verguts, T., Vettel, J.M., Vijayarajah, S., Vo, K., Wall, M.B., Weeda, W.D., Weis, S., White, D.J., Wisniewski, D., Xifra-Porras, A., Yearling, E.A., Yoon, S., Yuan, R., Yuen, K.S.L., Zhang, L., Zhang, X., Zosky, J.E., Nichols, T.E., Poldrack, R.A., Schonberg, T., 2020. Variability in the analysis of a single neuroimaging dataset by many teams. *Nature* 2020 582:7810 582 (7810), 84–88. doi:10.1038/s41586-020-2314-9.
- Bowtell, R.W., McIntyre, D.J.O., Command, M.J., Glover, P.M., Mansfield, P., 1994. Correction of geometric distortion in echo planar images. In: *Proceedings of 2nd Annual Meeting of the SMR, San Francisco*, p. 411.
- Bruder, H., Fischer, H., Reinfelder, H.-E., Schmitt, F., 1992. Image reconstruction for echo planar imaging with nonequidistant k-space sampling. *Magn Reson Med* 23 (2), 311–323. doi:10.1002/mrm.1910230211.
- Brun, L., Pron, A., Sein, J., Deruelle, C., Coulon, O., 2019. Diffusion MRI: assessment of the impact of acquisition and preprocessing methods using the brainVISA-Diffuse toolbox. *Front Neurosci* 13 (JUN), 536. doi:10.3389/fnins.2019.00536.
- Buonocore, M., Gao, L., 1997. Ghost artifact reduction for echo planar imaging using image phase correction. *Magn Reson Med* 38, 89–100.
- Cai, L.Y., Yang, Q., Hansen, C.B., Nath, V., Ramadass, K., Johnson, G.W., Conrad, B.N., Boyd, B.D., Begnoche, J.P., Beason-Held, L.L., Shafer, A.T., Resnick, S.M., Taylor, W.D., Price, G.R., Morgan, V.L., Rogers, B.P., Schilling, K.G., Landman, B.A., 2021. Prequal: an automated pipeline for integrated preprocessing and quality assurance of diffusion weighted mri images. *bioRxiv* doi:10.1101/2020.09.14.260240.
- Cai, L.Y., Yang, Q., Hansen, C.B., Nath, V., Ramadass, K., Johnson, G.W., Conrad, B.N., Boyd, B.D., Begnoche, J.P., Beason-Held, L.L., et al., 2021b. Prequal: an automated pipeline for integrated preprocessing and quality assurance of diffusion weighted mri images. *Magn Reson Med* 86 (1), 456–470.

- Cai, L. Y., Yang, Q., Kanakaraj, P., Nath, V., Newton, A. T., Edmonson, H. A., Luci, J., Conrad, B. N., Price, G. R., Hansen, C. B., Kerley, C. I., Ramadass, K., Yeh, F. C., Kang, H., Garyfallidis, E., Descoteaux, M., Rheault, F., Schilling, K. G., Landman, B. A., 2020. MASIVar: Multisite, multiscanner, and multisubject acquisitions for studying variability in diffusion weighted magnetic resonance imaging. *10.1101/2020.12.03.408567*
- Cetin-Karayumak, S., Di Biase, M.A., Chunga, N., Reid, B., Somes, N., Lyall, A.E., Kelly, S., Solgun, B., Pasternak, O., Vangel, M., Pearlson, G., Tamminga, C., Sweeney, J.A., Clementz, B., Schretlen, D., Viher, P.V., Stegmayer, K., Walther, S., Lee, J., Crow, T., James, A., Voineskos, A., Buchanan, R.W., Szeszko, P.R., Malhotra, A.K., Hegde, R., McCarley, R., Keshavan, M., Shenton, M., Rath, Y., Kubicki, M., 2020. White matter abnormalities across the lifespan of schizophrenia: a harmonized multi-site diffusion MRI study. *Mol. Psychiatry* 25 (12), 3208–3219. doi:10.1038/s41380-019-0509-y.
- Cetin Karayumak, S., O'Sullivan, L., Gabriella Lyons, M., Billah, T., Pasternak, O., Bouix, S., Kubicki, M., Rath, Y., 2020. Reproducibility crisis in diffusion MRI: Contribution of software processing pipelines. In: *ISMRM*, p. 4380.
- Chamberland, M., Bernier, M., Girard, F., Fortin, D., Descoteaux, M., Whittingstall, K., 2019. Penhthera 1.5T doi:10.5281/ZENODO.260222.
- Chang, H., Fitzpatrick, J.M., 1992. A technique for accurate magnetic resonance imaging in the presence of field inhomogeneities. *IEEE TMI* 11 (3), 319–329.
- Chang, H.-C., Chen, N.-K., 2016. Joint correction of nyquist artifact and minuscule motion-induced aliasing artifact in interleaved diffusion weighted epi data using a composite two-dimensional phase correction procedure. *Magn Reson Imaging* 34 (7), 974–979. doi:10.1016/j.mri.2016.04.017.
- Chang, L.-C., Jones, D.K., Pierpaoli, C., 2005. RESTORE: Robust estimation of tensors by outlier rejection. *Magn Reson Med* 53 (5), 1088–1095. doi:10.1002/mrm.20426.
- Chang, L.-C., Walker, L., Pierpaoli, C., 2012. $\langle i \rangle$ RESTORE: A method for robust estimation of diffusion tensor from low redundancy datasets in the presence of physiological noise artifacts. *Magn Reson Med* 68 (5), 1654–1663. doi:10.1002/mrm.24173.
- Chen, B., Guo, H., Song, A.W., 2006. Correction for direction-dependent distortions in diffusion tensor imaging using matched magnetic field maps. *Neuroimage* 30 (1), 121–129. doi:10.1016/j.neuroimage.2005.09.008. URL <https://www.ncbi.nlm.nih.gov/pubmed/16242966>
- Chen, N.-k., Wyrwicz, A.M., 2004. Removal of epi nyquist ghost artifacts with two-dimensional phase correction. *Magn Reson Med* 51 (6), 1247–1253. doi:10.1002/mrm.20097.
- Choi, I.-Y., Kreis, R., 2021. Advanced methodology for in vivo magnetic resonance spectroscopy. *NMR Biomed* 34 (5), e4504. doi:10.1002/nbm.4504. E4504 NBM-21-0055.
- Christiaens, D., Cordero-Grande, L., Pietsch, M., Hutter, J., Price, A.N., Hughes, E.J., Vecchiato, K., Deprez, M., Edwards, A.D., Hajnal, J.V., Tournier, J.D., 2021. Scattered slice SHARD reconstruction for motion correction in multi-shell diffusion MRI. *Neuroimage* 225, 117437. doi:10.1016/j.neuroimage.2020.117437.
- Cieslak, M., Cook, P.A., He, X., Yeh, F.C., Dhollander, T., Adebimpe, A., Aguirre, G.K., Bassett, D.S., Betzel, R.F., Bourque, J., Cabral, L.M., Davatzikos, C., Detre, J., Earl, E., Elliott, M.A., Fadnavis, S., Fair, D.A., Foran, W., Fotiadis, P., Garyfallidis, E., Giesbrecht, B., Gur, R.C., Gur, R.E., Kelz, M., Keshavan, A., Larsen, B.S., Luna, B., Mackey, A.P., Milham, M., Oathes, D.J., Perrone, A., Pines, A.R., Roalf, D.R., Richie-Halford, A., Rokem, A., Sydnor, V.J., Tapera, T.M., Tooley, U.A., Vettel, J.M., Yeatman, J.D., Grafton, S.T., Satterthwaite, T.D., 2021. QSIprep: an integrative platform for preprocessing and reconstructing diffusion MRI data. *Nature Methods* 18, 775–778.
- Clare, S., 2003. Iterative nyquist ghost correction for single and multi-shot EPI using an entropy measure. In: *Proceedings of International Society of Magnetic Resonance in Medicine*, p. 1041.
- Collier, Q., Veraart, J., Jeurissen, B., den Dekker, A.J., Sijbers, J., 2015. Iterative reweighted linear least squares for accurate, fast, and robust estimation of diffusion magnetic resonance parameters. *Magn Reson Med* 73 (6), 2174–2184. doi:10.1002/mrm.25351.
- Constable, R., Henkelman, R., 1991. Data extrapolation for truncation artifact removal. *Magn Reson Med* 17 (1), 108–118.
- Cordero-Grande, L., Christiaens, D., Hutter, J., Price, A.N., Hajnal, J.V., 2019. Complex diffusion-weighted image estimation via matrix recovery under general noise models. *Neuroimage* 200, 391–404.
- Cottaar, M., Szczepankiewicz, F., Bastiani, M., Hernandez-Fernandez, M., Sotiropoulos, S.N., Nilsson, M., Jbabdi, S., 2020. Improved fibre dispersion estimation using b-tensor encoding. *Neuroimage* 215, 116832. doi:10.1016/j.neuroimage.2020.116832. URL <https://www.sciencedirect.com/science/article/pii/S1053811920303190>
- Coupé, P., Manjón, J.V., Gedamu, E., Arnold, D., Robles, M., Collins, D.L., 2010. Robust rician noise estimation for mr images. *Med Image Anal* 14 (4), 483–493.
- Cox, R.W., 1996. Afni: software for analysis and visualization of functional magnetic resonance neuroimages. *Comput. Biomed. Res.* 29 (3), 162–173.
- Cox, R.W., Ashburner, J., Breman, H., Fissell, K., Haselgrove, C., Holmes, C.J., Lancaster, J.L., Rex, D.E., Smith, S.M., Woodward, J.B., Strother, S.C., 2004. A (Sort of) New Image Data Format Standard: NIFTI-1. *Organization for Human Brain Mapping*.
- Cox, S.R., Ritchie, S.J., Tucker-Drob, E.M., Liewald, D.C., Hagenaars, S.P., Davies, G., Wardlaw, J.M., Gale, C.R., Bastin, M.E., Deary, I.J., 2016. Ageing and brain white matter structure in 3,513 uk biobank participants. *Nat Commun* 7 (1), 13629. doi:10.1038/ncomms13629.
- Cui, Z., Zhong, S., Xu, P., He, Y., Gong, G., 2013. Panda: a pipeline toolbox for analyzing brain diffusion images. *Front Hum Neurosci* 7. doi:10.3389/fnhum.2013.00042. 42–42, URL <https://pubmed.ncbi.nlm.nih.gov/23439846> <https://www.ncbi.nlm.nih.gov/pmc/articles/PMC3578208/>.
- de Vos, B.D., Berendsen, F.F., Viergever, M.A., Sokooti, H., Staring, M., Išgum, I., 2019. A deep learning framework for unsupervised affine and deformable image registration. *Med Image Anal* 52, 128–143. doi:10.1016/j.media.2018.11.010.
- Di Tommaso, P., Chatzou, M., Floden, E. W., Barja, P. P., Palumbo, E., Notredame, C., 2017. Nextflow enables reproducible computational workflows. *10.1038/nbt.3820*
- Dietrich, O., Raya, J.G., Reeder, S.B., Ingrisch, M., Reiser, M.F., Schoenberg, S.O., 2008. Influence of multichannel combination, parallel imaging and other reconstruction techniques on MRI noise characteristics. *Magn Reson Imaging* 26 (6), 754–762. doi:10.1016/j.mri.2008.02.001.
- Ding, Z., Gore, J.C., Anderson, A.W., 2005. Reduction of noise in diffusion tensor images using anisotropic smoothing. *Magnetic Resonance in Medicine: An Official Journal of the International Society for Magnetic Resonance in Medicine* 53 (2), 485–490.
- Donoho, D., Gavish, M., et al., 2014. Minimax risk of matrix denoising by singular value thresholding. *Ann Stat* 42 (6), 2413–2440.
- Doran, S.J., Charles-Edwards, L., Reinsberg, S.A., Leach, M.O., 2005. A complete distortion correction for MR images: i. gradient warp correction. *Phys Med Biol* 50 (7), 1343–1361. doi:10.1088/0031-9155/50/7/001.
- Duffy, B.A., Zhao, L., Sepehrband, F., Min, J., Wang, D.J., Shi, Y., Toga, A.W., Kim, H., 2021. Retrospective motion artifact correction of structural MRI images using deep learning improves the quality of cortical surface reconstructions. *Neuroimage* 230, 117756. doi:10.1016/j.neuroimage.2021.117756.
- Duong, S.T., Phung, S.L., Bouzardoum, A., Schira, M.M., 2020. An unsupervised deep learning technique for susceptibility artifact correction in reversed phase-encoding epi images. *Magn Reson Imaging* 71, 1–10. doi:10.1016/j.mri.2020.04.004. URL <https://www.sciencedirect.com/science/article/pii/S0730725X19307325>.
- Eichner, C., Cauley, S.F., Cohen-Adad, J., Möller, H.E., Turner, R., Setsompop, K., Wald, L.L., 2015. Real diffusion-weighted MRI enabling true signal averaging and increased diffusion contrast. *Neuroimage* 122, 373–384. doi:10.1016/j.neuroimage.2015.07.074. URL <http://www.ncbi.nlm.nih.gov/pubmed/26241680> <http://www.pubmedcentral.nih.gov/articlerender.fcgi?artid=PMC4651971>.
- Elsaid, N.M.H., Wu, Y.C., 2019. Super-resolution diffusion tensor imaging using sr-cnn: A feasibility study*. In: *2019 41st Annual International Conference of the IEEE Engineering in Medicine and Biology Society (EMBC)*, pp. 2830–2834. doi:10.1109/EMBC.2019.8857125.
- Embleton, K.V., Haroon, H.A., Morris, D.M., Ralph, M.A., Parker, G.J., 2010. Distortion correction for diffusion-weighted mri tractography and fmri in the temporal lobes. *Hum Brain Mapp* 31 (10), 1570–1587. doi:10.1002/hbm.20959. URL <https://www.ncbi.nlm.nih.gov/pubmed/20143387>
- Eskildsen, S.F., Coupé, P., Fonov, V., Manjón, J.V., Leung, K.K., Guizard, N., Wassef, S.N., Østergaard, L.R., Collins, D.L., Initiative, A.D.N., et al., 2012. Beast: brain extraction based on nonlocal segmentation technique. *Neuroimage* 59 (3), 2362–2373.
- Esteban, O., Birman, D., Schaer, M., Koyejo, O.O., Poldrack, R.A., Gorgolewski, K.J., 2017. MRIQC: Advancing the automatic prediction of image quality in MRI from unseen sites. *PLoS ONE* 12 (9), e0184661. doi:10.1371/JOURNAL.PONE.0184661.
- Esteban, O., Markiewicz, C.J., Blair, R.W., Moodie, C.A., Isik, A.I., Erramuzpe, A., Kent, J.D., Goncalves, M., DuPre, E., Snyder, M., Oya, H., Ghosh, S.S., Wright, J., Durnez, J., Poldrack, R.A., Gorgolewski, K.J., 2018. Fmriprep: a robust preprocessing pipeline for functional MRI. *Nature Methods* 15 (1), 111–116. doi:10.1038/s41592-018-0235-4.
- Esteban, O., Zosso, D., Daducci, A., Bach-Cuadra, M., Ledesma-Carbayo, M.J., Thi-ran, J.-P., Santos, A., 2016. Surface-driven registration method for the structure-informed segmentation of diffusion mr images. *Neuroimage* 139, 450–461. doi:10.1016/j.neuroimage.2016.05.011.
- Fadnavis, S., Batson, J., Garyfallidis, E., 2020. Patch2self: Denoising diffusion mri with self-supervised learning. In: *Larochelle, H., Ranzato, M., Hadsell, R., Balcan, M.F., Lin, H. (Eds.), Advances in Neural Information Processing Systems, Vol. 33*, pp. 16293–16303. URL <https://proceedings.neurips.cc/paper/2020/file/bc047286b224b7bfa73d4cb02de1238d-Paper.pdf>
- Fan, Q., Witzel, T., Nummenmaa, A., Van Dijk, K.R., Van Horn, J.D., Drews, M.K., Somerville, L.H., Sheridan, M.A., Santillana, R.M., Snyder, J., Hedden, T., Shaw, E.E., Hollinshead, M.O., Renvall, V., Zanzonico, R., Keil, B., Cauley, S., Polimeni, J.R., Tisdall, D., Buckner, R.L., Wedeen, V.J., Wald, L.L., Toga, A.W., Rosen, B.R., 2016. MGH-USC Human connectome project datasets with ultra-high b-value diffusion MRI. *Neuroimage* 124, 1108–1114. doi:10.1016/j.neuroimage.2015.08.075.
- Farzinfar, M., Li, Y., Verde, A.R., Oguz, I., Gerig, G., Styner, M.A., 2013. DTI quality control assessment via error estimation from Monte Carlo simulations. In: *Medical Imaging 2013: Image Processing*. SPIE, p. 86692C. doi:10.1117/12.2006925. URL <https://www.ncbi.nlm.nih.gov/pmc/articles/PMC3702180/>
- Farzinfar, M., Oguz, I., Smith, R.G., Verde, A.R., Dietrich, C., Gupta, A., Escobar, R.L., Piven, J., Pujol, S., Vachet, C., Gouttard, S., Gerig, G., Dager, S., McKinstry, R.C., Paterson, S., Evans, A.C., Styner, M.A., 2013. Diffusion imaging quality control via entropy of principal direction distribution. *Neuroimage* 82, 1–12. doi:10.1016/j.neuroimage.2013.05.022.
- Filiard, P., Pennec, X., Arsigny, V., Ayache, N., 2007. Clinical DT-MRI estimation, smoothing, and fiber tracking with log-euclidean metrics. *IEEE Trans Med Imaging* 26 (11), 1472–1482. doi:10.1109/TMI.2007.899173.
- Finsterbusch, J., 2009. Eddy-current compensated diffusion weighting with a single refocusing rf pulse. *Magn Reson Med* 61 (3), 748–754. doi:10.1002/mrm.21899. URL <https://www.ncbi.nlm.nih.gov/pubmed/19132755>
- Foo, T.K.F., Tan, E.T., Vermilyea, M.E., Hua, Y., Fiveland, E.W., Piel, J.E., Park, K., Ricci, J., Thompson, P.S., Graziani, D., Conte, G., Kagan, A., Bai, Y., Vasil, C., Tarasek, M., Yeo, D.T., Snell, F., Lee, D., Dean, A., DeMarco, J.K., Shih, R.Y., Hood, M.N., Chae, H., Ho, V.B., 2020. Highly efficient head-only magnetic field insert gradient coil for achieving simultaneous high gradient amplitude and slew rate at 3.0T (MAGNUS) for brain microstructure imaging. *Magn Reson Med* 83 (6), 2356–2369. doi:10.1002/mrm.28087.

- Forman, C., Aksoy, M., Hornegger, J., Bammer, R., 2011. Self-encoded marker for optical prospective head motion correction in mri. *Med Image Anal* 15 (5), 708–719. doi:10.1016/j.media.2011.05.018.
- Froeling, M., Tax, C.M., Vos, S.B., Luijten, P.R., Leemans, A., 2017. “MASSIVE” Brain dataset: multiple acquisitions for standardization of structural imaging validation and evaluation. *Magn Reson Med* 77 (5), 1797–1809. doi:10.1002/mrm.26259.
- Gallichan, D., Scholz, J., Bartsch, A., Behrens, T.E., Robson, M.D., Miller, K.L., 2009. Addressing a systematic vibration artifact in diffusion-weighted MRI. *Hum Brain Mapp* 31 (2), NA–NA. doi:10.1002/hbm.20856.
- Garyfallidis, E., Brett, M., Amirbekian, B., Rokem, A., Van Der Walt, S., Descoteaux, M., Nimmo-Smith, I., 2014. Dipy, a library for the analysis of diffusion mri data. *Front Neuroinform* 8, 8.
- Gavish, M., Donoho, D.L., 2017. Optimal shrinkage of singular values. *IEEE Trans. Inf. Theory* 63 (4), 2137–2152.
- Geman, S., 1987. Statistical methods for tomographic image reconstruction. *Bull. Int. Stat. Inst* 4, 5–21. URL <https://ci.nii.ac.jp/naid/10006751899>
- Gholam, J., Szczepankiewicz, F., Aja-Fernandez, S., Jones, D.K., Beltrachini, L. AD-WI-BIDS: an extension to the brain imaging data structure for advanced diffusion weighted imaging.
- Gibbs, J.W., 1898. Fourier’s series. *Nature* 59 (1522), 200–200.
- Girard, G., Whittingstall, K., Deriche, R., Descoteaux, M., 2015. Structural connectivity reproducibility through multiple acquisitions. Organization for Human Brain Mapping. URL <https://hal.inria.fr/hal-01174327>
- Glasser, M.F., Sotiropoulos, S.N., Wilson, J.A., Coalson, T.S., Fischl, B., Andersson, J.L., Xu, J., Jbabdi, S., Webster, M., Polimeni, J.R., Van Essen, D.C., Jenkinson, M., 2013. The minimal preprocessing pipelines for the human connectome project. *Neuroimage* 80, 105–124. doi:10.1016/j.neuroimage.2013.04.127. URL <https://www.sciencedirect.com/science/article/pii/S1053811913005053?via%3Dihub>.
- Glover, G. H., Pelc, N. J., 1983. Method for correcting image distortion due to gradient nonuniformity.
- Golkov, V., Dosovitskiy, A., Sperl, J.I., Menzel, M.I., Czisch, M., Sämann, P., Brox, T., Cremers, D., 2016. Q-space deep learning: twelve-fold shorter and model-free diffusion mri scans. *IEEE Trans Med Imaging* 35 (5), 1344–1351. doi:10.1109/TMI.2016.2551324.
- Gorgolewski, K., Burns, C.D., Madison, C., Clark, D., Halchenko, Y.O., Waskom, M.L., Ghosh, S.S., 2011. Nipype: A Flexible, lightweight and extensible neuroimaging data processing framework in python. *Front Neuroinform* 5, 13. doi:10.3389/fninf.2011.00013.
- Gorgolewski, K.J., Alfaro-Almagro, F., Auer, T., Bellec, P., Capotà, M., Chakravarty, M.M., Churchill, N.W., Cohen, A.L., Craddock, R.C., Devenyi, G.A., Eklund, A., Esteban, O., Flandin, G., Ghosh, S.S., Guntupalli, J.S., Jenkinson, M., Keshavan, A., Kiar, G., Liem, F., Raamana, P.R., Raffelt, D., Steele, C.J., Quirion, P.-O., Smith, R.E., Strother, S.C., Varoquaux, G., Wang, Y., Yarkoni, T., Poldrack, R.A., 2017. BIDS Apps: improving ease of use, accessibility, and reproducibility of neuroimaging data analysis methods. *PLoS Comput. Biol.* 13 (3), e1005209. doi:10.1371/JOURN.PCBL.1005209.
- Gorgolewski, K.J., Auer, T., Calhoun, V.D., Craddock, R.C., Das, S., Duff, E.P., Flandin, G., Ghosh, S.S., Glatard, T., Halchenko, Y.O., Handwerker, D.A., Hanke, M., Keator, D., Li, X., Michael, Z., Maumet, C., Nichols, B.N., Nichols, T.E., Pellmar, J., Poline, J.B., Rokem, A., Schaefer, G., Sochat, V., Triplett, W., Turner, J.A., Varoquaux, G., Poldrack, R.A., 2016. The brain imaging data structure, a format for organizing and describing outputs of neuroimaging experiments. *Sci Data* 3 (1), 1–9. doi:10.1038/sdata.2016.44. URL www.nature.com/sdata/.
- Graham, M.S., Drobnyak, I., Jenkinson, M., Zhang, H., 2017. Quantitative assessment of the susceptibility artefact and its interaction with motion in diffusion MRI. *PLoS ONE* 12 (10), e0185647. doi:10.1371/journal.pone.0185647.
- Graham, M.S., Drobnyak, I., Zhang, H., 2016. Realistic simulation of artefacts in diffusion mri for validating post-processing correction techniques. *Neuroimage* 125, 1079–1094. doi:10.1016/j.neuroimage.2015.11.006. URL <https://www.sciencedirect.com/science/article/pii/S1053811915010289>.
- Graham, M.S., Drobnyak, I., Zhang, H., 2018. A supervised learning approach for diffusion MRI quality control with minimal training data. *Neuroimage* 178, 668–676. doi:10.1016/j.neuroimage.2018.05.077.
- Grussu, F., Battiston, M., Palombo, M., Schneider, T., Gandini Wheeler-Kingshott, C., Alexander, D., 2020a. Deep learning model fitting for diffusion-relaxometry: a comparative study. *10.1101/2020.10.20.347625*
- Grussu, F., Battiston, M., Veraart, J., Schneider, T., Cohen-Adad, J., Shepherd, T.M., Alexander, D.C., Fieremans, E., Novikov, D.S., Gandini Wheeler-Kingshott, C.A., 2020. Multi-parametric quantitative in vivo spinal cord MRI with unified signal readout and image denoising. *Neuroimage* 217, 116884. doi:10.1016/j.neuroimage.2020.116884.
- Gu, X., Eklund, A., 2019. Evaluation of six phase encoding based susceptibility distortion correction methods for diffusion mri. *Front Neuroinform* 13, 76.
- Gudbjartsson, H., Patz, S., 1995. The rician distribution of noisy mri data. *Magn Reson Med* 34 (6), 910–914. doi:10.1002/mrm.1910340618. URL <https://www.ncbi.nlm.nih.gov/pmc/articles/PMC2254141/>.
- Guo, F., de Luca, A., Parker, G., Jones, D., Viergever, M., Leemans, A., Tax, C., 2020. The effect of gradient nonlinearities on fiber orientation estimates from spherical deconvolution of diffusion magnetic resonance imaging data. *Hum Brain Mapp* doi:10.1002/hbm.25228.
- Guo, F., Tax, C., de Luca, A., Viergever, M., Heemskerk, A., Leemans, A., 2019. Effects of inaccurate response function calibration on characteristics of the fiber orientation distribution in diffusion MRI. *10.1101/760546*
- Haddad, S.M.H., Scott, C.J.M., Ouzzou, M., Holmes, M.F., Arnott, S.R., Nanayakkara, N.D., Ramirez, J., Black, S.E., Dowlatshahi, D., Strother, S.C., Swartz, R.H., Symons, S., Montero-Odasso, M., Bartha, R., 2019. Comparison of quality control methods for automated diffusion tensor imaging analysis pipelines. *PLoS ONE* 14 (12), e0226715. doi:10.1371/journal.pone.0226715.
- Hagler, D.J., Hatton, S., Cornejo, M.D., Makowski, C., Fair, D.A., Dick, A.S., Sutherland, M.T., Casey, B.J., Barch, D.M., Harms, M.P., Watts, R., Bjork, J.M., Garavan, H.P., Hilmer, L., Pung, C.J., Sicut, C.S., Kuperman, J., Bartsch, H., Xue, F., Heitzeg, M.M., Laird, A.R., Trinh, T.T., Gonzalez, R., Tapert, S.F., Riedel, M.C., Squeglia, L.M., Hyde, L.W., Rosenberg, M.D., Earl, E.A., Howlett, K.D., Baker, F.C., Soules, M., Diaz, J., de Leon, O.R., Thompson, W.K., Neale, M.C., Herting, M., Sowell, E.R., Alvarez, R.P., Hawes, S.W., Sanchez, M., Bodurka, J., Breslin, F.J., Morris, A.S., Paulus, M.P., Simmons, W.K., Polimeni, J.R., van der Kouwe, A., Nencka, A.S., Gray, K.M., Pierpaoli, C., Matochik, J.A., Noronha, A., Aklin, W.M., Conway, K., Glantz, M., Hoffman, E., Little, R., Lopez, M., Pariyadath, V., Weiss, S.R.B., Wolff-Hughes, D.L., DelCarmen-Wiggins, R., Feldstein Ewing, S.W., Miranda-Dominguez, O., Nagel, B.J., Perrone, A.J., Sturgeon, D.T., Goldstone, A., Pfefferbaum, A., Pohl, K.M., Prouty, D., Uban, K., Bookheimer, S.Y., Dapretto, M., Galvan, A., Bagot, K., Giedd, J., Infante, M.A., Jacobus, J., Patrick, K., Shilling, P.D., Siskian, R., Li, Y., Sugrue, L., Banich, M.T., Friedman, N., Hewitt, J.K., Hopfer, C., Sakai, J., Tanabe, J., Cottler, L.B., Nixon, S.J., Chang, L., Cloak, C., Ernst, T., Reeves, G., Kennedy, D.N., Heeringa, S., Peltier, S., et al., 2019. Image processing and analysis methods for the adolescent brain cognitive development study. *Neuroimage* 202, 116091. doi:10.1016/j.neuroimage.2019.116091. URL <https://www.sciencedirect.com/science/article/pii/S1053811919306822>.
- Haldar, J.P., Wedeen, V.J., Nezamzadeh, M., Dai, G., Weiner, M.W., Schuff, N., Liang, Z.-P., 2013. Improved diffusion imaging through snr-enhancing joint reconstruction. *Magn Reson Med* 69 (1), 277–289.
- Hansen, C.B., Nath, V., Hainline, A.E., Schilling, K.G., Parvathaneni, P., Bayrak, R.G., Blaber, J.A., Irfanoglu, O., Pierpaoli, C., Anderson, A.W., et al., 2019. Characterization and correlation of signal drift in diffusion weighted mri. *Magn Reson Imaging* 57, 133–142.
- Hansen, C.B., Rogers, B.P., Schilling, K.G., Nath, V., Blaber, J.A., Irfanoglu, O., Barnett, A., Pierpaoli, C., Anderson, A.W., Landman, B.A., 2021. Empirical field mapping for gradient nonlinearity correction of multi-site diffusion weighted MRI. *Magn Reson Imaging* 76, 69–78. doi:10.1016/j.mri.2020.11.005.
- Harms, M.P., Somerville, L.H., Ances, B.M., Andersson, J., Barch, D.M., Bastiani, M., Bookheimer, S.Y., Brown, T.B., Buckner, R.L., Burgess, G.C., Coalson, T.S., Chappell, M.A., Dapretto, M., Douaud, G., Fischl, B., Glasser, M.F., Greve, D.N., Hodge, C., Jamison, K.W., Jbabdi, S., Kandala, S., Li, X., Mair, R.W., Mangia, S., Marcus, D., Mascali, D., Moeller, S., Nichols, T.E., Robinson, E.C., Salat, D.H., Smith, S.M., Sotiropoulos, S.N., Terpstra, M., Thomas, K.M., Tisdall, M.D., Ugrubil, K., van der Kouwe, A., Woods, R.P., Zölle, L., Van Essen, D.C., Yacoub, E., 2018. Extending the human connectome project across ages: imaging protocols for the lifespan development and aging projects. *Neuroimage* 183, 972–984. doi:10.1016/j.neuroimage.2018.09.060. URL <https://www.sciencedirect.com/science/article/pii/S1053811918318652>.
- Hasan, K.M., 2007. A framework for quality control and parameter optimization in diffusion tensor imaging: theoretical analysis and validation. *Magn Reson Imaging* 25 (8), 1196–1202. doi:10.1016/j.mri.2007.02.011.
- Haselgrove, J.C., Moore, J.R., 1996. Correction for distortion of echo-planar images used to calculate the apparent diffusion coefficient. *Magn Reson Med* 36 (6), 960–964. doi:10.1002/mrm.1910360620. URL <https://www.ncbi.nlm.nih.gov/pubmed/8946363>
- Heid, O., US Patent 6,043,6512000. Method for the phase correction of nuclear magnetic resonance signals.
- Hoge, W.S., Polimeni, J.R., 2016. Dual-polarity grappa for simultaneous reconstruction and ghost correction of echo planar imaging data. *Magn Reson Med* 76 (1), 32–44. doi:10.1002/mrm.25839.
- Hoge, W.S., Setsompop, K., Polimeni, J.R., 2018. Dual-polarity slice-grappa for concurrent ghost correction and slice separation in simultaneous multi-slice epi. *Magn Reson Med* 80 (4), 1364–1375. doi:10.1002/mrm.27113.
- Holland, D., Kuperman, J.M., Dale, A.M., 2010. Efficient correction of inhomogeneous static magnetic field-induced distortion in echo planar imaging. *Neuroimage* 50, 175–183.
- Hong, Y., Chen, G., Yap, P.T., Shen, D., 2019. Multifold acceleration of diffusion MRI via deep learning reconstruction from slice-under-sampled data. *Inf Process Med Imaging* 11492, 530–541. doi:10.1007/978-3-030-20351-1_41.
- Horsfield, M.A., 1999. Mapping eddy current induced fields for the correction of diffusion-weighted echo planar images. *Magn Reson Imaging* 17 (9), 1335–1345. doi:10.1016/s0730-725x(99)00077-6. URL <https://www.ncbi.nlm.nih.gov/pubmed/10576719>
- Howard, A.F., Mollink, J., Kleinnijhuis, M., Pallbage-Gamarallage, M., Bastiani, M., Cottarr, M., Miller, K.L., Jbabdi, S., 2019. Joint modelling of diffusion mri and microscopy. *Neuroimage* 201. doi:10.1016/j.neuroimage.2019.116014. 116014–116014. URL <https://pubmed.ncbi.nlm.nih.gov/31315062> <https://www.ncbi.nlm.nih.gov/pmc/articles/PMC6880780/>.
- Hu, X., Le, T., 1996. Artifact reduction in epi with phase-encoded reference scan. *Magn Reson Med* 36, 166–171.
- Hu, Z., Wang, Y., Zhang, Z., Zhang, J., Zhang, H., Guo, C., Sun, Y., Guo, H., 2020. Distortion correction of single-shot epi enabled by deep-learning. *Neuroimage* 221, 117170. doi:10.1016/j.neuroimage.2020.117170. URL <https://www.sciencedirect.com/science/article/pii/S105381192030656X>.
- Hutter, J., Sator, P.J., Christiaens, D., Teixeira, R.P.A.G., Roberts, T., Jackson, L., Price, A.N., Malik, S., Hajnal, J.V., 2018. Integrated and efficient diffusion-relaxometry using ZEBRA. *Sci Rep* 8 (1), 15138. doi:10.1038/s41598-018-33463-2.
- Hutter, J., Tournier, J.D., Price, A.N., Cordero-Grande, L., Hughes, E.J., Malik, S., Steinweg, J., Bastiani, M., Sotiropoulos, S.N., Jbabdi, S., Andersson, J., Edwards, A.D., Hajnal, J.V., 2018. Time-efficient and flexible design of optimized multishell hardi diffusion. *Magn Reson Med* 79 (3), 1276–1292. doi:10.1002/mrm.26765.

- Hédouin, R., Commowick, O., Bannier, E., Scherrer, B., Taquet, M., Warfield, S.K., Barillot, C., 2017. Block-matching distortion correction of echo-planar images with opposite phase encoding directions. *IEEE Trans Med Imaging* 36 (5), 1106–1115. doi:10.1109/TMI.2016.2646920.
- Irfanoglu, M.O., Modi, P., Nayak, A., Hutchinson, E.B., Sarlls, J., Pierpaoli, C., 2015. DR-BUDDI: (Diffeomorphic registration for blip-up blip-down diffusion imaging) method for correcting echo planar imaging distortions. *Neuroimage* 106, 284–289.
- Irfanoglu, M.O., Nayak, A., Jenkins, J., Hutchinson, E.B., Sadeghi, N., Thomas, C.P., Pierpaoli, C., 2016. DR-TAMAS: Diffeomorphic registration for tensor accurate alignment of anatomical structures. *Neuroimage* 132, 439–454.
- Irfanoglu, M.O., Nayak, A., Jenkins, J., Pierpaoli, C., 2017. TORTOISEv3: improvements and new features of the NIH Diffusion MRI processing pipeline. In: *Proceedings of International Society of Magnetic Resonance in Medicine*, p. 3540.
- Irfanoglu, M.O., Sadeghi, N., Sarlls, J., Pierpaoli, C., 2020. Improved reproducibility of diffusion MRI of the human brain with a four-way blip-up and down phase-encoding acquisition approach. *Magn Reson Med*.
- Irfanoglu, M.O., Sarlls, J., Nayak, A., Pierpaoli, C., 2019. Evaluating corrections for eddy-currents and other epi distortions in diffusion mri: methodology and a dataset for benchmarking. *Magn Reson Med* 81 (4), 2774–2787. doi:10.1002/mrm.27577.
- Irfanoglu, M.O., Walker, L., Sarlls, J., Marengo, S., Pierpaoli, C., 2012. Effects of image distortions originating from susceptibility variations and concomitant fields on diffusion MRI tractography results. *Neuroimage* 15 (61), 275–288.
- Janke, A., Zhao, H., Cowin, G.J., Galloway, G.J., Doddrell, D.M., 2004. Use of spherical harmonic deconvolution methods to compensate for nonlinear gradient effects on MRI images. *Magn Reson Med* 52 (1), 115–122. doi:10.1002/mrm.20122.
- Jbabdi, S., Sotiropoulos, S.N., Savio, A.M., Graña, M., Behrens, T.E.J., 2012. Model-based analysis of multishell diffusion mr data for tractography: how to get over fitting problems. *Magn Reson Med* 68 (6), 1846–1855. doi:10.1002/mrm.24204. URL <https://pubmed.ncbi.nlm.nih.gov/22334356> <https://www.ncbi.nlm.nih.gov/pmc/articles/PMC3359399/>.
- Jenkinson, M., Bannister, P., Brady, M., Smith, S., 2002. Improved optimization for the robust and accurate linear registration and motion correction of brain images. *Neuroimage* 17 (2), 825–841. doi:10.1016/S1053-8119(02)9132-8.
- Jenkinson, M., Beckmann, C.F., Behrens, T.E., Woolrich, M.W., Smith, S.M., 2012. FSL. *Neuroimage* 62 (2), 782–790. doi:10.1016/J.NEUROIMAGE.2011.09.015. URL <https://www.sciencedirect.com/science/article/pii/S1053811911010603?via3DiHub>.
- Jenkinson, M., Smith, S., 2001. A global optimisation method for robust affine registration of brain images. *Med Image Anal* 5 (2), 143–156. doi:10.1016/S1361-8415(01)00036-6.
- Jeurissen, B., Leemans, A., Sijbers, J., 2014. Automated correction of improperly rotated diffusion gradient orientations in diffusion weighted mri. *Med Image Anal* 18 (7), 953–962.
- Jezzard, P., Balaban, R.S., 1995. Correction for geometric distortion in echo planar images from B0 field variations. *Magn Reson Med* 34, 65–73.
- Jezzard, P., Barnett, A.S., Pierpaoli, C., 1998. Characterization of and correction for eddy current artifacts in echo planar diffusion imaging. *Magn Reson Med* 39 (5), 801–812. doi:10.1002/mrm.1910390518. URL <https://www.ncbi.nlm.nih.gov/pubmed/9581612>
- Jiang, H., Van Zijl, P.C., Kim, J., Pearlson, G.D., Mori, S., 2006. DtiStudio: resource program for diffusion tensor computation and fiber bundle tracking. *Comput Methods Programs Biomed* 81 (2), 106–116. doi:10.1016/j.cmpb.2005.08.004.
- Jiang, S., Xue, H., Glover, A., Rutherford, M., Rueckert, D., Hajnal, J.V., 2007. Mri of moving subjects using multislice snapshot images with volume reconstruction (svr): application to fetal, neonatal, and adult brain studies. *IEEE Trans Med Imaging* 26 (7), 967–980. doi:10.1109/tmi.2007.895456.
- Jolly, E., Sadhukha, S., Chang, L.J., 2020. Custom-molded headcases have limited efficacy in reducing head motion during naturalistic fmri experiments. *Neuroimage* 222, 117207. doi:10.1016/J.NEUROIMAGE.2020.117207.
- Jones, D., Alexander, D., Bowtell, R., Cercignani, M., Dell'Acqua, F., McHugh, D., Miller, K., Palombo, M., Parker, G., Rudrapatna, U., Tax, C., 2018. Microstructural imaging of the human brain with a 'super-scanner': 10 key advantages of ultra-strong gradients for diffusion MRI. *Neuroimage* doi:10.1016/J.NEUROIMAGE.2018.05.047. URL <https://www.sciencedirect.com/science/article/pii/S1053811918304610?via3DiHub>.
- Jones, D.K., 2004. The effect of gradient sampling schemes on measures derived from diffusion tensor MRI: A Monte carlo study. *Magn Reson Med* 51 (4), 807–815. doi:10.1002/mrm.20033.
- Jones, D.K., Cercignani, M., 2010. Twenty-five pitfalls in the analysis of diffusion MRI data. *NMR Biomed* 23 (7), 803–820. doi:10.1002/nbm.1543.
- Kellner, E., Dhital, B., Kiselev, V.G., Reisert, M., 2016. Gibbs-ringing artifact removal based on local subvoxel-shifts. *Magn Reson Med* 76 (5), 1574–1581. doi:10.1002/mrm.26054.
- Kennedy, M., Lee, Y., Nagy, Z., 2018. An industrial design solution for integrating nmr magnetic field sensors into an mri scanner. *Magn Reson Med* 80 (2), 833–839. doi:10.1002/mrm.27055.
- Kim, B., Boes, J.L., Bland, P.H., Chenevert, T.L., Meyer, C.R., 1999. Motion correction in fmri via registration of individual slices into an anatomical volume. *Magn Reson Med* 41 (5), 964–972. doi:10.1002/(sici)1522-2594(199905)41:5<964::aid-mrm16>3.0.co;2-d.
- Kim, K., Habas, P.A., Rousseau, F., Glenn, O.A., Barkovich, A.J., Studholme, C., 2010. Intersection based motion correction of multislice mri for 3-d in utero fetal brain image formation. *IEEE Trans Med Imaging* 29 (1), 146–158. doi:10.1109/tmi.2009.2030679.
- Kim, K.H., Park, S.-H., 2017. Artificial neural network for suppression of banding artifacts in balanced steady-state free precession mri. *Magn Reson Imaging* 37, 139–146. doi:10.1016/j.mri.2016.11.020.
- Kleban, E., Tax, C.M., Rudrapatna, U.S., Jones, D.K., Bowtell, R., 2020. Strong diffusion gradients allow the separation of intra- and extra-axonal gradient-echo signals in the human brain. *Neuroimage* 217, 116793. doi:10.1016/j.neuroimage.2020.116793.
- Kleesiek, J., Urban, G., Hubert, A., Schwarz, D., Maier-Hein, K., Bendszus, M., Biller, A., 2016. Deep mri brain extraction: a 3d convolutional neural network for skull stripping. *Neuroimage* 129, 460–469. doi:10.1016/j.neuroimage.2016.01.024. URL <https://www.sciencedirect.com/science/article/pii/S1053811916000306>.
- Knoll, F., Bredies, K., Pock, T., Stollberger, R., 2011. Second order total generalized variation (tgv) for mri. *Magn Reson Med* 65 (2), 480–491.
- Koay, C.G., Chang, L.-C., Carew, J.D., Pierpaoli, C., Basser, P.J., 2006. A unifying theoretical and algorithmic framework for least squares methods of estimation in diffusion tensor imaging. *J. Magn. Reson.* 182 (1), 115–125. doi:10.1016/j.jmr.2006.06.020.
- Koay, C.G., Özarslan, E., Pierpaoli, C., 2009. Probabilistic identification and estimation of noise (PIESNO): a self-consistent approach and its applications in MRI. *J. Magn. Reson.* 199 (1), 94–103. doi:10.1016/J.JMR.2009.03.005. URL <https://www.sciencedirect.com/science/article/pii/S1090780709000767?via3DiHub>.
- Koch, A., Zhukov, A., Stöcker, T., Groeschel, S., Schultz, T., 2019. SHORE-Based detection and imputation of dropout in diffusion MRI. *Magn Reson Med* 82 (6), 2286–2298. doi:10.1002/mrm.27893.
- Kochunov, P., Dickie, E.W., Viviano, J.D., Turner, J., Kingsley, P.B., Jahanshad, N., Thompson, P.M., Ryan, M.C., Fieremans, E., Novikov, D., Veraart, J., Hong, E.L., Malhotra, A.K., Buchanan, R.W., Chavez, S., Voineskos, A.N., 2018. Integration of routine qa data into mega-analysis may improve quality and sensitivity of multisite diffusion tensor imaging studies. *Hum Brain Mapp* 39 (2), 1015–1023. doi:10.1002/hbm.23900.
- Koster, J., Rahmann, S., 2012. Snakemake—a scalable bioinformatics workflow engine. *Bioinformatics* 28 (19), 2520–2522. doi:10.1093/bioinformatics/bts480.
- Krissian, K., Aja-Fernández, S., 2009. Noise-driven anisotropic diffusion filtering of mri. *IEEE Trans. Image Process.* 18 (10), 2265–2274.
- Kurtzer, G.M., Sochat, V., Bauer, M.W., 2017. Singularity: scientific containers for mobility of compute. *PLoS ONE* 12 (5). doi:10.1371/journal.pone.0177459.
- Kybic, J., Thevenaz, P., Nirkko, A., Unser, M., 2000. Unwarping of unidirectionally distorted EPI images. *IEEE Trans Med Imaging* 19 (2), 80–93.
- Küstner, T., Liebgott, A., Mauch, L., Martirosian, P., Bamberg, F., Nikolaou, K., Yang, B., Schick, F., Gatidis, S., 2018. Automated reference-free detection of motion artifacts in magnetic resonance images. *Magn Reson Mater Phys.* 31, 243–256. doi:10.1007/s10334-017-0650-z.
- Lam, F., Babacan, S.D., Haldar, J.P., Weiner, M.W., Schuff, N., Liang, Z.-P., 2014. Denoising diffusion-weighted magnitude mr images using rank and edge constraints. *Magn Reson Med* 71 (3), 1272–1284.
- Lampinen, B., Szczepankiewicz, F., Mårtensson, J., Westin, D., Hansson, O., Westin, C., Nilsson, M., 2020. Towards unconstrained compartment modeling in white matter using diffusion-relaxation MRI with tensor-valued diffusion encoding. *Magn Reson Med* 84 (3), 1605–1623. doi:10.1002/mrm.28216.
- Lampinen, B., Szczepankiewicz, F., Novén, M., van Westen, D., Hansson, O., Englund, E., Mårtensson, J., Westin, C.F., Nilsson, M., 2019. Searching for the neurite density with diffusion mri: challenges for biophysical modeling. *Hum Brain Mapp* 40 (8), 2529–2545. doi:10.1002/hbm.24542.
- Langlois, S., Desvignes, M., Constans, J., Revenu, M., 1999. MRI Geometric distortion: a simple approach to correcting the effects of non-linear gradient fields. *J. Magn. Reson. Imaging* 9 (6), 821–831. doi:10.1002/(SICI)1522-2586(199906)9:6<821::AID-JMRI9>3.0.CO;2-2.
- Larkman, D.J., Nunes, R.G., 2007. Parallel magnetic resonance imaging. *Phys Med Biol* 52 (7), R15–55. doi:10.1088/0031-9155/52/7/R01. URL <https://www.ncbi.nlm.nih.gov/pubmed/17374908>
- Lauzon, C.B., Asman, A.J., Esparza, M.L., Burns, S.S., Fan, Q., Gao, Y., Anderson, A.W., Davis, N., Cutting, L.E., Landman, B.A., 2013. Simultaneous analysis and quality assurance for diffusion tensor imaging. *PLoS ONE* 8 (4), e61737. doi:10.1371/journal.pone.0061737.
- Le Bihan, D., Poupon, C., Amadon, A., Lethimonnier, F., 2006. Artifacts and pitfalls in diffusion MRI. *J. Magn. Reson. Imaging* 24 (3), 478–488. doi:10.1002/jmri.20683.
- Le Bihan, D., Poupon, C., Amadon, A., Lethimonnier, F., 2006. Artifacts and pitfalls in diffusion mri. *J. Magn Reson Imaging* 24 (3), 478–488. doi:10.1002/jmri.20683. URL <https://www.ncbi.nlm.nih.gov/pubmed/16897692>
- Lebel, C., Gee, M., Camicioli, R., Wieler, M., Martin, W., Beaulieu, C., 2012. Diffusion tensor imaging of white matter tract evolution over the lifespan. *Neuroimage* 60 (1), 340–352. doi:10.1016/j.neuroimage.2011.11.094. URL <https://www.sciencedirect.com/science/article/pii/S1053811911013760>.
- Lee, J., Jin, K.H., Ye, J.C., 2016. Reference-free single-pass EPI nyquist ghost correction using annihilating filter-based low rank hankel matrix (ALPHA). *Magn Reson Med* 76 (6), 1775–1789. doi:10.1002/mrm.26077.
- Lee, Y., Kettinger, A.O., Wilm, B.J., Deichmann, R., Weiskopf, N., Lambert, C., Pruessmann, K.P., Nagy, Z., 2020. A comprehensive approach for correcting voxel-wise b-value errors in diffusion MRI. *Magn Reson Med* 83 (6), 2173–2184. doi:10.1002/mrm.28078. URL <https://www.ncbi.nlm.nih.gov/pmc/articles/PMC7065087/>.
- Leemans, A., Jeurissen, B., Sijbers, J., Jones, D., 2009. ExploreDTI: a graphical toolbox for processing, analyzing, and visualizing diffusion MR data. *Proceedings 17th Scientific Meeting, International Society for Magnetic Resonance in Medicine* 17 (2), 3537.
- Leemans, A., Jones, D.K., 2009. The <i>b</i>-matrix must be rotated when correcting for subject motion in DTI data. *Magn Reson Med* 61 (6), 1336–1349. doi:10.1002/mrm.21890.
- Lehtinen, J., Munkberg, J., Hasselgren, J., Laine, S., Karras, T., Aittala, M., Aila, T., 2018. Noise2noise: Learning image restoration without clean data. In: *International Conference on Machine Learning*. PMLR, pp. 2965–2974.
- Jerma-Usabiaga, G., Mukherjee, P., Perry, M.L., Wandell, B.A., 2020. Data-science ready,

- Basser, P.J., 2013. Mean apparent propagator (MAP) MRI: a novel diffusion imaging method for mapping tissue microstructure. *Neuroimage* 78, 16–32.
- Pajevic, S., Pierpaoli, C., 1999. Color schemes to represent the orientation of anisotropic tissues from diffusion tensor data: application to white matter fiber tract mapping in the human brain. *Magn Reson Med* 42 (3), 526–540. doi:10.1002/(SICI)1522-2594(199909)42:3<526::AID-MRM15>3.0.CO;2-J.
- Pan, Z., Guo, H., Dai, E., Auerbach, E., Ugurbil, K., Wu, X., 2020. Coil-joint-split N/2 ghost correction and joint L1-SPIRiT for SMS-EPI reconstruction: Demonstration using 7T HCP-style diffusion acquisition. In: *Proceedings of International Society of Magnetic Resonance in Medicine*, p. 0983.
- Pannek, K., Raffelt, D., Bell, C., Mathias, J.L., Rose, S.E., 2012. HOMOR: Higher order model outlier rejection for high b-value MR diffusion data. *Neuroimage* 63 (2), 835–842. doi:10.1016/j.neuroimage.2012.07.022. URL <https://pubmed.ncbi.nlm.nih.gov/22819964/>.
- Papadakis, N.G., Martin, K.M., Pickard, J.D., Hall, L.D., Carpenter, T.A., Huang, C.L., 2000. Gradient preemphasis calibration in diffusion-weighted echo-planar imaging. *Magn Reson Med* 44 (4), 616–624. doi:10.1002/1522-2594(200010)44:4<616::aid-mrm16>3.0.co;2-t. URL <https://www.ncbi.nlm.nih.gov/pubmed/11025518>
- Papadakis, N.G., Sponias, T., Berwick, J., Mayhew, J.E., 2005. K-space correction of eddy-current-induced distortions in diffusion-weighted echo-planar imaging. *Magn Reson Med* 53 (5), 1103–1111. doi:10.1002/mrm.20429. URL <https://www.ncbi.nlm.nih.gov/pubmed/15844088>.
- Paquette, M., Gilbert, G., Descoteaux, M., 2019. Penthera 3T10.5281/ZENODO.2602049
- Paquette, M., Tax, C.M., Eichner, C., Anwander, A., 2020. Impact of gradient nonlinearities on B-tensor diffusion encoding. *Proc. Intl. Soc. Mag. Reson. Med.* 28, 4412–undefined. URL <http://indexsmart.miramir.com/ISMRM2020/PDFfiles/4412.html>
- Parker, G.D., Marshall, D., Rosin, P.L., Drage, N., Richmond, S., Jones, D.K., 2013. RES-DORE: Robust estimation in spherical deconvolution by outlier rejection. *ISMRM* 21, 3148–undefined. URL <https://archive.ismrm.org/2013/3148.html>.
- Passingham, R.E., Stephan, K.E., Köster, R., 2002. The anatomical basis of functional localization in the cortex. *Nat. Rev. Neurosci.* 3 (8), 606–616. doi:10.1038/nrn893.
- Patel, V., Dinov, I.D., Van Horn, J.D., Thompson, P.M., Toga, A.W., 2010. LONI Mind: metadata in Nifti for DWI. *Neuroimage* 51 (2), 665–676. doi:10.1016/j.neuroimage.2010.02.069.
- Pawar, K., Chen, Z., Shah, N., Egan, G., 2018. Moconet: motion correction in 3d mprage images using a convolutional neural network approach. *ArXiv:1807.10831*.
- Perrone, D., Aelterman, J., Pižurica, A., Jeurissen, B., Philips, W., Leemans, A., 2015. The effect of gibbs ringing artifacts on measures derived from diffusion MRI. *Neuroimage* 120, 441–455. doi:10.1016/j.neuroimage.2015.06.068.
- Perrone, D., Jeurissen, B., Aelterman, J., Roine, T., Sijbers, J., Pižurica, A., Leemans, A., Philips, W., 2016. D-BRAIN: Anatomically accurate simulated diffusion MRI brain data. *PLoS ONE* 11 (3), e0149778. doi:10.1371/journal.pone.0149778.
- Peterson, E., Aksoy, M., Maclaren, M.J., Bammer, R., 2015. Acquisition-free Nyquist ghost correction for parallel imaging accelerated EPI. In: *Proceedings of International Society of Magnetic Resonance in Medicine*, p. 75.
- Pierpaoli, C., 2010. Artifacts in Diffusion MRI. In: *Diffusion MRI*. Oxford University Press, pp. 303–318. doi:10.1093/med/9780195369779.003.0018. URL <http://oxfordmedicine.com/view/10.1093/med/9780195369779.001.0001/med-9780195369779-chapter-018>
- Pierpaoli, C., Basser, P.J., 1996. Toward a quantitative assessment of diffusion anisotropy. *Magn Reson Med* 36 (6), 893–906. doi:10.1002/mrm.1910360612. URL <https://pubmed.ncbi.nlm.nih.gov/8946355/>.
- Pierpaoli, C., Walker, L., Irfanoglu, M.O., Barnett, A.S., Chang, L.C., Koay, C.G., Pajevic, S., Rohde, G.K., Sarlis, J., Wu, M., 2010. TORTOISE: An integrated software package for processing of diffusion MRI data. In: *Proceedings of International Society of Magnetic Resonance in Medicine*, p. 1597.
- Pizzolato, M., Fick, R.R., Boutelier, T.T., Deriche, R., 2016. Noise Floor Removal via Phase Correction of Complex Diffusion-Weighted Images: Influence on DTI and q-space Metrics. In: *Computational Diffusion MRI (MICCAI)*, pp. 127–140. URL <https://hal.inria.fr/hal-01358770>
- Pizzolato, M., Gilbert, G., Thiran, J.P., Descoteaux, M., Deriche, R., 2020. Adaptive phase correction of diffusion-weighted images. *Neuroimage* 206, 116274. doi:10.1016/j.neuroimage.2019.116274.
- Porter, D.A., Calamante, F., Gadian, D.G., Connelly, A., 1999. The effect of residual nyquist ghost in quantitative echo-planar diffusion imaging. *Magn Reson Med* 42 (2), 385–392. doi:10.1002/(SICI)1522-2594(199908)42:2<385::AID-MRM21>3.0.CO;2-J.
- Powell, E., Schneider, T., Battiston, M., Grussu, F., Toosy, A., Clayden, J.D., Gandini Wheeler-Kingshott, C.A.M., 2020. Sense reconstruction with simultaneous 2D phase correction and channel-wise noise removal (SPECTRE). In: *Proceedings of International Society of Magnetic Resonance in Medicine*, p. 4361.
- Prohl, A.K., Scherrer, B., Tomas-Fernandez, X., Filip-Dhima, R., Kapur, K., Velasco-Annis, C., Clancy, S., Carmody, E., Dean, M., Valle, M., Prabh, S.P., Peters, J.M., Bebin, E.M., Krueger, D.A., Northrup, H., Wu, J.Y., Sahin, M., Warfield, S.K., 2019. Reproducibility of structural and diffusion tensor imaging in the tacern multi-center study. *Front Integr Neurosci* 13. doi:10.3389/fnint.2019.00024. 24–24, URL <https://pubmed.ncbi.nlm.nih.gov/31417372> <https://www.ncbi.nlm.nih.gov/pmc/articles/PMC6650594/>.
- Qiao, Y., Shi, Y., 2020. Unsupervised deep learning for susceptibility distortion correction in connectome imaging. In: *Martel, A.L., Abolmaesumi, P., Stoyanov, D., Mateus, D., Zuluaga, M.A., Zhou, S.K., Racoceanu, D., Joskowicz, L. (Eds.), Medical Image Computing and Computer Assisted Intervention – MICCAI 2020*. Springer International Publishing, Cham, pp. 302–310.
- Qiao, Y., Sun, W., Shi, Y., 2019. Fod-based registration for susceptibility distortion correction in brainstem connectome imaging. *Neuroimage* 202, 116164. doi:10.1016/j.neuroimage.2019.116164.
- Raffelt, D., Tournier, J.-D., Frupp, J., Crozier, S., Connelly, A., Salvado, O., 2011. Symmetric diffeomorphic registration of fibre orientation distributions. *Neuroimage* 56 (3), 1171–1180.
- Raffelt, D.A., Tournier, J.-D., Smith, R.E., Vaughan, D.N., Jackson, G., Ridgway, G.R., Connelly, A., 2017. Investigating white matter fibre density and morphology using fixel-based analysis. *Neuroimage* 144, 58–73. doi:10.1016/j.neuroimage.2016.09.029. URL <http://www.sciencedirect.com/science/article/pii/S1053811916304943>.
- Ramos-Llordén, G., Ning, L., Liao, C., Mukhometzianov, R., Michailovich, O., Setsompop, K., Rath, Y., 2020. High-fidelity, accelerated whole-brain submillimeter in vivo diffusion mri using gslider-spherical ridgelets (gslider-sr). *Magn Reson Med* 84 (4), 1781–1795. doi:10.1002/mrm.28232.
- Reese, T.G., Heid, O., Weisskoff, R.M., Wedeen, V.J., 2003. Reduction of eddy-current-induced distortion in diffusion mri using a twice-refocused spin echo. *Magn Reson Med* 49 (1), 177–182. doi:10.1002/mrm.10308. URL <https://www.ncbi.nlm.nih.gov/pubmed/12509835>
- Reid, R.I., Nedelska, Z., Schwarz, C.G., Ward, C., Jack, C.R., Initiative, A.D.N., et al., 2018. Diffusion Specific Segmentation: Skull Stripping with Initiation MRI Data Alone. In: *Computational Diffusion MRI*. Springer, pp. 67–80.
- Roalf, D.R., Quarmley, M., Elliott, M.A., Satterthwaite, T.D., Vandekar, S.N., Ruparel, K., Gennatas, E.D., Calkins, M.E., Moore, T.M., Hopson, R., Prabhakaran, K., Jackson, C.T., Verma, R., Hakonarson, H., Gur, R.C., Gur, R.E., 2016. The impact of quality assurance assessment on diffusion tensor imaging outcomes in a large-scale population-based cohort. *Neuroimage* 125, 903–919. doi:10.1016/j.neuroimage.2015.10.068.
- Roebroeck, A., Miller, K.L., Aggarwal, M., 2019. Ex vivo diffusion mri of the human brain: technical challenges and recent advances. *NMR Biomed* 32 (4), e3941. doi:10.1002/nbm.3941.
- Rohde, G., Barnett, A., Basser, P., Marengo, S., Pierpaoli, C., 2004. Comprehensive approach for correction of motion and distortion in diffusion-weighted MRI. *Magn Reson Med* 51 (1), 103–114. doi:10.1002/mrm.10677.
- Rohde, G.K., Barnett, A.S., Basser, P.J., Pierpaoli, C., 2005. Estimating intensity variance due to noise in registered images: applications to diffusion tensor mri. *Neuroimage* 26 (3), 673–684. doi:10.1016/j.neuroimage.2005.02.023.
- Rudin, L.I., Osher, S., Fatemi, E., 1992. Nonlinear total variation based noise removal algorithms. *Physica D* 60 (1–4), 259–268.
- Rudrapatna, U., Parker, G.D., Roberts, J., Jones, D.K., 2021. A comparative study of gradient nonlinearity correction strategies for processing diffusion data obtained with ultra-strong gradient MRI scanners. *Magn Reson Med* 85 (2), 1104–1113. doi:10.1002/mrm.28464.
- Ruthotto, L., Kugel, H., Olesch, J., Fischer, B., Modersitzki, J., Burger, M., Wolters, C.H., 2012. Diffeomorphic susceptibility artifact correction of diffusion-weighted magnetic resonance images. *Phys Med Biol* 57 (18), 5715.
- Ruthotto, L., Mohammadi, S., Heck, C., Modersitzki, J., Weiskopf, N., 2013. Hyperelastic susceptibility artifact correction of DTI in SPM. In: *Meinzer, H.-P., Deserno, T.M., Handels, H., Tolxdorff, T. (Eds.), Bildverarbeitung für die Medizin 2013*. Springer Berlin Heidelberg, Berlin, Heidelberg, pp. 344–349.
- Sairanen, V., Leemans, A., Tax, C.M., 2018. Fast and accurate slice-wise outlier detection (SOLID) with informed model estimation for diffusion MRI data. *Neuroimage* 181, 331–346. doi:10.1016/j.neuroimage.2018.07.003.
- Samani, Z.R., Alappatt, J.A., Parker, D., Ismail, A.A.O., Verma, R., 2020. QC-Automator: Deep learning-based automated quality control for diffusion MR images. *Front Neurosci* 13, 1456. doi:10.3389/fnins.2019.01456. URL <https://www.frontiersin.org/article/10.3389/fnins.2019.01456/full>.
- Schilling, K.G., Blaber, J., Huo, Y., Newton, A., Hansen, C., Nath, V., Shafer, A.T., Williams, O., Resnick, S.M., Rogers, B., Anderson, A.W., Landman, B.A., 2019. Synthesized b0 for diffusion distortion correction (synb0-disco). *Magn Reson Imaging* 64, 62–70. doi:10.1016/j.mri.2019.05.008. Artificial Intelligence in MRI.
- Schilling, K.G., Fadnavis, S., Visagie, M., Garyfallidis, E., Landman, B.A., Smith, S.A., O’Grady, K.P., 2021. Patch2self denoising of diffusion mri in the cervical spinal cord improves repeatability and feature conspicuity. *International Society for Magnetic Resonance in Medicine Annual Meeting*.
- Schilling, K.G., Yeh, F.-C., Nath, V., Hansen, C., Williams, O., Resnick, S., Anderson, A.W., Landman, B.A., 2019. A fiber coherence index for quality control of b-table orientation in diffusion mri scans. *Magn Reson Imaging* 58, 82–89.
- Schlemper, J., Caballero, J., Hajnal, J.V., Price, A.N., Rueckert, D., 2018. A deep cascade of convolutional neural networks for dynamic mr image reconstruction. *IEEE Trans Med Imaging* 37 (2), 491–503. doi:10.1109/TMI.2017.2760978.
- Seo, S., Do, W.-J., Luu, H.M., Kim, K.H., Choi, S.H., Park, S.-H., 2020. Artificial neural network for slice encoding for metal artifact correction (semac) mri. *Magn Reson Med* 84 (1), 263–276. doi:10.1002/mrm.28126.
- Serag, A., Blesa, M., Moore, E.J., Pataky, R., Sparrow, S.A., Wilkinson, A., Macnaught, G., Semple, S.I., Boardman, J.P., 2016. Accurate learning with few atlases (alfa): an algorithm for neonatal brain extraction and comparison with 11 publicly available methods. *Sci Rep* 6 (1), 1–15.
- Setsompop, K., Kimmlingen, R., Eberlein, E., Witzel, T., Cohen-Adad, J., McNab, J.A., Keil, B., Tisdall, M.D., Hoecht, P., Dietz, P., Cauley, S.F., Tountcheva, V., Matschl, V., Lenz, V.H., Heberlein, K., Potthast, A., Thein, H., Van Horn, J., Toga, A., Schmitt, F., Lehne, D., Rosen, B.R., Wedeen, V., Wald, L.L., 2013. Pushing the limits of in vivo diffusion MRI for the human connectome project. *Neuroimage* 80, 220–233. doi:10.1016/j.neuroimage.2013.05.078.
- Shan, S., Yan, W., Guo, X., Chang, E.I.-C., Fan, Y., Xu, Y., 2019. Unsupervised end-to-end learning for medical image registration.
- Sijbers, J., den Dekker, A.J., Scheunders, P., Van Dyck, D., 1998. Maximum-likelihood estimation of rician distribution parameters. *IEEE Trans Med Imaging* 17 (3), 357–361.
- Sinke, M.R.T., Otte, W.M., Christiaens, D., Schmitt, O., Leemans, A., van der Toorn, A., Sarabjit Singh, R.A., Joëls, M., Dijkhuizen, R.M., 2018. Diffusion mri-based corti-

- cal connectome reconstruction: dependency on tractography procedures and neuroanatomical characteristics. *Brain Structure and Function* 223 (5), 2269–2285. doi:10.1007/s00429-018-1628-y.
- Skare, S., Andersson, J.L., 2001. On the effects of gating in diffusion imaging of the brain using single shot EPI. *Magn Reson Imaging* 19 (8), 1125–1128. doi:10.1016/S0730-725X(01)00415-5. URL <https://pubmed.ncbi.nlm.nih.gov/11711237/>.
- Skare, S., Clayton, D.B., Newbould, R., Moseley, M., Bammer, R., 2006. A fast and robust minimum entropy based non-interactive Nyquist ghost correction algorithm. In: *Proceedings of International Society of Magnetic Resonance in Medicine*, p. 2349.
- Skope, 2019. Skope field camera. URL <https://www.skope.swiss/diffusion-imaging>.
- Sled, J.G., Pike, G.B., 2000. Quantitative interpretation of magnetization transfer in spoiled gradient echo MRI sequences. *J. Magn. Reson.* 145 (1), 24–36. doi:10.1006/jmre.2000.2059.
- Smith, A.M., Lewis, B.K., Ruttimann, U.E., Ye, F.Q., Sinnwell, T.M., Yang, Y., Duyn, J.H., Frank, J.A., 1999. Investigation of low frequency drift in fmrisignal. *Neuroimage* 9 (5), 526–533. doi:10.1006/nimg.1999.0435.
- Smith, S.M., 2002. Fast robust automated brain extraction. *Hum Brain Mapp* 17 (3), 143–155.
- Smith, S.M., Brady, J.M., 1997. SUSAN-A New approach to low level image processing. *International Journal of Computer Vision* 1997 23:1 23 (1), 45–78. doi:10.1023/A:1007963824710.
- Smith, S.M., Jenkinson, M., Johansen-Berg, H., Rueckert, D., Nichols, T.E., Mackay, C.E., Watkins, K.E., Ciccarelli, O., Cader, M.Z., Matthews, P.M., Behrens, T.E., 2006. Tract-based spatial statistics: voxelwise analysis of multi-subject diffusion data. *Neuroimage* 31 (4), 1487–1505. doi:10.1016/j.neuroimage.2006.02.024.
- Sotiropoulos, S.N., Jbabdi, S., Andersson, J.L., Woolrich, M.W., Ugurbil, K., Behrens, T.E., 2013. Rubix: combining spatial resolutions for bayesian inference of crossing fibers in diffusion mri. *IEEE Trans Med Imaging* 32 (6), 969–982. doi:10.1109/TMI.2012.2231873. URL <https://www.ncbi.nlm.nih.gov/pubmed/23362247>
- Sotiropoulos, S.N., Jbabdi, S., Andersson, J.L., Woolrich, M.W., Ugurbil, K., Behrens, T.E., 2013. Rubix: combining spatial resolutions for bayesian inference of crossing fibers in diffusion MRI. *IEEE Trans Med Imaging* 32 (6), 969–982. doi:10.1109/TMI.2012.2231873. URL <http://ieeexplore.ieee.org/document/6420959/>.
- Sotiropoulos, S.N., Jbabdi, S., Xu, J., Andersson, J.L., Moeller, S., Auerbach, E.J., Glasser, M.F., Hernandez, M., Sapiro, G., Jenkinson, M., Feinberg, D.A., Yacoub, E., Lenglet, C., Van Essen, D.C., Ugurbil, K., Behrens, T.E., 2013. Advances in diffusion mri acquisition and processing in the human connectome project. *Neuroimage* 80, 125–143. doi:10.1016/j.neuroimage.2013.05.057.
- Sperl, J.I., Sprenger, T., Tan, E.T., Menzel, M.I., Hardy, C.J., Marinelli, L., 2017. Model-based denoising in diffusion-weighted imaging using generalized spherical deconvolution. *Magn Reson Med* 78 (6), 2428–2438.
- St-Jean, S., Coupé, P., Descoteaux, M., 2016. Non local spatial and angular matching: enabling higher spatial resolution diffusion mri datasets through adaptive denoising. *Med Image Anal* 32, 115–130.
- St-Jean, S., De Luca, A., Tax, C.M., Viergever, M.A., Leemans, A., 2020. Automated characterization of noise distributions in diffusion mri data. *Med Image Anal* 65, 101758.
- Stejskal, E.O., Tanner, J.E., 1965. Spin diffusion measurements: spin echoes in the presence of a time-Dependent field gradient. *J Chem Phys* 42 (1), 288–292. doi:10.1063/1.1695690.
- Storey, P., Frigo, F.J., Hinks, R.S., Mock, B.J., Collick, B.D., Baker, N., Marmurek, J., Graham, S.J., 2007. Partial-space reconstruction in single-shot diffusion-weighted echo-planar imaging. *Magn Reson Med* 57 (3), 614–619. doi:10.1002/mrm.21132.
- Szczepankiewicz, F., Lasić, S., van Westen, D., Sundgren, P.C., Englund, E., Westin, C.-F., Ståhlberg, F., Lätt, J., Topgaard, D., Nilsson, M., 2015. Quantification of microscopic diffusion anisotropy disentanglements effects of orientation dispersion from microstructure: applications in healthy volunteers and in brain tumors. *Neuroimage* 104, 241–252. doi:10.1016/j.neuroimage.2014.09.057. URL <https://www.sciencedirect.com/science/article/pii/S105381191400799X>.
- Szczepankiewicz, F., Sjöland, J., Dall'Armellina, E., Plein, S., Schneider, J.E., Teh, I., Westin, C., 2021. Motion-compensated gradient waveforms for tensor-valued diffusion encoding by constrained numerical optimization. *Magn Reson Med* 85 (4), 2117–2126. doi:10.1002/mrm.28551.
- Szczepankiewicz, F., Westin, C., Nilsson, M., 2019. Maxwell-compensated design of asymmetric gradient waveforms for tensor-valued diffusion encoding. *Magn Reson Med* 82 (4), 1424–1437. doi:10.1002/mrm.27828.
- Tao, R., Fletcher, P.T., Gerber, S., Whitaker, R.T., 2009. A variational image-based approach to the correction of susceptibility artifacts in the alignment of diffusion weighted and structural MRI. *Information Processing in Medical Imaging* 21, 651–663.
- Tao, S., Trzasko, J.D., Shu, Y., Huston, J., Bernstein, M.A., 2015. Integrated image reconstruction and gradient nonlinearity correction. *Magn Reson Med* 74 (4), 1019–1031. doi:10.1002/mrm.25487.
- Tax, C., Grusso, F., Kaden, E., Ning, L., Rudrapatna, U., John Evans, C., St-Jean, S., Leemans, A., Koppers, S., Merhof, D., Ghosh, A., Tanno, R., Alexander, D., Zappalà, S., Charron, C., Kusmia, S., Linden, D., Jones, D., Veraart, J., 2019. Cross-scanner and cross-protocol diffusion MRI data harmonisation: a benchmark database and evaluation of algorithms. *Neuroimage* 195. doi:10.1016/j.neuroimage.2019.01.077.
- Chantal, M.W.T., Kleban, E., Chamberland, M., Baraković, M., Rudrapatna, U., Jones, D.K., 2021. Measuring compartmental T2-orientational dependence in human brain white matter using a tiltable RF coil and diffusion-T2 correlation MRI. *NeuroImage* 236, 117967.
- Tax, C., Vos, S., Leemans, A., 2016. Checking and correcting DTI data doi:10.1007/978-1-4939-3118-7.7.
- Tax, C.M., Otte, W.M., Viergever, M.A., Dijkhuizen, R.M., Leemans, A., 2015. REKINDLE: Robust extraction of kurtosis INDICES with linear estimation. *Magn Reson Med* 73 (2), 794–808. doi:10.1002/mrm.25165.
- Tax, C.M., Szczepankiewicz, F., Nilsson, M., Jones, D.K., 2019. The dot-compartment revealed? diffusion MRI with ultra-strong gradients and spherical tensor encoding in the living human brain. *bioRxiv* doi:10.1101/584730.
- Taylor, P., Rajendra, J., Nayak, A., Irfanoglu, O.M., Glen1, D.R., Reynolds, R.C., 2018. New analysis and visualization tools afni-fatcat (and implementing other software). *International Society for Magnetic Resonance in Medicine Annual Meeting*.
- Taylor, P.A., Alhamud, A., van der Kouwe, A., Saleh, M.G., Loughton, B., Meintjes, E., 2016. Assessing the performance of different DTI motion correction strategies in the presence of EPI distortion correction. *Hum Brain Mapp* 37 (12), 4405–4424. doi:10.1002/hbm.23318.
- Teh, I., Maguire, M.L., Schneider, J.E., 2017. Efficient gradient calibration based diffusion mri. *Magn Reson Med* 77 (1), 170–179. doi:10.1002/mrm.26105.
- Theaud, G., Houde, J.C., Boré, A., Rheault, F., Morency, F., Descoteaux, M., 2020. Tractoflow: a robust, efficient and reproducible diffusion MRI pipeline leveraging nextflow & singularity. *Neuroimage* 218, 116889. doi:10.1016/j.neuroimage.2020.116889.
- Thompson, P., Stein, J., Medland, S., Hibar, D., Vasquez, A., Renteria, M., Toro, R., Jahanshad, N., Schumann, G., Franke, B., Wright, M., Martin, N., Agartz, I., Alda, M., Alhusaini, S., Almasy, L., Almeida, J., Alpert, K., Andreassen, N., Andreassen, O., Apostolova, L., Appel, K., Armstrong, N., Aribisala, B., Bastin, M., Bauer, M., Bearden, C., Bergmann, Ø., Binder, E., Blangero, J., Bockholt, H., Bøen, E., Bois, C., Boomsma, D., Booth, T., Bowman, I., Bralten, J., Brouwer, R., Brunner, H., Brohawn, D., Buckner, R., Buitelaar, J., Bulayeva, K., Bustillo, J., Calhoun, V., Cannon, D., Cantor, R., Carless, M., Caseras, X., Cavalleri, G., Chakravarty, M., Chang, K., Ching, C., Christoforou, A., Cichon, S., Clark, V., Conrod, P., Coppola, G., Crespo-Facorro, B., Curran, J., Czisch, M., Dearn, I., de Geus, E., den Braber, A., Delvecchio, G., Depondt, C., de Haan, L., de Zubicaray, G., Dima, D., Dimitrova, R., Djurovic, S., Dong, H., Donohoe, G., Dugger, R., Dyer, T., Ehrlich, S., Ekman, C., Elvsåshagen, T., Emsell, L., Erk, S., Espeseth, T., Fagnerness, J., Fears, S., Fedko, I., Fernández, G., Fisher, S., Foroud, T., Fox, P., Francks, C., Frangou, S., Frey, E., Frodl, T., Frouin, V., Garavan, H., Giddaluru, S., Glahn, D., Godlewska, B., Goldstein, R., Gollub, R., Grabe, H., Grimm, O., Gruber, O., Guadalupe, T., Gur, R., Gur, R., Göring, H., Hagenaars, S., Hajek, T., Hall, G., Hall, J., Hardy, J., Hartman, C., Hass, J., Hatton, S., Haukvik, U., Hegenscheid, K., Heinz, A., Hickie, I., Ho, B., Hoehn, D., Hoekstra, P., Hollinshead, M., Holmes, A., Homuth, G., Hoogman, M., Hong, L., Hosten, N., Hottenga, J., Hulshoff Pol, H., Hwang, K., Jack, C., Jenkinson, M., Johnston, C., Jönsson, E., Kahn, R., Kasperaviciute, D., Kelly, S., Kim, S., Kochunov, P., Koenders, L., Krämer, B., Kwok, J., Lagopoulos, J., Laje, G., Landen, M., Landman, B., Lauriello, J., Lawrie, S., Lee, P., Le Hellard, S., Lemaitre, H., Leonardo, C., Li, C., Liberg, B., Liewald, D., Liu, X., Lopez, L., Loth, E., Lourdasamy, A., Luciano, M., Macciardi, F., Machielsen, M., MacQueen, G., Malt, U., Mandl, R., Manoach, D., Martinot, J., Matarin, M., Mather, K., Mattheisen, M., Mattingsdal, M., Meyer-Lindenberg, A., McDonald, C., McIntosh, A., McMahon, F., McMahon, K., Meisenzahl, E., Melle, I., Milaneschi, Y., Mohnke, S., Montgomery, G., Morris, D., Moses, E., Mueller, E., Muñoz Maniega, S., Müllerleisen, T., Müller-Myhsok, B., Mwangi, B., Nauck, M., Nho, K., Nichols, T., Nilsson, L., Nugent, A., Nyberg, L., Olvera, R., Oosterlaan, J., Ophoff, R., Pandolfo, M., Papalampropoulou-Tsiridou, M., Pappmeyer, M., Paus, T., Pausova, Z., Pearlson, G., Penninx, B., Peterson, C., Pfennig, A., Phillips, M., Pike, G., Poline, J., Potkin, S., Pütz, B., Ramasamy, A., Rasmussen, J., Rietschel, M., Rijpkema, M., Risacher, S., Roffman, J., Roiz-Santiañez, R., Romanczuk-Seiferth, N., Rose, E., Royle, N., Rujescu, D., Ryten, M., Sachdev, P., Salami, A., Satterthwaite, T., Savitz, J., Saykin, A., Scanlon, C., Schmaal, L., Schnack, H., Schork, A., Schulz, S., Schür, R., Seidman, L., Shen, L., Shoemaker, J., Simmons, A., Sisodiya, S., Smith, C., Smoller, J., Soares, J., Sponheim, S., Sprooten, E., Starr, J., Steen, V., Strakowski, S., Strike, L., Sussmann, J., Sämman, P., Teumer, A., Toga, A., Tordesillas-Gutierrez, D., Trabzuni, D., Trost, S., Turner, J., Van den Heuvel, M., van der Wee, N., van Eijk, K., van Erp, T., van Haren, N., van 't Ent, D., van Tol, M., Valdés Hernández, M., Veltman, D., Verace, A., Völzke, H., Walker, R., Walter, H., Wang, L., Wardlaw, J., Weale, M., Weiner, M., Wen, W., Westlye, L., Whalley, H., Whelan, C., White, T., Winkler, A., Wittfeld, K., Woldehawariat, G., Wolf, C., Zilles, D., Zwiers, M., Thalathumuth, A., Schofield, P., Freimer, N., Lawrence, N., Drevets, W., 2014. The enigma consortium: large-scale collaborative analyses of neuroimaging and genetic data. *Brain Imaging Behav* 8 (2), 153–182. doi:10.1007/s11682-013-9269-5.
- Tian, Q., Bilgic, B., Fan, Q., Liao, C., Ngamsombat, C., Hu, Y., Witzel, T., Setsompop, K., Polimeni, J.R., Huang, S.Y., 2020. Deepdti: high-fidelity six-direction diffusion tensor imaging using deep learning. *Neuroimage* 219, 117017. doi:10.1016/j.neuroimage.2020.117017.
- Tian, Q., Li, Z., Fan, Q., Ngamsombat, C., Hu, Y., Liao, C., Wang, F., Setsompop, K., Polimeni, J.R., Bilgic, B., Huang, S.Y., 2021. Srdti: deep learning-based super-resolution for diffusion tensor mri.
- Tournier, J.-D., Mori, S., Leemans, A., 2011. Diffusion tensor imaging and beyond. *Magn Reson Med* 65 (6), 1532–1556. doi:10.1002/mrm.22924.
- Tournier, J.D., Smith, R., Raffelt, R., Tabbara, R., Dhollander, T., Pietsch, M., Christiaens, D., Jeurissen, B., Yeh, C.H., Connelly, A., 2019. MRtrix3: A fast, flexible and open software framework for medical image processing and visualisation. *Neuroimage* 202. doi:10.1016/J.NEUROIMAGE.2019.116137. URL <https://pubmed.ncbi.nlm.nih.gov/31473352/>.
- Truong, T.-K., Guidon, A., 2014. High-resolution multitshot spiral diffusion tensor imaging with inherent correction of motion-induced phase errors. *Magn Reson Med* 71 (2), 790–796. doi:10.1002/mrm.24709. URL <https://pubmed.ncbi.nlm.nih.gov/23450457> <https://www.ncbi.nlm.nih.gov/pmc/articles/PMC3949176/>.
- Tustison, N.J., Avants, B.B., Cook, P.A., Zheng, Y., Egan, A., Yushkevich, P.A., Gee, J.C.,

2010. N4itk: Improved n3 bias correction. *IEEE Trans Med Imaging* 29 (6), 1310–1320.
- Vellmer, S., Tonoyan, A.S., Suter, D., Pronin, I.N., Maximov, I.I., 2018. Validation of DWI pre-processing procedures for reliable differentiation between human brain gliomas. *Z Med Phys* 28 (1), 14–24. doi:10.1016/j.zemedi.2017.04.005. URL <https://pubmed.ncbi.nlm.nih.gov/28532604/>.
- Veraart, J., Fieremans, E., Jolescu, I.O., Knoll, F., Novikov, D.S., 2016. Gibbs ringing in diffusion mri. *Magn Reson Med* 76 (1), 301–314.
- Veraart, J., Fieremans, E., Novikov, D.S., 2016. Diffusion mri noise mapping using random matrix theory. *Magn Reson Med* 76 (5), 1582–1593.
- Veraart, J., Novikov, D.S., Fieremans, E., 2018. TE Dependent diffusion imaging (TEddi) distinguishes between compartmental T2 relaxation times. *Neuroimage* 182, 360–369. doi:10.1016/j.neuroimage.2017.09.030. URL <https://www.sciencedirect.com/science/article/pii/S1053811917307784?via3Dihub>.
- Veraart, J., Sijbers, J., Sunaert, S., Leemans, A., Jeurissen, B., 2013. Weighted linear least squares estimation of diffusion MRI parameters: strengths, limitations, and pitfalls. *Neuroimage* 81, 335–346. doi:10.1016/j.neuroimage.2013.05.028. URL <https://www.sciencedirect.com/science/article/pii/S1053811913005223?via3Dihub>.
- Veraart, J., Van Hecke, W., Sijbers, J., 2011. Constrained maximum likelihood estimation of the diffusion kurtosis tensor using a rician noise model. *Magn Reson Med* 66 (3), 678–686.
- Vos, S.B., Jones, D.K., Viergever, M.A., Leemans, A., 2011. Partial volume effect as a hidden covariate in dti analyses. *Neuroimage* 55 (4), 1566–1576.
- Vos, S.B., Tax, C.M., Luijten, P.R., Ourselin, S., Leemans, A., Froeling, M., 2017. The importance of correcting for signal drift in diffusion mri. *Magn Reson Med* 77 (1), 285–299.
- Walker, L., Chang, L.C., Koay, C.G., Sharma, N., Cohen, L., Verma, R., Pierpaoli, C., 2011. Effects of physiological noise in population analysis of diffusion tensor MRI data. *Neuroimage* 54 (2), 1168–1177. doi:10.1016/j.neuroimage.2010.08.048.
- Wandell, B., Rokem, A., Perry, L., Schaefer, G., Dougherty, R., 2018. Data management to support reproducible research.
- Wang, D., Strugnell, W., Cowin, G., Doddrell, D.M., Slaughter, R., 2004. Geometric distortion in clinical MRI systems: part i: evaluation using a 3D phantom. *Magn Reson Imaging* 22 (9), 1211–1221. doi:10.1016/j.mri.2004.08.012.
- Wang, F., Dong, Z., Tian, Q., Liao, C., Fan, Q., Hoge, W.S., Keil, B., Polimeni, J.R., Wald, L.L., Huang, S.Y., Setsompop, K., 2020. In vivo human whole-brain connectome diffusion mri dataset at 760 μm isotropic resolution. *bioRxiv* doi:10.1101/2020.10.05.327395.
- Wang, S., Su, Z., Ying, L., Peng, X., Zhu, S., Liang, F., Feng, D., Liang, D., 2016. Accelerating magnetic resonance imaging via deep learning. In: 2016 IEEE 13th International Symposium on Biomedical Imaging (ISBI), pp. 514–517. doi:10.1109/ISBI.2016.7493320.
- Wang, X., Li, X.-H., Cho, J.W., Russ, B., Rajamani, N., Omelchenko, A., Ai, L., Korchmaros, A., Garcia-Saldivar, P., Wang, Z., et al., 2020. U-Net model for brain extraction on non-human primates. *bioRxiv*.
- Wedeen, V.J., Hagmann, P., Tseng, W.-Y.I., Reese, T.G., Weisskoff, R.M., 2005. Mapping complex tissue architecture with diffusion spectrum magnetic resonance imaging. *Magn Reson Med* 54 (6), 1377–1386.
- Wedeen, V.J., Weisskoff, R.M., Poncelet, B.P., 1994. MRI Signal void due to in-plane motion is all-or-none. *Magn Reson Med* 32 (1), 116–120. doi:10.1002/mrm.1910320116.
- Weiger, M., Overweg, J., Rösler, M.B., Froidevaux, R., Hennel, F., Wilm, B.J., Penn, A., Sturzenegger, U., Schuth, W., Mathlener, M., Borgo, M., Börner, P., Leussler, C., Luechinger, R., Dietrich, B.E., Reber, J., Brunner, D.O., Schmid, T., Vionnet, L., Pruessmann, K.P., 2018. A high-performance gradient insert for rapid and short-T2 imaging at full duty cycle. *Magn Reson Med* 79 (6), 3256–3266. doi:10.1002/mrm.26954.
- Westin, C.-F., Knutsson, H., Pasternak, O., Szczepankiewicz, F., Özarslan, E., van Westen, D., Mattisson, C., Bogren, M., O'Donnell, L.J., Kubicki, M., Topgaard, D., Nilsson, M., 2016. Q-Space trajectory imaging for multidimensional diffusion mri of the human brain. *Neuroimage* 135, 345–362. doi:10.1016/j.neuroimage.2016.02.039. URL <https://www.sciencedirect.com/science/article/pii/S1053811916001488>.
- Wiest-Daesslé, N., Prima, S., Coupé, P., Morrissey, S.P., Barillot, C., 2008. Rician noise removal by non-local means filtering for low signal-to-noise ratio mri: applications to dt-mri. In: *International Conference on Medical Image Computing and Computer-assisted Intervention*. Springer, pp. 171–179.
- Wilbraham, H., 1848. On a certain periodic function. *The Cambridge and Dublin Mathematical Journal* 3, 198–201.
- Wilm, B.J., Nagy, Z., Barmet, C., Vannesjo, S.J., Kasper, L., Haeberlin, M., Gross, S., Dietrich, B.E., Brunner, D.O., Schmid, T., Pruessmann, K.P., 2015. Diffusion mri with concurrent magnetic field monitoring. *Magn Reson Med* 74 (4), 925–933. doi:10.1002/mrm.25827.
- Wirestam, R., Bibic, A., Lätt, J., Brockstedt, S., Ståhlberg, F., 2006. Denoising of complex mri data by wavelet-domain filtering: application to high-b-value diffusion-weighted imaging. *Magnetic Resonance in Medicine: An Official Journal of the International Society for Magnetic Resonance in Medicine* 56 (5), 1114–1120.
- Wu, G., Kim, M., Wang, Q., Munsell, B.C., Shen, D., 2016. Scalable high-performance image registration framework by unsupervised deep feature representations learning. *IEEE Trans. Biomed. Eng.* 63 (7), 1505–1516. doi:10.1109/TBME.2015.2496253.
- Wu, M., Chang, L.C., Walker, L., Lemaitre, H., Barnett, A.S., Marengo, S., Pierpaoli, C., 2008. Comparison of EPI distortion correction methods in diffusion tensor MRI using a novel framework. *Proceedings of MICCAI* 11, 321–329.
- Xiang, Q.-S., Ye, F.Q., 2007. Correction for geometric distortion and n/2 ghosting in epi by phase labeling for additional coordinate encoding (place). *Magn Reson Med* 57 (4), 731–741. doi:10.1002/mrm.21187.
- Yamada, H., Abe, O., Shizukuishi, T., Kikuta, J., Shinozaki, T., Dezawa, K., Nagano, A., Matsuda, M., Haradome, H., Imamura, Y., 2014. Efficacy of distortion correction on diffusion imaging: comparison of FSL eddy and eddy-correct using 30 and 60 directions diffusion encoding. *PLoS ONE* 9 (11). doi:10.1371/journal.pone.0112411. URL <https://pubmed.ncbi.nlm.nih.gov/25405472/>.
- Yang, G., McNab, J.A., 2019. Eddy current nulled constrained optimization of isotropic diffusion encoding gradient waveforms. *Magn Reson Med* 81 (3), 1818–1832. doi:10.1002/mrm.27539.
- Yang, Y., Sun, J., Li, H., Xu, Z., 2016. Deep admm-net for compressive sensing mri. In: *Proceedings of the 30th International Conference on Neural Information Processing Systems*, pp. 10–18.
- Ye, C., 2017. Tissue microstructure estimation using a deep network inspired by a dictionary-based framework. *Med Image Anal* 42, 288–299. doi:10.1016/j.media.2017.09.001.
- Ye, C., Li, X., Chen, J., 2019. A deep network for tissue microstructure estimation using modified lstm units. *Med Image Anal* 55, 49–64. doi:10.1016/j.media.2019.04.006.
- Yeh, F.-c., 2021. DSI Studio10.5281/ZENODO.4978980
- Yeh, F.-C., Wedeen, V.J., Tseng, W.-Y.I., 2010. Generalized q -sampling imaging. *IEEE Trans Med Imaging* 29 (9), 1626–1635.
- Yendiki, A., Koldeyn, K., Kakunoori, S., Kanwisher, N., Fischl, B., 2014. Spurious group differences due to head motion in a diffusion MRI study. *Neuroimage* 88, 79–90. doi:10.1016/j.neuroimage.2013.11.027.
- Yeo, D.T., Fessler, J.A., Kim, B., 2008. Concurrent correction of geometric distortion and motion using the map-slice-to-volume method in echo-planar imaging. *Magn Reson Imaging* 26 (5), 703–714. doi:10.1016/j.mri.2007.11.001.
- Yeung, J.T., Taylor, H.M., Young, I.M., Nicholas, P.J., Doyen, S., Sughrue, M.E., 2021. Unexpected hubness: a proof-of-concept study of the human connectome using pagerank centrality and implications for intracerebral neurosurgery. *J. Neurooncol.* 151 (2), 249–256.
- Zaitsev, M., Dold, C., Sakas, G., Hennig, J., Speck, O., 2006. Magnetic resonance imaging of freely moving objects: prospective real-time motion correction using an external optical motion tracking system. *Neuroimage* 31 (3), 1038–1050. doi:10.1016/j.neuroimage.2006.01.039. URL <https://www.sciencedirect.com/science/article/abs/pii/S1053811906000917>.
- Zeng, K., Zheng, H., Cai, C., Yang, Y., Zhang, K., Chen, Z., 2018. Simultaneous single- and multi-contrast super-resolution for brain mri images based on a convolutional neural network. *Comput. Biol. Med.* 99, 133–141. doi:10.1016/j.compbiomed.2018.06.010.
- Zhang, H., Yushkevich, P.A., Alexander, D.C., Gee, J.C., 2006. Deformable registration of diffusion tensor MR images with explicit orientation optimization. *Med Image Anal* 10 (5), 764–785.
- Zhang, Q., Ruan, G., Yang, W., Liu, Y., Zhao, K., Feng, Q., Chen, W., Wu, E.X., Feng, Y., 2019. Mri gibbs-ringing artifact reduction by means of machine learning using convolutional neural networks. *Magn Reson Med* 82 (6), 2133–2145.
- Zhang, Y., Brady, M., Smith, S., 2001. Segmentation of brain mr images through a hidden markov random field model and the expectation-maximization algorithm. *IEEE Trans Med Imaging* 20 (1), 45–57.
- Zhou, Z., Liu, W., Cui, J., Wang, X., Arias, D., Wen, Y., Bansal, R., Hao, X., Wang, Z., Peterson, B.S., Xu, D., 2011. Automated artifact detection and removal for improved tensor estimation in motion-corrupted DTI data sets using the combination of local binary patterns and 2D partial least squares. *Magn Reson Imaging* 29 (2), 230–242. doi:10.1016/j.mri.2010.06.022.
- Zhu, B., Liu, J., Cauley, S., 2018. Image reconstruction by domain-transform manifold learning. *Nature* 555, 487–492. doi:10.1038/nature25988.
- Zhuang, J., Hrabec, J., Kangarlou, A., Xu, D., Bansal, R., Branch, C.A., Peterson, B.S., 2006. Correction of eddy-current distortions in diffusion tensor images using the known directions and strengths of diffusion gradients. *J Magn Reson Imaging* 24 (5), 1188–1193. doi:10.1002/jmri.20727. URL <https://www.ncbi.nlm.nih.gov/pubmed/17024663>
- Zhuang, J., Lu, Z.-L., Vidal, C.B., Damasio, H., 2013. Correction of eddy current distortions in high angular resolution diffusion imaging. *J. Magn. Reson. Imaging* 37 (6). doi:10.1002/jmri.24275. sponce-spone.
- Zwiers, M.P., 2010. Patching cardiac and head motion artefacts in diffusion-weighted images. *Neuroimage* 53 (2), 565–575. doi:10.1016/j.neuroimage.2010.06.014.